Many Body Quantum Optics

Local time-averaged optical potentials using acousto-optic deflectors

Bachelor thesis by

Bodo Kaiser

Ludwig-Maximilians-Universität München

bodo.kaiser@physik.uni-muenchen.de

September 7, 2018

Supervisors: Prof. Dr. Immanuel Bloch, Dr. Monika Aidelsburger and Christian Schweizer.

Vielteilchen Quantenoptik

Lokale zeitgemittelte optische Potentiale unter Nutzung von akusto-optischen Deflektoren

Bachelorarbeit von

Bodo Kaiser

Ludwig-Maximilians-Universität München

bodo.kaiser@physik.uni-muenchen.de

7. September 2018

Betreuer: Prof. Dr. Immanuel Bloch, Dr. Monika Aidelsburger und Christian Schweizer.

Abstract

Ultracold atoms in optical lattices open up a wide range of possibilities to simulate many-body quantum phenomena, which would elsewise be neither computationally nor experimentally tangible.

The topology of the optical lattice is a decisive property of these kind of experiments and therefore of major interest. Recently, efforts have been reported to create novel optical potentials through the use of digital micromirror arrays that permit alterations of localized potentials. Though promising results have been achieved — in particular for static potentials — limitations due to the mechanical nature of these mirror arrays arise, for instance, with regard to dynamical control.

In the present work we present an alternative implementation of localized optical lattice potentials based on acousto-optic deflectors and direct digital synthesizers.

We will give a brief theoretical introduction into the main concepts, i.e. the interaction of neutral atoms with optical potentials as well as the general operation of direct digital synthesizer and acousto-optic deflectors. From the physics we can derive the requirements imposed on the technical implementation of the radio frequency (RF) signal source and the deflection.

We will find that even though the platform of digital signal synthesis generally suites our application in terms of modulation capabilities and resolution, the particular implementation of the AD9910 demonstrates several shortcomings.

In the second part we characterize the deflection efficiency of the acousto-optic deflectors. Towards the end we try to minimize the variance of the deflection efficiency by performing a random search on the amplitude segments of the RF signal. It turns out that the deflection efficiency is a highly non-linear function of the applied RF power and frequency. Furthermore minimization of the deflection efficiency variances proves to be very unstable. Though we can largely preclude electronic defects to be the source of this behaviour, further investigation is required.

Acknowledgement

The success and final outcome of the present work required a lot of guidance and assistance from many people. Without them it would not have been possible for me to deliver this work and remember the exciting time I had in the past weeks.

At most I want to thank my parents for their support, that I have been privileged to benefit from all the years. Though my life involved many unexpected turnarounds, I never felt left alone and could rely on your diverse experience whenever the situation required it.

Further I want to thank Prof. Immanuel Bloch and Dr. Monika Aidelsburger for creating and sustaining a fertile scientific environment. It has been a refreshing novelty for me to have the opportunity to have inspiring discussions at almost any time and to seamlessly implement new ideas without being limited by the present material. Moreover I want to thank Dr. Monika Aidelsburger for spending late hours to read through my work, providing me many suggestions and thereby greatly improving the overall quality of this thesis.

Equally I want to express my gratitude to all personal involved in the formation process of my thesis. Especially I want to name Christian Schweizer with whom it had been a great pleasure to work with. Further I want to thank Till Klostermann for instantly sharing his deep insights in many problems I have encountered and his help with the optical setup. Hendrik von Raven I want to thank for his overall guidance with regard to the electronic equipment. In addition I owe special thanks to Michael Schreiber who helped me understand the theoretical foundations of atoms in optical lattices, Moritz Berngruber as a great office colleague and for his help with arbitray physics questions, David Wei for his hospitality and productive discussions about the acousto-optic deflectors, and of course biggest thanks to Bodo Hecker for his advice as electrical engineer and distinct perspective on undergone challenges.

Contents

1. Introduction **7**

2. Optical potentials **12**
2.1. Atom-light interaction . . . 12
2.1.1. Dipole potential . . . 12
2.1.2. AC-Stark effect . . . 13
2.2. Laser light fields . . . 14
2.2.1. Gaussian beams . . . 15
2.3. Effective local potentials . . . 16

3. Characteristic energy scales **19**
3.1. Harmonic approximation . . . 19
3.2. Lattice structures . . . 20
3.3. Bloch states . . . 21
3.4. Energy band structure . . . 21
3.5. Wannier states . . . 24
3.6. Hopping energy . . . 24
3.6.1. Nearest-neighbor approximation . . . 25
3.7. Conclusion . . . 26

4. Experimental setup **28**
4.1. Optics . . . 28
4.1.1. Acousto-optic deflectors . . . 28
4.1.2. Setup . . . 29
4.2. Electronics . . . 31
4.2.1. Signal source . . . 31
4.2.2. Power amplifier . . . 32
4.2.3. PID controller . . . 32
4.2.4. Trigger source . . . 32
4.3. Communication . . . 33
4.4. Trial run . . . 34

5. Characterisation of the optical setup **36**
5.1. Intensity control . . . 36
5.2. Beam profile . . . 39

6. Digital signal synthesis **42**
6.1. Operating principle . . . 42
6.1.1. Clock generation . . . 44
6.1.2. Parameter modulation . . . 44
6.2. Quantization effects . . . 45
6.3. Frequency response . . . 46
6.4. Memory playback . . . 48

6.5. Digital ramp . . . 49
6.6. Frequency and time resolution . . . 50

7. Characterisation of the electronic setup **51**
7.1. Digital signal synthesizer . . . 51
7.2. Power amplifier . . . 55
7.3. Acoustic transducer . . . 57
7.3.1. Reflection spectrum . . . 57

8. Characterisation of the acousto-optic deflectors **61**
8.1. Difference between individual acousto-optic deflectors . . . 61
8.1.1. Individual acousto-optic deflectors . . . 61
8.2. 2D intensity distribution . . . 65
8.3. Diffraction efficiency optimization . . . 69

9. Summary and outlook **74**

Glossary **76**

Acronyms **77**

List of Figures **79**

List of Tables **83**

List of Listings **84**

Bibliography **85**

A. Electronics **88**
A.1. Trigger hub . . . 88

B. Calibration **90**
B.1. Fiber coupling . . . 90
B.2. Beam alignment . . . 91
B.3. Camera focus . . . 91

Chapter 1.

Introduction

In this first chapter we want to familiarize the reader with the scientific background of our work and its motivation. We hope to clarify what basic questions the discipline of ultracold atom experiments tries to solve. In a second part we want to elaborate on the concepts of localized optical potential dynamics and summarize related work reported by the community.

Many-body quantum systems studied inter alia in condensed matter physics are experimentally challenging to access and investigate directly. As a way forward, experiments with ultracold atoms in optical lattices give us a highly controllable environment where you can access observables at a single atom level, prepare clean, well-known quantum states and increase length and time scales to experimentally accessible quantities. Thus the platform of ultracold atoms in optical lattices permits us to simulate and explore quantum effects and expand our current understanding of quantum mechanics and statistical physics [1, 2]. The apparatus used for ultracold-atom experiments com-

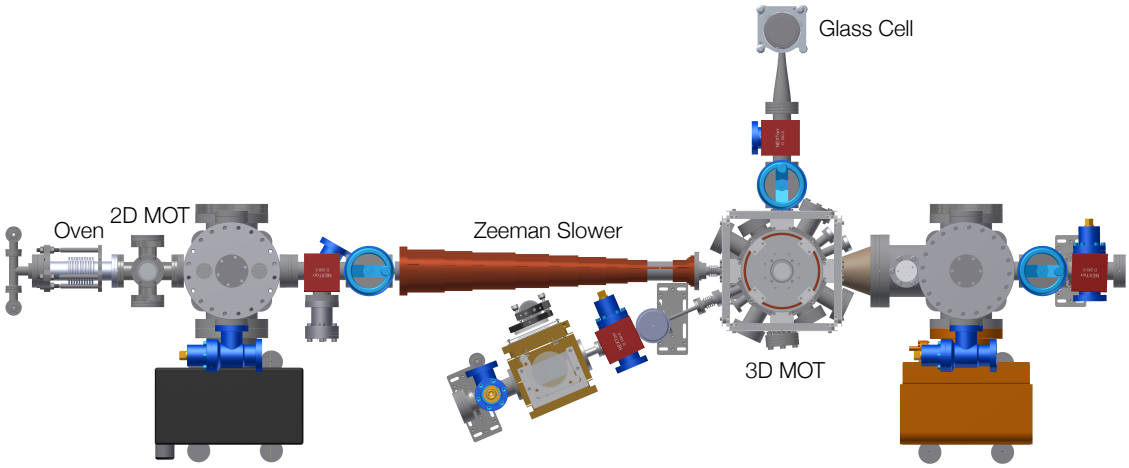

Figure 1.1.: Apparatus of the cesium experiment. On the left-hand side an oven heats up the cesium source. A two-dimensional (2D) magneto-optical trap (MOT) generates a particle beam twoards the pipe running through the Zeeman slower in the center. The Zeeman slower creates a magnetic field gradient, such that the atoms are in resonance with a cooling laser antiparallel to their flight direction. In the three-dimensional (3D) MOT atoms are cooled even further until they are transported to a glass cell where they are loaded into the optical lattice and the actual experiments are conducted. Thank you to Till Klostermann and Hendrik v. Raven for providing the cesium apparatus render.

prises a vacuum system with multiple chambers and windows for optical control and manipulation.

Figure 1.1 depicts an exemplary apparatus used for such an experiment with cesium atoms. The oven on the left-hand side heats up a cesium source to produce a hos gas of cesium atoms, which will then diffuse to the right. Two orthogonal pairwise windows enable for transverse cooling of the atoms in a 2D MOT. The Zeeman slower in the center of the apparatus creates a magnetic field gradient such that the atoms are always in resonance with a cooling laser antiparallel to the momentum direction. Through this cooling step many of the atoms can be slowed down in order to be captured in the 3D MOT where the atoms are cooled further [3]. Finally the atom cloud is transported to a glass cell at the top, where they are loaded into an optical lattice. The glass cell is placed between two high numerical aperture objectives for in-situ, single site imaging and addressing.

One major ingredient to control and manipulate the ultracold atom ensemble in the experimental chamber is the optical lattice itself. In Figure 1.2 a square 2D optical lattice is illustrated. The

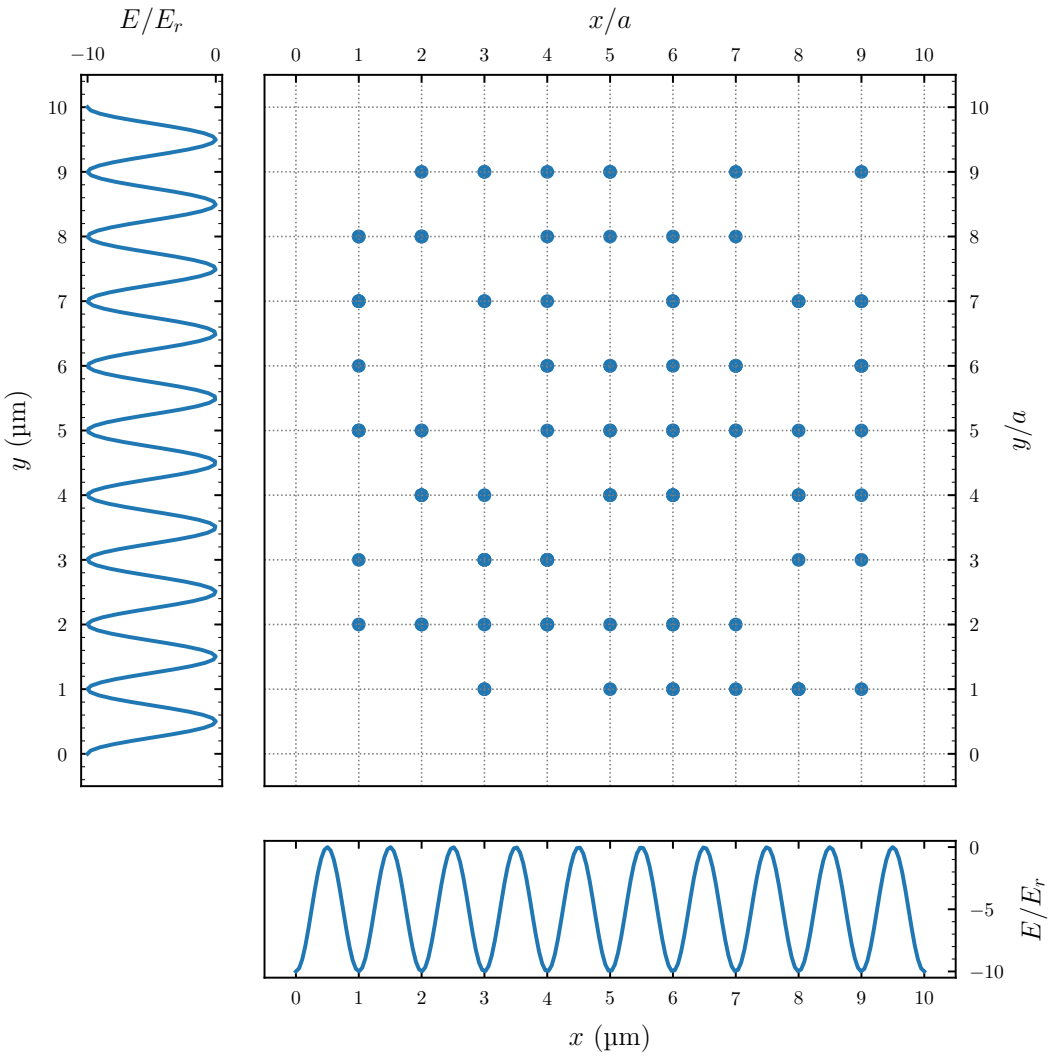

Figure 1.2.: Simple square 2D optical lattice. The atoms (blue points) sit on their respective lattice site created by the superposition of two periodic potentials.

atoms (blue points) sit on their respective lattice sites (nodes in the gray grid) which are created

by the superposition of two orthogonal optical lattice potentials (outer diagrams) [4]. In such periodic structures the atomic wave functions already show amazing similarity to the electron wave functions known from solid states physics but with much higher energies and longer time scales because of the greater mass [5, 6]. Though the square 2D optical lattice already offers many possiblities, one can think of many more variations in terms of lattice structures like hexagonal lattices or even lattices with a substructure in the literature known as superlattices. Beside changes to the global lattice structure we can also think of local changes. In Figure 1.3 we show an embodiment of a local optical lattice used to confine particles. By changing the barrier height

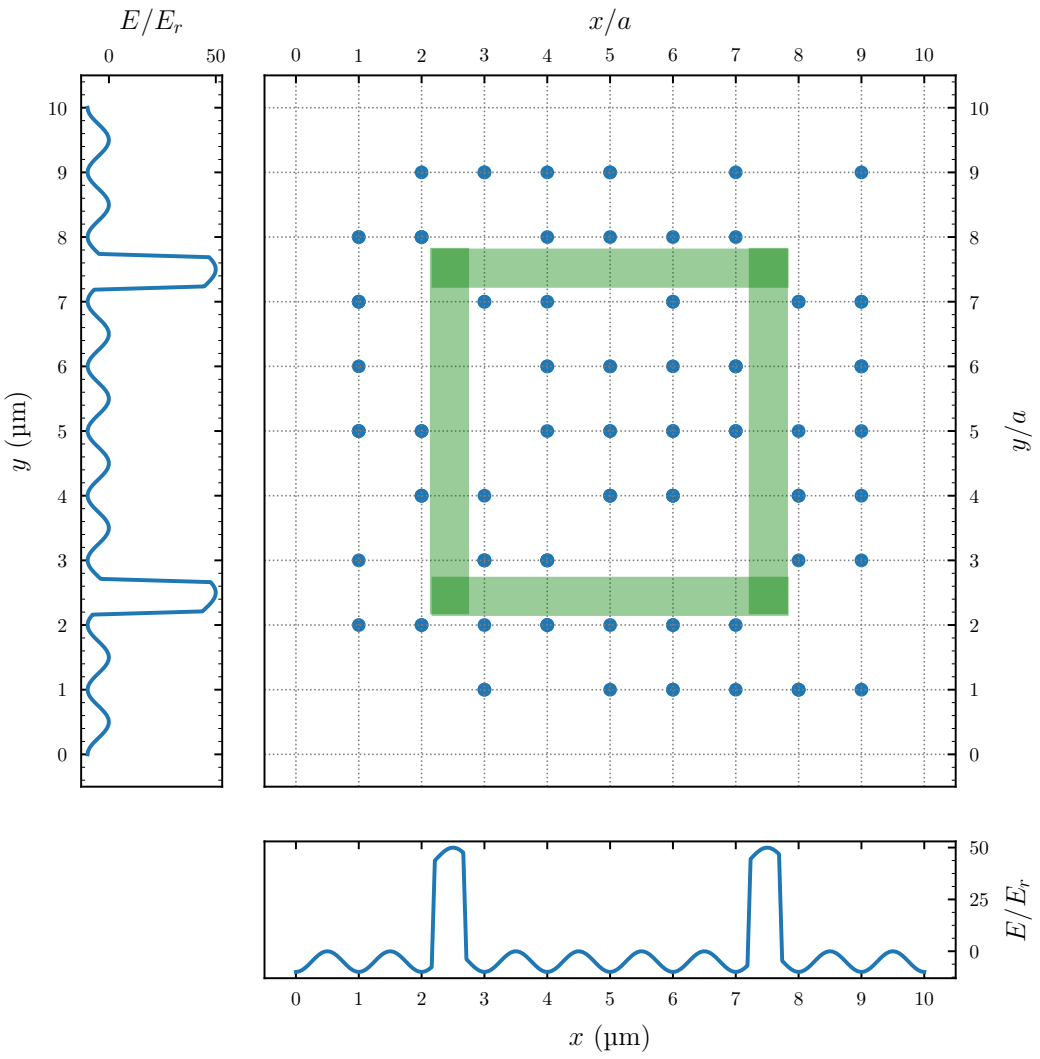

Figure 1.3.: Simple square 2D optical lattice with local barrier potential. The local barrier potential confines atoms inside the green box in a finite homogeneous lattice potential.

one can control tunel coupling between neighboring lattice sites which allows one to confine atoms in an optical lattice without harmonic trap and to study interesting physics at the edges, i.e. topologically protected edge states in the quantum Hall effect, which cannot be studied without sharp edge heights. A similar potential can be realized using attractive local potentials to create a potential pot as illustrated in Figure 1.4. Dynamically controllable high-resolution potentials could be used, for instance, to dynamically shape the global potentials to reach lower entropies

or to generate local potentials that affect only a single lattice site [7, 8, 9]. These are only a few examples, there are, of course, many more applications of locally controllable optical potentials.

High-precision local potentials have been created using high-resolution imaging techniques in combination with digital micromirror devices or spatial light modulators. The generation of high-quality arbitrary potentials is, however, challenging and the degree of dynamical control is limited. Another possibility is the use of arrays of optical tweezers that allow for trapping, stacking and sorting for particles [10], however, there is no tunnel coupling between neighboring sites. An alternative approach consists in the implementation of time-averaged optical potentials. The key concept to create time-averaged local optical potentials is similar to the operation of cathode ray tube screens. The idea is to consecutively illuminate a finite set of points that covers the desired space. A complete passthrough of the finite set has to occur on a time scale short compared to the time scale of the observed processes such that on average the passthrough yields an effective time-averaged potential in the observed process. Yet, only recently, attempts to interact with local particle clusters through high-precision time-averaged optical potentials have been reported [11]. In comparison to the state of the art which uses mechanical mirror arrays for creation of local potentials [11] our approach is based on acousto-optic deflector (AOD). In the following we continue on the ground work laid out in reference [12] which provided us with an optical setup for single-site manipulation using an AOD as well as the discussion of aperture limited Gaussian beam propagation.

We will start with the theoretical foundation of optical lattice potentials and give more details on how the lattice potential is modified under the presence of an additional perturbation potential. From there on we will estimate the required time scale set by the hopping frequency and energy bands of the atoms between neighboring lattice sites. After a short introduction to direct digital signal synthesis we will calculate, if and how the direct-digital synthesizer (DDS) meet the previously determined demands. That in place we can continue with an overview of our experimental setup and results. The experiments separate in a two parts: the first one concerns a detailed understanding of the radio electronics, which powers the AOD and the second one is dedicated to the diffraction efficiency of the laser beam after the AOD, which is influenced by the RF signal and its time-dependence.

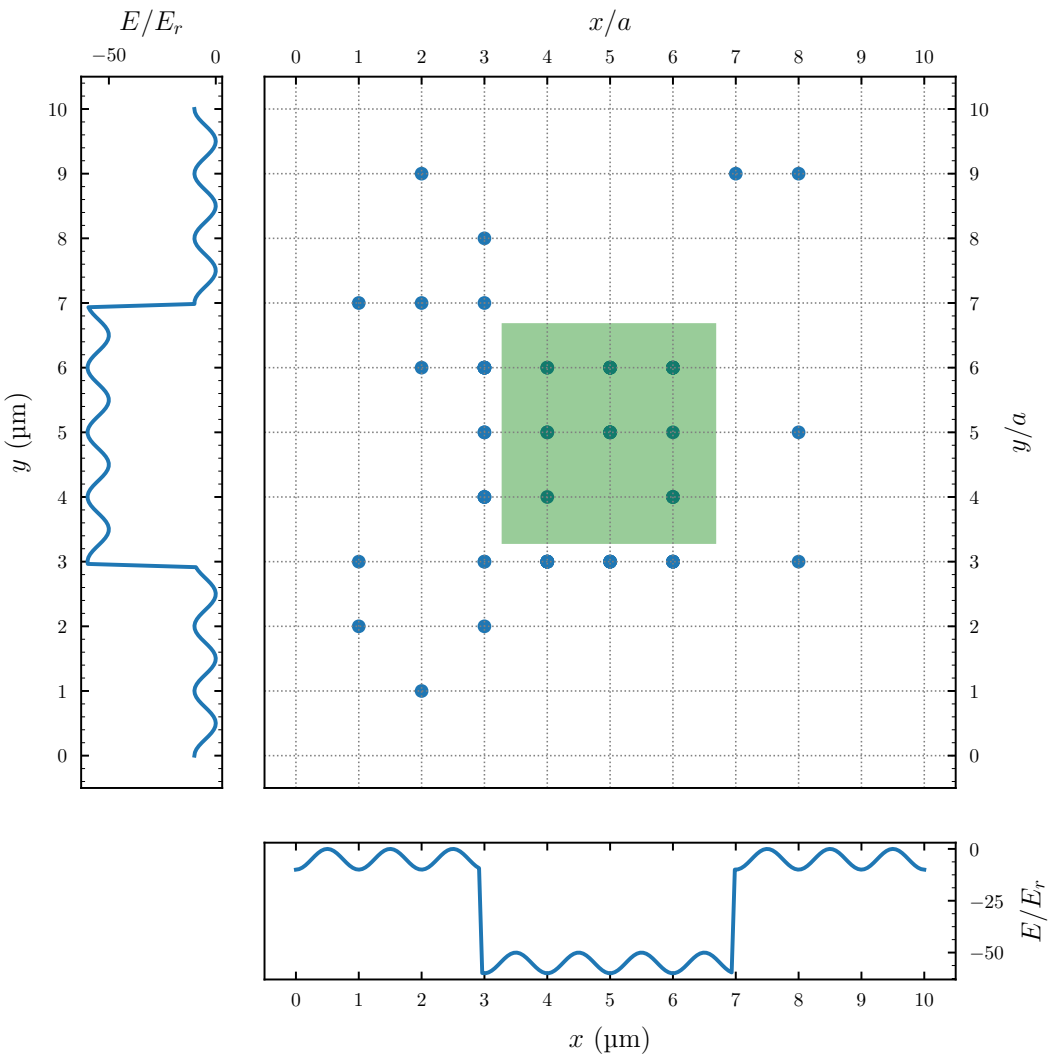

Figure 1.4.: Simple square 2D optical lattice with local pot potential. The local potental pot draws particles from the unperturbated lattice potential to a confined area.

Chapter 2.

Optical potentials

In the introduction we emphasized the importance of optical lattices, yet we left out many details, for instance, how these optical lattices are created and how the optical quantities enter the potential energy of the atoms. In this chapter we will make up for said gaps. First we will recapitulate the theory behind laser light intensities and then derive a formulation of the effective lattice potentials felt by the atoms.

2.1. Atom-light interaction

At first we need to ask ourselves how the laser field acts as a perturbation to the Hamiltonian of the atomic system and how this perturbation leads to an intensity dependent potential for the atoms, which we can control in the experiment. In deviations are loosely based on references [13, 14, 15].

2.1.1. Dipole potential

We will use SI units unless stated otherwise. The Hamiltonian of an electron in an external electromagnetic field reads

$$\hat{H}_{\mathrm{em}} = \frac{1}{2m_e}(\hat{\mathbf{p}} + e\mathbf{A})^2 - e\Phi + \hat{V}_0, \tag{2.1}$$

with vector potential $\mathbf{A}$ and scalar potential Φ of the external field and the Coulomb potential of the nucleus $\hat{V}_0$. Further m_e denotes the electron mass and e the elementary charge. Equation (2.1) is exact for the hydrogen atom that only hosts one electron. For alkali atoms we know that inner electron shells are closed and the single outer electron is approximately described by eq. (2.1). The electromagnetic field relates to the vector and scalar potential through

$$\mathbf{E} = -\boldsymbol{\nabla}\Phi - \frac{\partial \mathbf{A}}{\partial t}, \qquad \mathbf{B} = \boldsymbol{\nabla} \times \mathbf{A}, \tag{2.2}$$

where $\mathbf{E}$ is the electric and $\mathbf{B}$ the magnetic field component.

The canonical momentum $\hat{\mathbf{p}} + e\mathbf{A}$ in eq. (2.1) is difficult to work with. Fortunately Gauge transforms

$$\mathbf{A} \to \mathbf{A} + \boldsymbol{\nabla}\chi \qquad \Phi \to \Phi - \frac{\partial \chi}{\partial t}, \tag{2.3}$$

allow us to simplify eq. (2.1) by choosing a specific Gauge function $\chi(\mathbf{x}, t)$. The Gauge function itself χ does not amend the electromagnetic field components eq. (2.2) which we usually consider to represent physical reality — in contrast to the electromagnetic potentials $\mathbf{A}, \Phi$ which are usually only considered mathematical aid.[1] In the following we choose the gauge function $\chi = -\mathbf{A} \cdot \mathbf{x}$ and assume the dipole approximation $\mathbf{A}(\mathbf{x}, t) \approx \mathbf{A}(t)$. The dipole approximation neglects the spatial variation of the electromagnetic field over the atom and instead assumes a small separation of opposite charges at the nucleus. The dipole approximation is reasonable as wave length of visible light are much larger than atomic length scales [13]. For a rigorous upper error bound on the dipole approximation see Ref. [16]. In the dipole approximation χ satisfies the Coulomb gauge condition $\boldsymbol{\nabla} \cdot \mathbf{A} = 0$ allowing us to set $\Phi = 0$ as no external sources are present [14]. Finally we can rewrite eq. (2.1) as

$$\hat{H}_{\text{dip}} = \frac{\hat{\mathbf{p}}^2}{2m} + \hat{V}_0 + \hat{V}_{\text{dip}} = \hat{H}_0 + \hat{V}_{\text{dip}}, \tag{2.4}$$

with the dipole potential

$$\hat{V}_{\text{dip}} = -\hat{\mathbf{d}} \cdot \mathbf{E}, \tag{2.5}$$

the dipole operator $\hat{\mathbf{d}} = -e\mathbf{x}$ and the spatially homogeneous light field $\mathbf{E}(t)$.

2.1.2. AC-Stark effect

We are now going to solve eq. (2.4) for an arbitrary light field of the form

$$\mathbf{E}(t, \mathbf{x}) = \mathbf{E}_0(\mathbf{x}) \cos(\omega t), \tag{2.6}$$

where $\mathbf{E}_0(\mathbf{x})$ should be compatible with Maxwell's equations and be approximately constant on atomic length scales to not violate the dipole approximation. Further we need the laser frequency ω to be far-off-resonant to the atomic transition frequencies to avoid population dynamics.

At $t < 0$ the system is in the energy eigenstate $|n\rangle$ of the unperturbated Hamiltonian $\hat{H}_0$

$$\hat{H}_0 |n\rangle = E_n |n\rangle = \hbar\omega_n |n\rangle . \tag{2.7}$$

At $t > 0$ the external light field appears immediately. The new state $|\psi\rangle$ can be expanded in the complete basis of the previous energy eigenstates

$$|\psi\rangle = \sum_n c_n(t) e^{-i\omega_n t} |n\rangle . \tag{2.8}$$

Inserting eq. (2.8) into the time-dependent Schrödinger equation with the dipole Hamiltonian eq. (2.4) and applying $\langle m| e^{i\omega_m t}$ to the right hand side leads us to a set of differential equations

$$\dot{c}_m = -\frac{i}{\hbar} \sum_n c_n(t) e^{-i\omega_{nm} t} \langle m| \hat{V}_{\text{dip}} |n\rangle , \tag{2.9}$$

with $\omega_{nm} = \omega_n - \omega_m$. One can read eq. (2.9) as the rate by which the probability amplitude of a state m changes in time. It is equal to the sum of oscillations between states n and m weighted by the current probability of state $c_n(t)$ and the interaction strength. If we are able to solve eq. (2.9) for $c_n(t)$ the population dynamic is entirely described by the time-dependent probabilities $|c_n(t)|^2$. By using eq. (2.6) we can rewrite the dipole transition matrix elements

$$\langle m| \hat{V}_{\text{dip}} |n\rangle = \Omega_{nm}(\mathbf{x}) \cos(\omega t)\hbar, \tag{2.10}$$

[1] The Aharonov-Bohm effect actually provides evidence that aso the electromagnetic potentials represent physical reality.

where we introduced the Rabi frequency

$$\Omega_{nm}(\mathbf{x}) = \langle n| \hat{\mathbf{d}} \cdot \mathbf{E}_0(\mathbf{x}) |m\rangle / \hbar. \tag{2.11}$$

More general expressions for dipole transition elements of one and two electron systems can be found in Reference [17].

Two-level system

From now on we assume a two state system that initially is in the ground state $c_g(0) = 1, c_e(0) = 0$. Under these circumstances the dynamics described in eq. (2.9) simplify to

$$i\dot{c}_g = \Omega_{ge} c_e(t) \cos(\omega t) e^{+i\omega_0 t} \qquad i\dot{c}_e = \Omega_{ge} c_g(t) \cos(\omega t) e^{-i\omega_0 t}. \tag{2.12}$$

Writing $\cos(\omega t)$ in terms of exponential functions and dropping $e^{\pm i(\omega+\omega_{ge})t}$ yields the so-called rotating wave approximation (RWA)

$$i\dot{c}_g \approx \frac{\Omega_{ge}}{2} c_e(t) e^{+i\Delta\omega t} \qquad i\dot{c}_e \approx \frac{\Omega_{ge}}{2} c_g(t) e^{-i\Delta\omega t}, \tag{2.13}$$

where we introduced the frequency detuning $\Delta\omega = |\omega - \omega_0|$. The RWA is motivated by the fact that oscillations of frequency $\omega + \omega_0$ are fast compared to changes in the population dynamics and therefore vanish on average.

We now define $a_g = c_g$ and $a_e = c_e e^{i\Delta\omega t}$ and rewrite eq. (2.13) by

$$i\dot{a}_g = \frac{\Omega_{ge}}{2} a_e(t) \qquad i\dot{a}_e = \frac{\Omega_{ge}}{2} a_g(t) - a_e \Delta\omega. \tag{2.14}$$

Using eq. (2.14) we can diagonalize the Hamiltonian and find the energy eigenvalues to be

$$E_{e,g} = \frac{\hbar}{2} \left(-\Delta\omega \mp \sqrt{\Omega_{ge}^2 + \Delta\omega^2} \right) \approx \mp \frac{\hbar \Omega_{ge}^2}{4\Delta\omega}, \tag{2.15}$$

where we applied a Taylor expansion for $\Omega_{ge}/\Delta\omega \ll 1$ around $\Omega_{ge}/\Delta\omega = 0$ and omitted terms of higher order.

Consequently, atoms in an external off-resonant light field experience an effective periodic lattice potential

$$\hat{V}_{\text{lat}}(\mathbf{x}) = \mp \frac{\hbar \Omega_{ge}^2(\mathbf{x})}{4\Delta\omega} = \mp \frac{d_0^2 E_0^2(\mathbf{x})}{4\hbar\Delta\omega}, \tag{2.16}$$

with dipole element d_0. The sign has to be chosen with respect to the direction of the laser detuning from resonance. If the laser is red-shifted compared to the resonance frequency, $\omega - \omega_0 > 0$, we need to choose the negative sign as the particles are drawn towards the areas of maximum intensity. If the laser is blue-shifted compared to the resonance frequency, $\omega - \omega_0 < 0$, we need to choose the positive sign as the particles are drawn towards the area of minimum intensity. The same results can also be obtained by the use of second order perturbation theory [18].

2.2. Laser light fields

In this section our focus will be on the spatial distribution of the lattice and perturbation laser light fields that create the time-averaged dynamical potentials we discussed in the introduction.

2.2.1. Gaussian beams

The predominant output mode of most lasers is the fundamental transverse gaussian mode. For a laser beam propagating along the z-direction it is described by

$$\mathbf{E}(r,z) = \mathbf{E}_0 \frac{w(0)}{w(z)} \exp\left\{-\frac{r^2}{w(z)^2}\right\} \exp\left\{-ik\left(z + \frac{r^2}{2R(z)} - \arctan\left(\frac{z}{z_R}\right)\right)\right\}, \tag{2.17}$$

where $w(z)$ is the waist radius, $z_R = \pi w(0)^2/\lambda$ the Rayleigh range and $R(z)$ the radius of curvature of the beam's wavefront at position z. Figure 2.1 unveils how the parameters relate to the beam

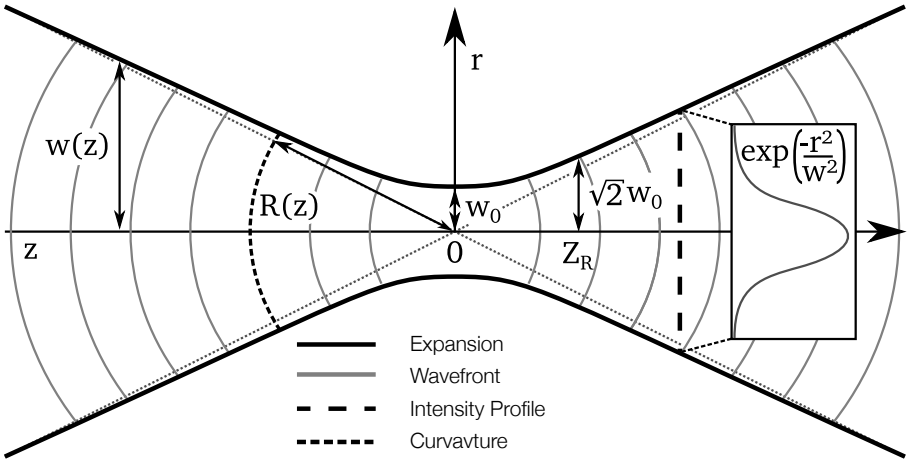

Figure 2.1.: Illustration of Gaussian beam parameters from Ref. [19] translated into English with changed radius of curvature.

profile as a function of propagation distance z. The waist radius $w(z)$ corresponds to the full width at half maximum (FWHM) by $w(z) = FWHM(z)/\sqrt{2\ln 2}$, $R(z)$ relates to the wavefront curvature and z_R is the distance from origin $z = 0$ where the beam waist is $w(z) = \sqrt{2}w(0)$. Beam waist and curvature of radius evolve according to

$$w(z) = w(0)\left[1 + \left(\frac{z}{z_R}\right)^2\right]^{1/2} \qquad R(z) = z\left[1 + \left(\frac{z_R}{z}\right)^2\right]. \tag{2.18}$$

Fortunately eq. (2.16) only depends on the absolute square of the electric field, thus we can drop the complex exponential from eq. (2.17) to find an expression for the Gaussian intensity distribution

$$I(r,z) = I_0\left(\frac{w(0)}{w(z)}\right)^2 \exp\left\{-\frac{2r^2}{w(z)^2}\right\} = I_0 \frac{\exp\left\{-\frac{2r^2}{w(z)^2}\right\}}{1 + \left(\frac{z}{z_R}\right)^2}, \tag{2.19}$$

where I_0 is the maximum intensity at $r = z = 0$.

Lattice intensity

A one-dimensional (1D) optical lattices can be generated through the interference of two counter-propagating Gaussian beams. One way to achieve counter-propagation while keeping the coherence

stable, is to use a mirror. Under the assumption of perfect reflection of the mirror, the electrical field component of the laser beam is described by

$$\begin{aligned}\mathbf{E}_{\rightarrow}(\mathbf{x},t)+\mathbf{E}_{\leftarrow}(\mathbf{x},t) &= \mathbf{E}_0(r,z)\cos(\omega t-kz)+\mathbf{E}_0(r,z)\cos(\omega t+kz)\\ &= 2\mathbf{E}_0(r,z)\cos(kz)\cos(\omega t).\end{aligned}$$

Hence, the intensity distribution equals eq. (2.19) with an additional $4\cos^2(kz)$ factor

$$I(r,z)=4I_0\cos^2(kz)\frac{\exp\left\{-\frac{2r^2}{w(z)^2}\right\}}{1+\left(\frac{z}{z_R}\right)^2}, \tag{2.20}$$

caused by the constructive interference. Table 2.1 lists typical values for a Gaussian beam used

Laser wavelength λ	Lattice constant $a=\lambda/2$	Beam waist $w(0)$	Rayleigh length z_R
1064 nm	532 nm	150 µm	66 mm

Table 2.1.: Typical values for a Gaussian beam used to generate an optical lattice potential.

to construct an optical lattice potential. Typical atom clouds occupy about 50–100 lattice sites spanning over a range of $l=50a\approx 27\,\mu\text{m}$ [20]. As typical atom clouds are much smaller then the typical beam waists used for optical lattices, we have $r/w(z)\ll 1$ and can approximate eq. (2.20)

$$I(r,z)\approx 4I_0\cos^2(kz), \tag{2.21}$$

which we will use from now on as the intensity distribution for 1D optical lattices.

Perturbation intensity

For the generation of optical lattices we want large beam waists because otherwise the potential is not homogeneous and there is a potential energy difference between neighboring lattice sites. For our perturbation potential, however, we need very high resolution on the order of a single lattice site, and therefore need a tightly focused beam. Table 2.2 summarizes the beam parameter of the

Laser wavelength λ	Beam waist $w(0)$	Rayleigh length z_R
532 nm	1 µm	6 µm

Table 2.2.: Typical values for a Gaussian beam used to perturbate the optical lattice potential reported by [12].

perturbation potential as suggested in Ref. [12]. For these parameters approximations made for optical lattice are not valid because of the small beam waist and Rayleigh length and we need to the exact eq. (2.19) formula. In fact for an actual experiment we would like to focus the laser beam to even smaller waists. The ultimate goal would be the ability to address single lattice sites.

2.3. Effective local potentials

With eq. (2.16) we found an expression of the potential energy in terms of atomic properties like the dipole transition element, the atomic resonance and the laser intensity distribution. For the

laser intensity distribution of the optical lattice we derived eq. (2.21) and we concluded that the intensity of the laser used for the creation of local potentials obeys eq. (2.19). If we add these pieces together we can calculate the effective potential with local perturbation as seen by the atoms. We will find that its shape deviates from the idealized local potentials we presented in the introduction in Figure 1.4 and Figure 1.3.

Box

In an first embodiment of local potentials we describe a box potential. A box potential could be used to draw surrounding atoms and confine them to a sharp-edged box. One application for such a box potential would be to replace the currently used harmonic traps imposed on optical lattice structures to prevent atoms to move away from the optical lattice. Figure 2.2 visualizes

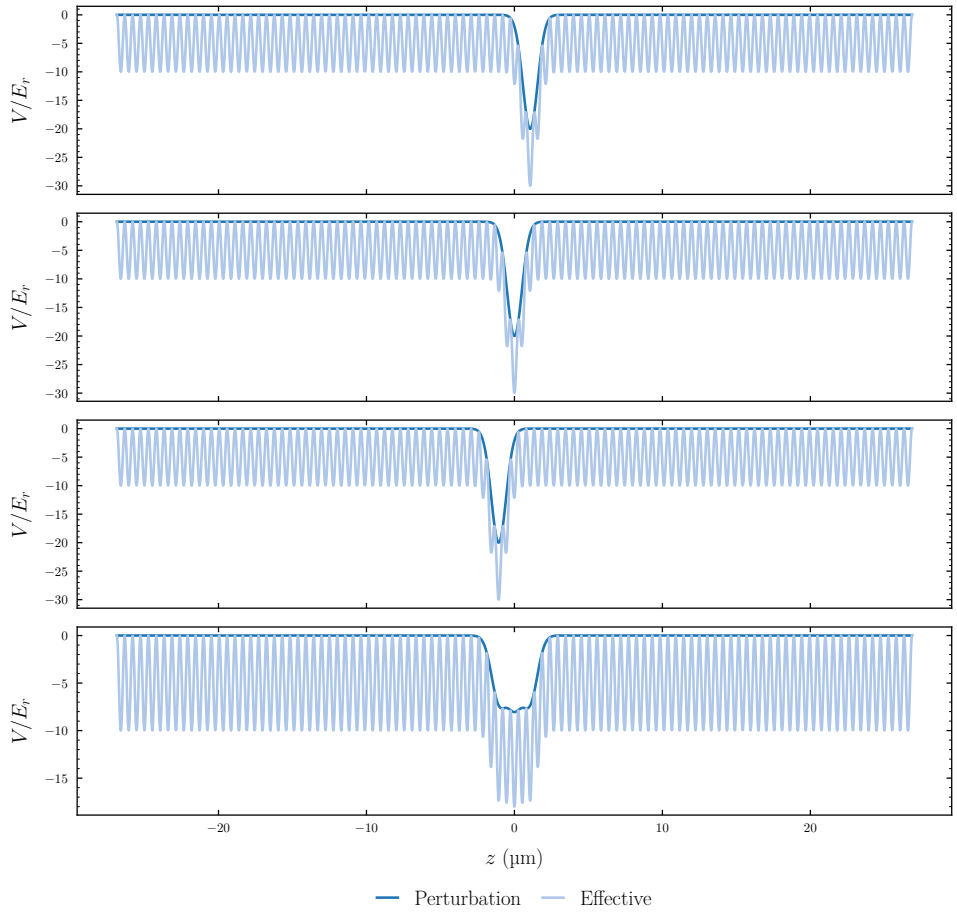

Figure 2.2.: Local pot potential and lattice potential in recoil energies. The pot potential is created by targetting multiple focus points close to each other. Over average this yields a kind of potential valley.

the realization of such a box potential through time-averaged high-resolution perturbation. In the first three plots we see how the perturbation is created at three neighboring lattice sites. In the final plot we see how an average of such a perturbation could look like. We note that the spatial resoltuion of the applied perturbation has to be very high in order to create a flat valley — otherwise one would create additional barriers and/or canyons inside the box. In practice it is

difficult to guarantee such high resolution. Fortunately there is an alternative realization which can be used to confine atoms inside a subregion of an optical lattice.

Barrier

The alternative approach to confine atoms in an optical lattice consists of creating an additive positive barrier potential as depicted in Figure 2.3. For the simple 1D case, it would be sufficient

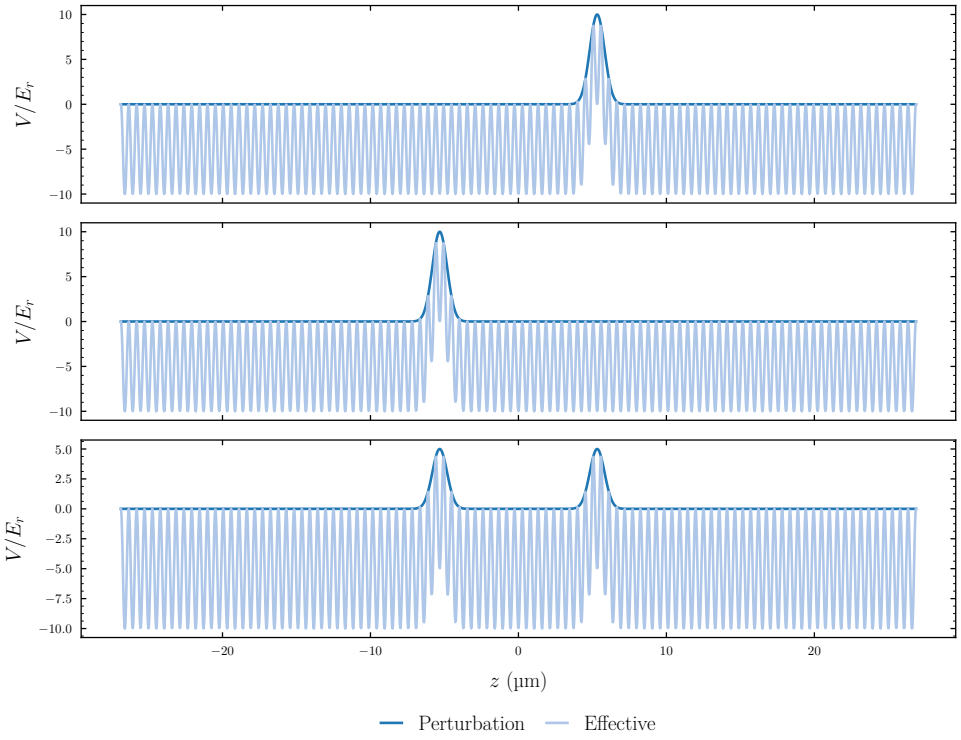

Figure 2.3.: Local barrier potential and lattice potential in recoil energies. The barrier potential is created by targetting two different focus points with the perturbation beam (first two rows). If both focus points are targetted in a sufficiently short period an average potential (last row) can be created.

to alternate the perturbation between two distinct lattice sites. For higher dimensions, however, multiple lattice sites are again necessary with the requirement of high resolution deflection in order to create a continuous barrier. Nevertheless precision demands are slightly lifted compared to the box potential as deflection at overlapping sites will only cause the barrier to be higher.

Chapter 3.

Characteristic energy scales

In the previous chapter we focused on the effective potential obtained by the superposition of the averaged superposition of the perturbation potential and the lattice potential. In this chapter we want to understand the characteristic energy scales in an optical lattice in order to infer the scanning timescales needed for the generation of a time-averaged optical potential the physics that determine the time scale of the perturbation potential.

3.1. Harmonic approximation

Given the optical lattice potential eq. (2.16) the lattice Hamiltonian reads

$$\hat{H}_{\mathrm{lat}} = \frac{\hat{p}^2}{2m} + \hat{V}_{\mathrm{lat}}. \tag{3.1}$$

One first naive approach to solve the time-independent Schrödinger equation subject to the effective lattice Hamiltonian would be to Taylor expand the lattice potential up to second order in kx

$$V_{\mathrm{lat}}(x) = V_0 \cos^2(kx) \approx V_0 \left(1 - \frac{1}{2}(kx)^2\right). \tag{3.2}$$

With eq. (3.2) we get the Hamiltonian of a linear harmonic quantum oscillator

$$\hat{H}_{\mathrm{har}} - V_0 = \frac{\hat{p}^2}{2m} - \frac{1}{2}V_0 k^2 \hat{x}^2, \tag{3.3}$$

with the well-known energy levels

$$E_n = \hbar\omega(2n+1)/2, \quad \omega = \sqrt{|V_0|/m}k = \sqrt{2|V_0|E_r}/\hbar, \tag{3.4}$$

where we introduced the recoil energy $E_r = (\hbar k)^2/(2m)$ as an atom-independent energy scale. In natural scales of the quantum harmonic oscillator we find the time-independent wave functions for the energy level n to be

$$\psi_n(x) = \langle x|\psi\rangle = \frac{\exp\left(-\frac{1}{2}x^2\right)}{\sqrt{2^n n!}\pi^{1/4}} H_n(x), \tag{3.5}$$

where $H_n(x)$ is the nth Hermite polynomial and the spatial coordinate x is expessed in natural length units of $xi = (2E_r/|V_0|)^{1/4}/k$. In Figure 3.1 we have visualized the probability densities of the wave functions of the harmonic approximation for the lattice depth $V_0 = -30E_r$ up to the

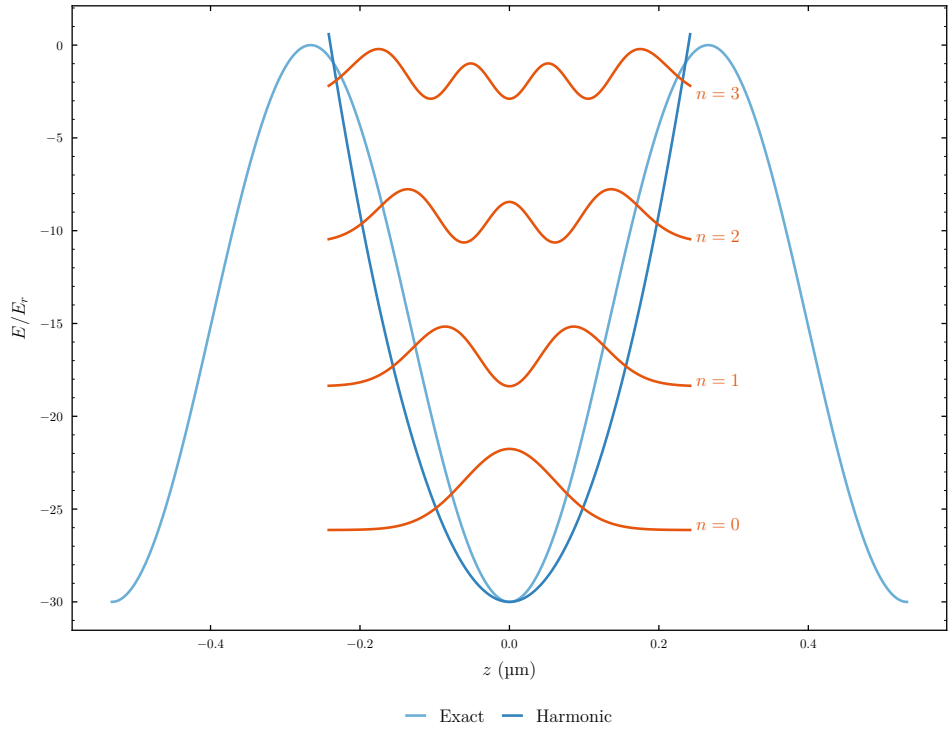

Figure 3.1.: Probability density of the wave functions of the harmonic approximation of the lattice potential.

fourth energy level. The probablity density decays exponentially at the potential boundary and thereby the probability for a particle to tunnel through the lattice potential vanishes. It turns out that the harmonic approximation is not suited for usual lattice depths of below $V_0 = -30E_r$ as we will after comparing the energy levels of the harmonic approximation with the exact energies. Nevertheless the harmonic approximation gives a correct magnitude of the energy while being soft on complexity.

3.2. Lattice structures

The periodicity of the lattice potential eq. (2.16) suggests that there exists a finite representation in the frequency domain. In the context of lattice structures the frequency domain is commonly known as the reciprocal lattice. We will shortly recapitulate the lattice structure basics from Ref. [21]. Let

$$\mathbf{R} = \langle \mathbf{x} | \mathbf{R} \rangle = \sum_{i=1}^{N} n_i \mathbf{a}_i, \quad n_1, \ldots, n_N \in \mathbb{Z}, \tag{3.6}$$

be an element of the Bravais lattice, i.e. a member of the lattice in the spatial domain, with $\mathbf{a}_i$ being the primitive vectors that span the primitive lattice cell. Then the reciprocal lattice is defined as the discrete point set

$$\mathbf{G} = \langle \mathbf{p} | \mathbf{G} \rangle = \sum_{i=1}^{N} m_i \mathbf{b}_i, \quad m_1, \ldots, m_N \in \mathbb{Z}, \tag{3.7}$$

that satisfy the condition $\exp(\mathbf{R}\cdot\mathbf{G})=1$, with $\mathbf{b}_i$ being the reciprocal primitive lattice vector. For a simple cubic lattice structure the reciprocal primitive lattice vector relates to the primitive vector by

$$\mathbf{b}_i = 2\pi\mathbf{a}_i/{\mathbf{a}_i}^2. \tag{3.8}$$

For the subsequent sections we will only consider the one dimensional simple cubic lattice. Cubic lattices of higher dimension, however, can be easily obtained by superposition of the potentials. We now take $|G_u\rangle$ to be the uth reciprocal lattice point. An arbitrary operator $\hat{A}$ with known representation in the spatial domain can be expressed in the recoprocal lattice basis through the transformation

$$\langle G_u|\,\hat{A}\,|G_v\rangle = \int \mathrm{d}x\,\langle G_u|x\rangle^*\,\langle x|\,\hat{A}\,|x\rangle\,\langle G_v|x\rangle = \int \mathrm{d}x\,A(x)e^{2ikx(u-v)}. \tag{3.9}$$

Evaluation of eq. (3.9) for the specific lattice potential found in eq. (2.16) yields

$$\langle G_u|\,\hat{V}_{\mathrm{lat}}\,|G_v\rangle = \frac{1}{4}V_0\left(2\delta^u_v+\delta^u_{v-1}+\delta^s_{u+v}\right), \tag{3.10}$$

which we will later use as matrix elements.

3.3. Bloch states

While eq. (3.10) gives us a simple representation of the periodic lattice potential we are missing an Ansatz for the wave function to solve the time-independent Schrödinger equation. Fortunately Bloch's theorem states that for a periodic potential

$$V_{\mathrm{per}}(x+a)=V_{\mathrm{per}}(x), \tag{3.11}$$

there exists a complete set of wave functions that are energy eigenstates of the Hamiltonian

$$\hat{H}_{\mathrm{per}}=\frac{\hat{\mathbf{p}}^2}{2m}+\hat{V}_{\mathrm{per}}, \tag{3.12}$$

and each of these Bloch waves can be written into the form

$$\left\langle x\middle|\Psi^n_q\right\rangle = \Psi^n_q(x) = e^{iqx}\psi^n_q(x), \tag{3.13}$$

with $\psi^n_q(x+a)=\psi^n_q(x)$, wave vector q and bandindex n. We confine the wave number to the first Brillouin zone $[-k,+k[$, also known as the primitive cell of the reciprocal lattice,

$$q=\frac{ks}{N},\quad s\in[-N,N-1]\cap\mathbb{Z}, \tag{3.14}$$

with N being the number of lattice sites. The discretization arises from the Born-von Karman boundary condition. For a complete proof of Bloch's theorem as well as details on the Born-von Karman boundary condition we refer the reader to Ref. [21] and Ref. [15].

3.4. Energy band structure

Using the Bloch states eq. (3.13) as ansatz to solve eq. (3.1) and noting that by the product rule $\hat{p}^2\Psi^n_q(x)=e^{iqx}(\hat{p}+\hbar q)\psi^n_q(x)$, we find

$$E^n_q\left|\Psi^n_q\right\rangle = \hat{H}_{lat}\left|\Psi^n_q\right\rangle = e^{iqx}\left(\frac{(\hat{p}+\hbar q)^2}{2m}+\hat{V}_{\mathrm{lat}}\right)\left|\psi^n_q\right\rangle. \tag{3.15}$$

Expansion of the state ψ_q^n in states of the reciprocal lattice returns

$$\left|\psi_q^n\right\rangle = \left(\sum_u |G_u\rangle \langle G_u|\right) \left|\psi_q^n\right\rangle = \sum_u \left\langle G_u \middle| \psi_q^n \right\rangle |G_u\rangle = \sum_u c_{uq}^n |G_u\rangle \,, \tag{3.16}$$

where the summation over u is restricted to the number of reciprocal lattice sites one wants to consider for numeric evaluation, or the set of integer numbers in general. The momentum eigenvalues of the state $|G_u\rangle$ can be found by expansion into position space

$$\hat{p}\,|G_s\rangle = \int\int \mathrm{d}x\,\mathrm{d}y\,|y\rangle\,\langle y|\,\hat{p}\,|x\rangle\,\langle x|G_s\rangle\,. \tag{3.17}$$

With $\langle y|\,\hat{p}\,|x\rangle = -i\hbar\delta(y-x)\frac{\mathrm{d}}{\mathrm{d}x}$ we can take the derivative of $\langle x|G_s\rangle = e^{2ikxu}$ and simplify eq. (3.17) down to

$$\hat{p}\,|G_u\rangle = 2\hbar k u \int \mathrm{d}x\,|x\rangle\,\langle x|G_u\rangle = 2\hbar k u\,|G_u\rangle\,. \tag{3.18}$$

Finally we insert eq. (3.16) into eq. (3.15) and apply $\langle G_v|$ to the right hand side while using eq. (3.10) and eq. (3.18), yielding

$$E_q^n c_{vq}^n = c_{vq}^n \frac{(2u+q/k)^2}{2m} E_r + \sum_u c_{uq}^n \,\langle G_v|\,\hat{V}_{\mathrm{lat}}\,|G_u\rangle\,, \tag{3.19}$$

with recoil energy $E_r = \hbar^2 k^2/(2m)$. Using eq. (3.10) we finally find the matrix elements of the lattice Hamiltonian eq. (3.1) to be

$$H_{uv} = \langle G_u|\,\hat{H}_{\mathrm{lat}}\,|G_v\rangle = \begin{cases} (2u+q/k)^2 E_r + \frac{1}{2}V_0, & \text{if } u = v \\ \frac{1}{4}V_0, & \text{if } |u-v| = 1 \\ 0, & \text{otherwise} \end{cases}. \tag{3.20}$$

By choosing a sufficient large matrix dimension, setting its values according to eq. (3.20) and finding its eigenvalues, we are able to reproduce the energy band structure. Table 3.1 lists the

Lattice sites N	Matrix dimension M	Matrix indices u, v
51	60	$-25, -24, \ldots, +24, +25$

Table 3.1.: Parameters used for the lattice Hamiltonian matrix elements to calculate the energy bands.

parameters we choose to calculate the energy bands for the lattice Hamiltonian matrix elements defined in eq. (3.20). The energy band structure for these parameters is depicted in Figure 3.2 for various lattice depths. For $V_0 = 0$ we can see how the confinement to the first Brillouin zone causes the energy band to be reflective at the boundaries of the Brillouin zone. Further we see that with increasing lattice depth the energy spacing increases. In Figure 3.3 we plotted the minimum and maximum energy range for the first four energy bands with increasing lattice depth next to the energy levels of the harmonic approximation. We can see how with increasing lattice depth the energy bands narrow to discrete energy levels as predicted with the harmonic approximation eq. (3.4).

Beside of the energy levels, we know that quantum particles have a non-zero probability amplitude to tunnel through classically forbidden potentials. In our context these quantum tunneling effects are described by the hopping term — an energy which corresponds to the mobility of the atoms in the lattice.

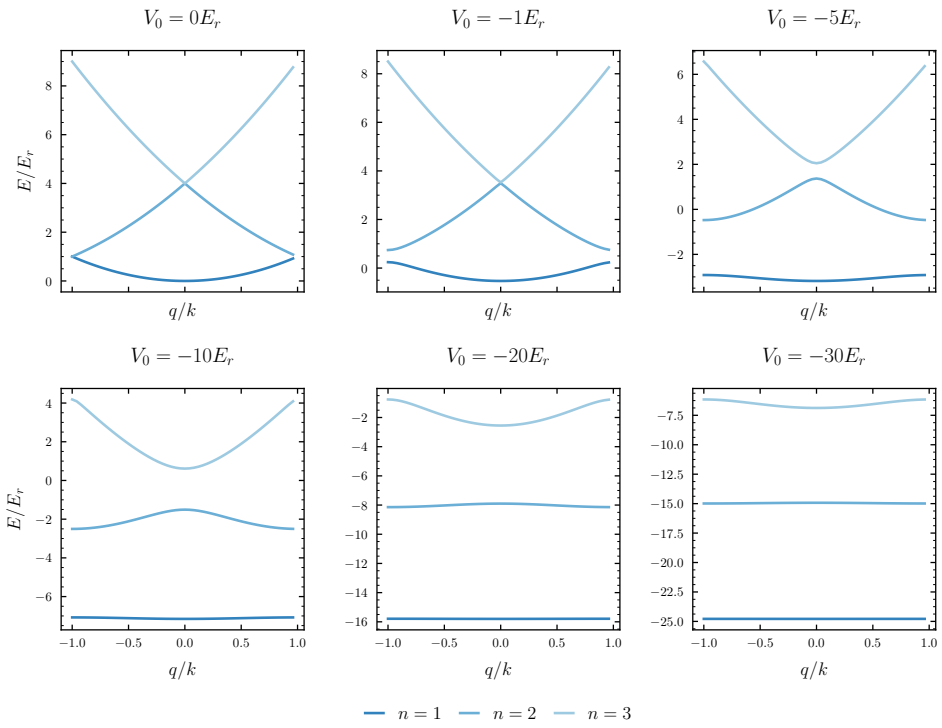

Figure 3.2.: Energy band structure for $N = 51$ lattice sites and various lattice potential depths V_0.

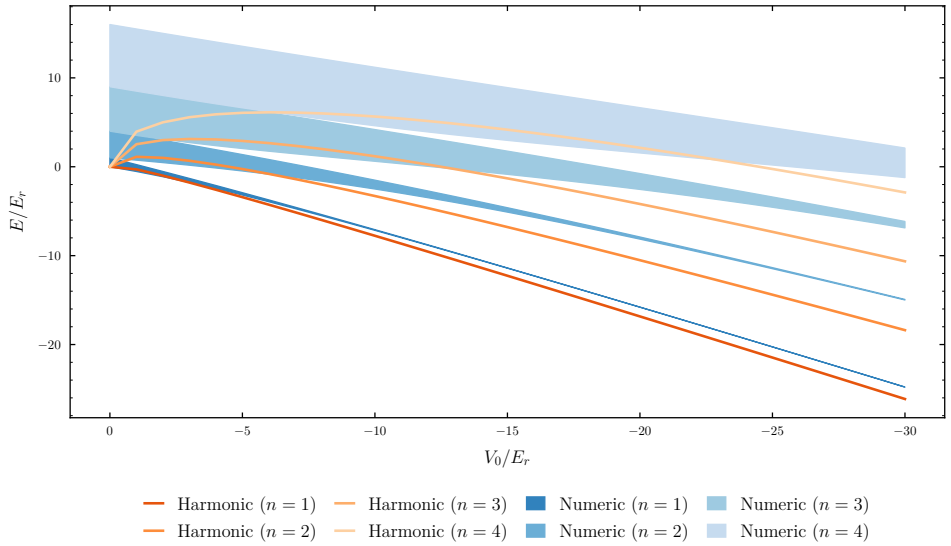

Figure 3.3.: Minimum and maximum energy range for the first four energy bands with the energy levels derived from the harmonic approximation.

3.5. Wannier states

So far we studied the effects of a periodic lattice potential on the energy levels and the Bloch wave functions that are extended over the full lattice. As lattice hopping is a local effect it makes sense to use a more localized basis like the Wannier basis.

The most common definition of the Wannier function with bandindex n on lattice site l reads

$$|\phi_l^n\rangle = \frac{1}{\sqrt{N}} \sum_q e^{-iqla} \left|\Psi_q^n\right\rangle, \tag{3.21}$$

where $\left|\Psi_q^n\right\rangle$ is the Bloch wave function defined in eq. (3.13). The defintion in eq. (3.21) is valid for simple lattice structures, however for more sophisticated lattices the Gauge degree of freedom of the phase of the Bloch states leads to different Wannier states, whereof only one is the maximally localized one [22]. One can find the phase of the Bloch states by minimizing the spread of the Wannier functions defined in eq. (3.21), however there exists an alternative definition that resolves the phase ubiquity. According to this definition the Wannier states are best to construct as the eigenstates of the band projected position operator. The band projector for a band n is defined as

$$\hat{P}_n = \sum_q \left|\Psi_q^n\right\rangle \left\langle\Psi_q^n\right|, \tag{3.22}$$

and the band projected position operator just follows as

$$\hat{x}_n = \hat{P}_n \hat{x}_n \hat{P}_n. \tag{3.23}$$

The Wannier states are now defined as the eigenstates of the eigenvalue equation

$$\hat{x}_n |\phi_l^n\rangle = x_l^n |\phi_l^n\rangle, \tag{3.24}$$

where x_l^n is the lth lattice site in the nth energy band. Choosing the Bloch functions to find the elements of the band projected position operator eq. (3.23) through

$$X_{qq'}^{nn'} = \left\langle\Psi_q^n\right| \hat{x}_n \left|\Psi_{q'}^{n'}\right\rangle = \int_0^{Na} \mathrm{d}x\, \Psi_q^n(x)^* x \Psi_{q'}^{n'}(x), \tag{3.25}$$

provides an analytical expression to calculate the matrix elements [23]. Let d_{lq}^{mn} be the diagonalized matrix $X_{qq'}^{nn'}$ in eq. (3.25) then the Wannier states are fully determined by

$$|\phi_l^n\rangle = \sum_{n,q} d_{lq}^{mn} \left|\Phi_q^n\right\rangle. \tag{3.26}$$

3.6. Hopping energy

With the previous tools in place we are now set to give an expression for the tunneling matrix element between neighboring lattice sites. We define the hopping from lattice site l to lattice site l' for bandindex n as

$$J_{l-l'}^n = -\langle\phi_l^n| \hat{H}_{\mathrm{lat}} |\phi_{l'}^n\rangle. \tag{3.27}$$

Using the common definition of the Wannier states eq. (3.21) for eq. (3.27) we find

$$J_{l-l'}^n = -\frac{1}{N} \sum_{q,q'} e^{iqa(l-l')} \left\langle\Psi_q^n\right| \hat{H}_{\mathrm{lat}} \left|\Psi_{q'}^n\right\rangle. \tag{3.28}$$

The Bloch states are energy eigenstates eq. (3.19) and orthonormal, henceforth

$$J^n_{l-l'} = -\frac{1}{N}\sum_q E^n_q e^{iqa(l-l')}, \tag{3.29}$$

where the sum covers all allowed q as defined in eq. (3.14). Expression eq. (3.29) is exact for a given number of lattice sites N and can be evaluated numerically. The form of eq. (3.29) resembles a discrete Fourier transform. The inverse Fourier transform gives us the energies in terms of the hopping probabilites

$$E^n_q = \sum_{l-l'} J^n_{l-l'} e^{-iqa(l-l')}, \tag{3.30}$$

where the sum runs from $l - l' = -N$ to $l - l' = +N$.

3.6.1. Nearest-neighbor approximation

For deep potentials $V_0 \gtrapprox -3E_r$ hopping only contributes from direct neighbour sites [20], thus we can abort the sum in eq. (3.30) for $|l - l'| > 1$

$$E^n_q \approx J^n_{l+1-l} e^{-iqa} + J^n_{l-1-l} e^{+iqa} + J^n_{l-l} = J^n_0 + 2J^n_1 \cos(qa), \tag{3.31}$$

where we have used $J^n_{-1} = J^n_{+1} = J_1$ because of translation invariance. Evaluation of J^n_0 using eq. (3.27) tells us that J^n_0 just is the average energy of an energy band. Evaluation of eq. (3.31) at $q = 0$ and $q = k$ and subtracting the results from eachother yields us the tight-binding approximation

$$J^n_1 \approx \frac{1}{4}\left(E^n_k - E^n_0\right), \tag{3.32}$$

which assumes a $\cos(qa)$ shaped energy band. Further [1] reports an analytical proxmity

$$J^n_1 \approx \frac{4}{\sqrt{\pi}}\left(\frac{V_0}{E_r}\right)^{3/4} \exp\left(-2\sqrt{V_0/E_r}\right), \tag{3.33}$$

to be valid for sinusoidal potentials like eq. (2.16) and to be derived from the Mathieu equation. The Mathieu equation can be obtained from the time-independent Schrödinger equation with $V_0 \cos^2(kx) = \frac{1}{2}V_0\left(1 - \cos(2kx)\right)$. In Ref. [24] we found a more elaborate deviation of eq. (3.33). Figure 3.4 compares the exact numerical calculations using eq. (3.29) for $l - l' = 1$, the tight-

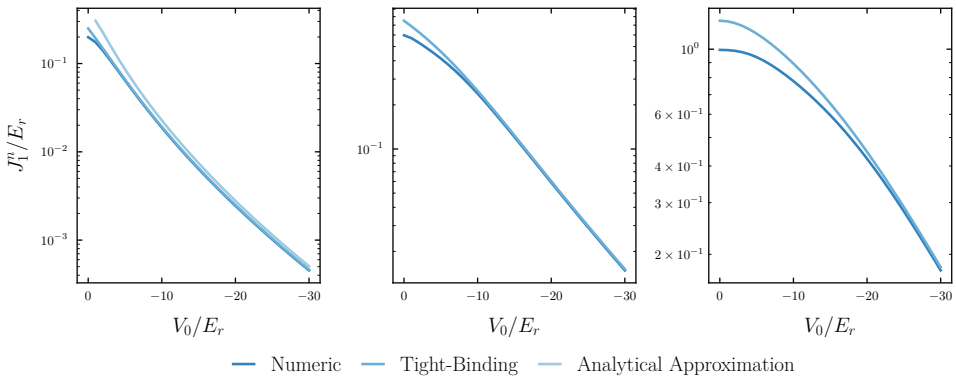

Figure 3.4.: Nearest-neighbor hopping energy derived from the exact numerical calculations, the tight-binding approximation and an analytical proxmity eq. (3.33).

binding approximation defined in eq. (3.32) and an analytical approximation eq. (3.33). We note

that the tight-binding approximation and the exact calculations converge already for small lattice depths for the first energy band and for medium lattice depths for the second energy band. For the third and higher energy bands the numerical evaluation should be used. From now on we

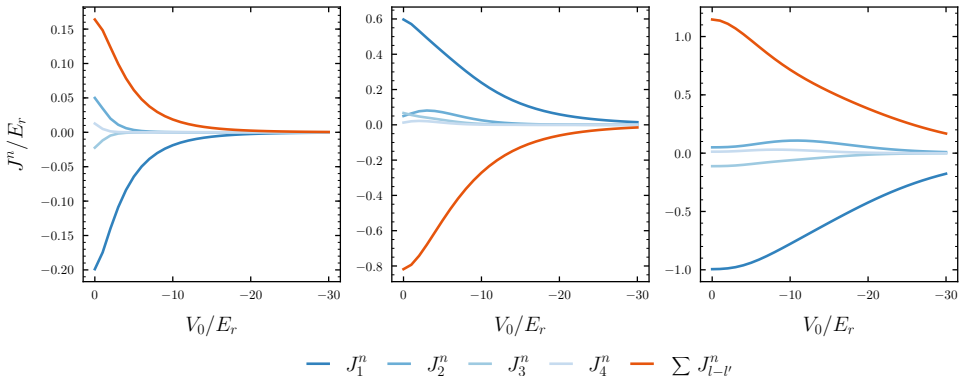

Figure 3.5.: Hopping energies for different neighbour ranges.

will use the exact numerical calculation of the hopping energy. In Figure 3.5 we calculated the hopping terms using eq. (3.29) for different $l - l'$ as well as a sum over all $l - l'$. We can see that the nearest-neighbor term J_1^n is most dominant, and, except for the second energy band, greater than the sum over all hopping terms. Because of this and the fact that perturbation potential is about the size of a single lattice site, as we have seen in the previous chapter, we will reduce ourselves to the nearest-neighbor hopping term J_1^n.

3.7. Conclusion

Through the Planck-Einstein formula $E = hf$, one can express energies as frequencies. We have

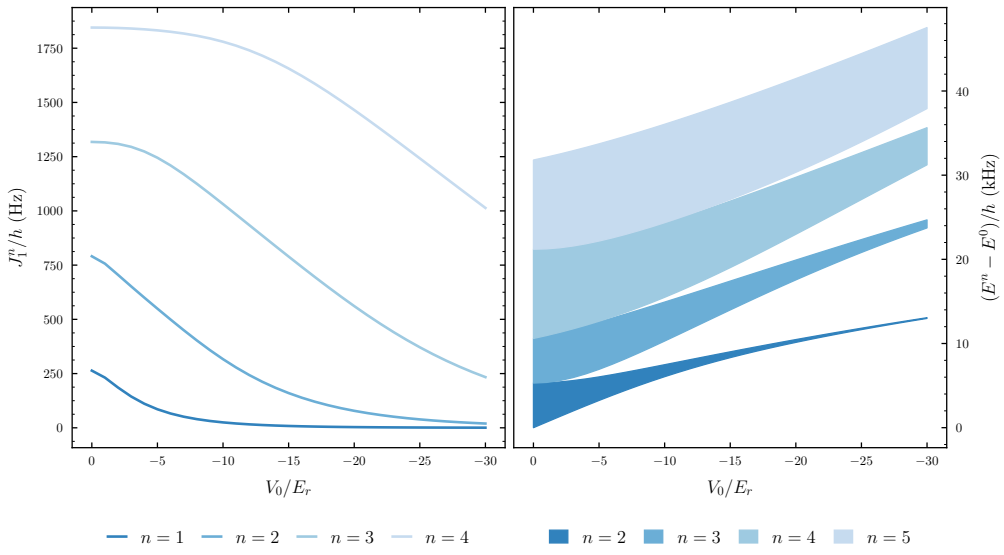

Figure 3.6.: Nearest-neighbor hopping energy as frequency and relative energy band differences with respect as frequency.

used $f = E/h$ to express the nearest-neighbor hopping and band energies relative to ground level as frequency. The so obtained frequencies should give us the magnitude of the sweep frequencies used for our envisioned perturbation potential in order for the time-average to hold. Figure 3.6 discloses the frequencies of hopping and band energies relative to the first energy band. We note that the hopping frequencies of the first four energy bands are in the single digit kHz range while the energy band frequencies of the first four energy bands releative to the first energy band go up to 40 kHz. The energy band frequencies are obviously higher then the hopping frequency, and thus should be a better upper bound. Regardless, it is left for discussion if the hopping frequencies are not more relevant for the ungoing physics. For the now we will take 50 kHz as an upper bound for generation of time-averaged potentials. This relates to a maximum duration of 20 µs the perturbation laser beam should spent between being deflected to the same lattice site.

Chapter 4.

Experimental setup

The exerimental setup was largely adopted from Ref. [12] and we will only give a brief summary including a short characterization. Amendments we made include the RF signal source of the AOD.

4.1. Optics

We start by describing the optical aspects of our setup. The main component of this work is the AOD. We will describe some of its properties below and then head on to the optical setup.

4.1.1. Acousto-optic deflectors

A schematic drawing of the AOD is depicted in Figure 4.1. We see the two AOD elements in the respective horizontal and vertical slot. The internals of the vertical AOD (left-hand side) are illustrated. The element itself spans through the casing (dashed line) while the acousto-optic crystal (dotted line) is glued onto the element. The laser beam (green) passes through the acousto-optic crystal. In the following we will refer to the horizontal AOD element as the AOD element anticipated for the horizontal slot and accordingly to the vertical AOD element as the AOD element intended for the vertical AOD socket. Under the assumption of a light polarized

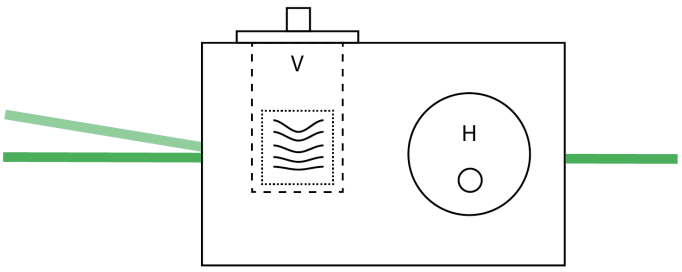

Figure 4.1.: Drawing of the used 2D AOD.

perpendicular or parallel to the elastic waves under normal incident angle Ref. [25] reports that

the acousto-optic acts as a diffraction grating with

$$\sin\theta_n = \pm n\frac{\lambda}{\Lambda}, \tag{4.1}$$

where θ_n denotes the angle of the nth diffraction order, λ the laser wavelength and Λ the wavelength of the elastic wave inside the acousto-optic crystal.

Ref. [12] discloses a linear model for the spatial resolution in the atomic plane in terms of the AOD frequencies

$$x(f_h)/\mu\text{m} = 3.66\frac{f_h}{1\,\text{MHz}} - 379 \qquad y(f_v)/\mu\text{m} = 3.62\frac{f_v}{1\,\text{MHz}} - 360, \tag{4.2}$$

wherein f_h, f_v denote the frequencies applied to the horizontal (H) respective vertical (V) AOD.

4.1.2. Setup

The optical setup can be disected into two parts: a closed first section that reduces the power of the 532 nm laser source from 10 W to below 2 mW, it also includes an acousto-optic modulator (AOM) for intensity regulation. The second section is the actual setup where a 2D AOD is used to manipulate the angle of the laser beam in order to dynamically control the position of the tightly-focused laser beam in the imaging plane. Both sections are connected through a single-mode optical fiber (SMF).

First section: power reduction

Because of safety concerns the power reduction section is confined into a visually sealed box housing. Figure 4.2 reveals the inside of the power reduction setup. The laser beam leaving the

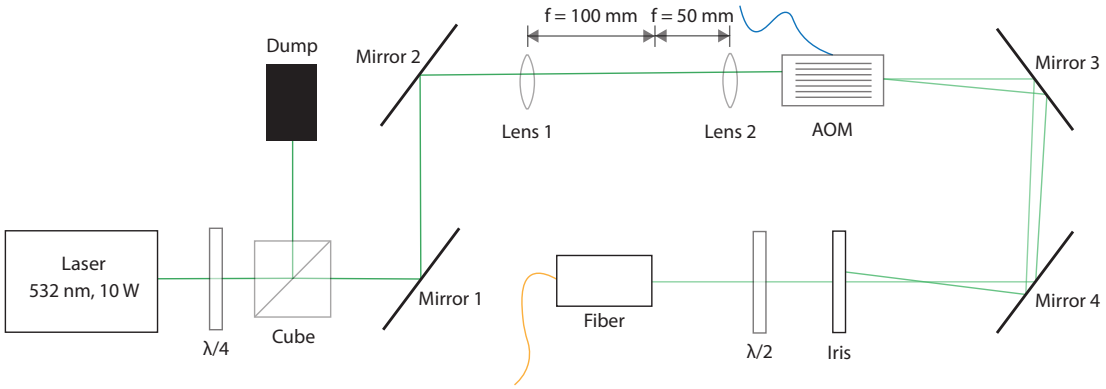

Figure 4.2.: Optical configuration of the power reduction section.

laser source is linearly polarized. In order to divert the majority of the power into a beam dump we use a $\lambda/2$ retarder plate and a high-power polarizing beam splitter. Afterwards Mirror 1 and Mirror 2 direct the beam towards the center of a $2:1$ telescope composed of Lens 1 and Lens 2. The telescope is there to reduce the beam diameter by 2 in order to avoid cut-off at the aperture of the subsequent AOM. The AOM diffracts the laser beam into multiple orders as it acts as a tunable diffraction grating. Mirror 3 and Mirror 4 direct these orders onto a pinhole which is

configured to intromit only the first order deflection. The power in the first diffraction order can be controlled by changing the RF power sent to the AOM. Finally a $\lambda/2$ retarder plate is used together with Mirror 3 and Mirror 4 to couple the beam into the polarization-maintaining SMF.

Beam deflection and detection

The section for beam deflection and detection as disclosed in Figure 4.3 receives the down-powered laser beam from the previously described section by a SMF. Hereinafter the beam passes a rotatable retarder plate and beam splitter Cube 1 to clean the polarization of the laser beam after passing through the SMF. A second polarizer with Cube 2 is used to branch off a part of the beam to Photodiode 1 that is positioned to be at the focal point of Lens 1. Photodiode 1 is connected via a feedback loop with the amplitude modulation of the AOM depicted in Figure 4.2 to stabilize the laser intensity against, for instance, thermal drifts. For horizontal and vertical beam deflection

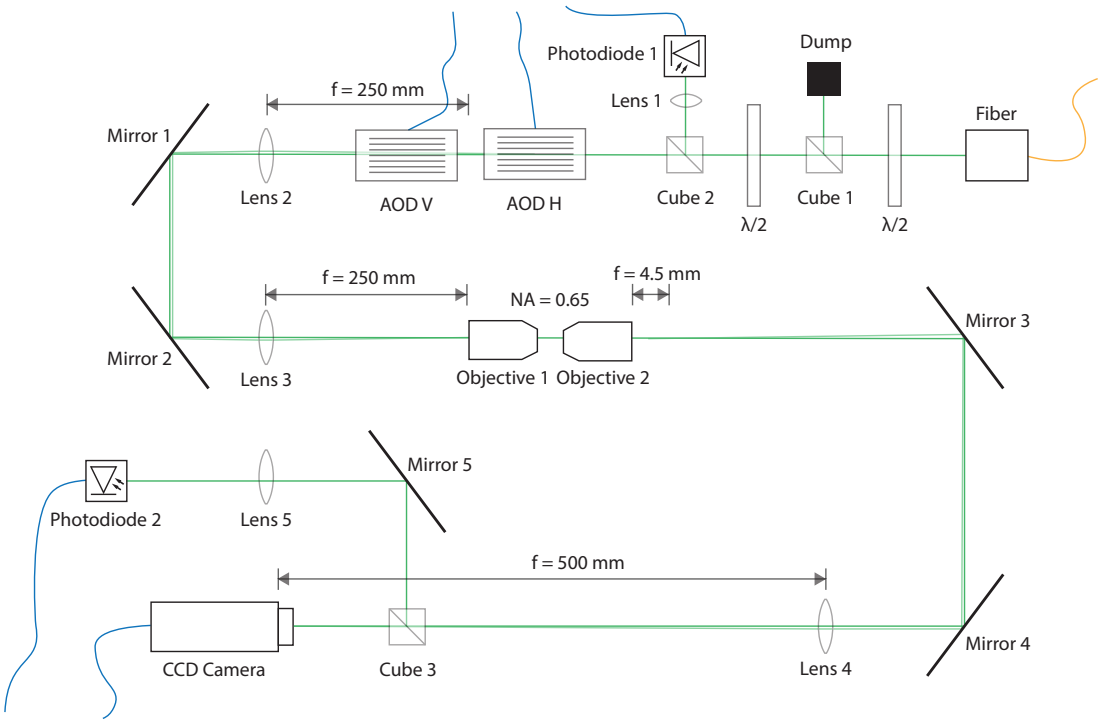

Figure 4.3.: Optical configuration of the beam deflection section.

two AODs are used. A 1 : 1 telescope comprised of two lenses (Lens 2 and Lens 3) is used to image the beam on a pair of objectives. The purpose of the first objective is to translate a change in the incident angle to a position offset in the atom plane. The components described so far are sufficient to offset a high-resolution pertubation laser perpendicular to the atomic plane. The purpose of the other components is to unfocus the laser back for detection. Combining the the focal length of the (second) objective f_{obj} with the focal length of f_4 we achieve a magnification of

$$M = \frac{f_4}{f_{\mathrm{obj}}} = \frac{500\,\mathrm{mm}}{4.5\,\mathrm{mm}} \approx 111. \tag{4.3}$$

The so colliminated and magnified laser beam is then imaged onto the charge-coupled device (CCD) camera sensor. Cube 3 forks a portion of the beam away from the CCD camera on Mirror 5 that guides the beam towards Lens 5 in order to focus the beam onto Photodiode 2. It is

important that the sensor of Photodiode 2 is positioned on the focal spot of Lens 5, otherwise the laser beam would leave the sensor when deflected by the AOD.

4.2. Electronics

Beforehand we described the optical setups used. Now we want to emphasize on the electronics and how they are integrated into the optical setup.

In Figure 4.4a the electronic setup of the AOM control loop is presented. The DDS signal source outputs a 80 MHz RF signal which is amplified and then supplied to the AOM for intensity modulation, see Figure 4.2. Photodiode 1 measures the modulated laser intensity and is connected to a proportional-integral-derivative controller (PID). The PID outputs a signal proportional to the deviation of the measured intensity from the configured intensity which is provided to the amplitude modulation input of the power amplifier. In Figure 4.4b the electronic setup connecting

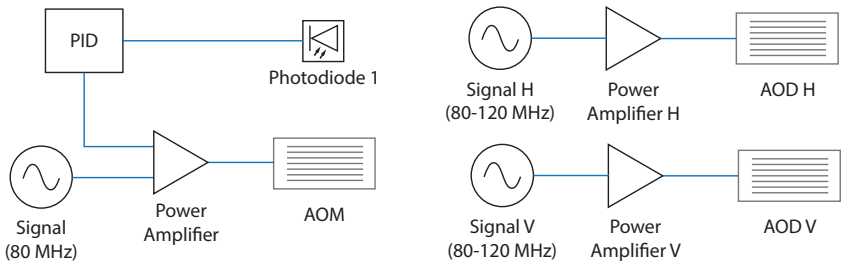

(a) Intensity control via AOM. (b) Deflection control via AOD.

Figure 4.4.: Electronic setup used to control the electro-optic devices.

the 2D AOD with the DDS signal sources are presented. The DDS output is configured through a network interface as we will explain later. Furthermore there is a reference signal source (not shown) that provides a 10 MHz reference signal to the DDS. First we will elaborate on the general components used in Figure 4.4 as well as our experiments.

4.2.1. Signal source

We require the signal source to generate a sinusoidal RF signal

$$x(t) = A\cos\left(2\pi f t\right), \tag{4.4}$$

where $0 \leq A \leq 1$ denotes the amplitude and f the frequency. For the AOM setup in Figure 4.4a it is sufficient to configure a constant frequency $f = 80\,\text{MHz}$ and amplitude $A = 1$, which is further varied by the feedback loop. For the AOD control, however, our requirements are beyond a constant signal. Ideally we would like to program a time-dependent amplitude $A(t)$ and frequency $f(t)$, supplementary to the support of an external trigger signal in order to syncronize multiple signal sources. For our setup we chose to use DDS as signal sources as they provide high frequency resolution, a wide range of modulation options and are cheap compared to signal generators. In chapter 6 we will give a more detailed view of the characteristics and limitations of the AD9910, the DDS integrated circuit (IC) we use as signal source.

4.2.2. Power amplifier

We use three signal amplifiers with respective input from the signal sources to have an output power of about $P = 2\,\mathrm{W}$ required by the AODs and the AOM for maximum diffraction efficiency. The used amplifiers offer a second input for external amplitude modulation. In case of the AOM we connect this input to the output of the feedback loop.

4.2.3. PID controller

A feedback loop takes a reference $r(t)$, also called setpoint, and a process variable $y(t)$ as input and outputs the value for a control variable $u(t)$, which in turn, affects the process that determines $y(t)$. A PID is a specific implementation of such a feedback loop that uses a proportional, differential and integrative term to estimate the control variable $u(t)$. In Figure 4.5 we see a block diagram

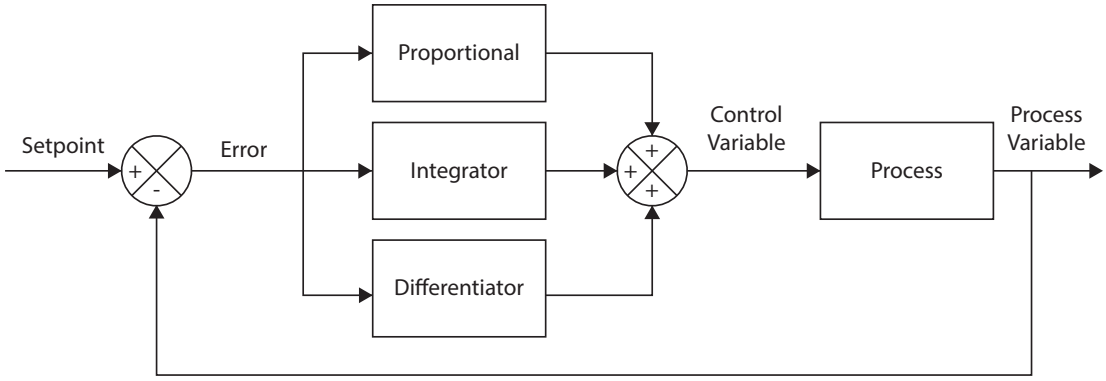

Figure 4.5.: Block diagram of a PID feedback loop.

of a PID. The error values is supplied to the proportional block as well as the differentiator and integrator which in sum give the updated control variable value $u(t)$. The process changes with $u(t)$ and we read off the process variable $y(t)$ we want to regulate and feed it back to the start of the loop. The control variable of the PID can be expressed through

$$u(t) = K_p e(t) + K_i \int_0^t \mathrm{d}t'\, e(t') + K_d \frac{\mathrm{d}t}{\mathrm{d}e(t)}, \tag{4.5}$$

where K_p, K_i, K_d denote the coefficients of the respective terms. The ideal values for the coefficients have to be found by loop tuning for each application. Every term contributing to eq. (4.5) can be thought of to account for a different time scale of the process: the proportional term considers the momentary error, the differential predicts trends and the integrator corrects for past errors. For our particular application the control variable is the amplitude $A(t)$ supplied to the modulation input of the power amplifier of the AOM RF signal. The process variable of our PID is the voltage measured at Photodiode 1.

4.2.4. Trigger source

To syncronize the signal sources, the CCD camera and the oscilloscope it was necessary to design a network programable trigger source that outputs a square pulse and forwards it to multiple devices. The schematics, board layout and source code can be found in the Appendix A.1.

4.3. Communication

In the last section of this chapter we will see that the diffraction efficiency of the AODs is not constant and requires readjustment by amplitude modulation of the RF signal supplied to the AODs. We consider this readjustment step as a calibration process. The efficienct implementation of such a calibration process requires an orchestrated interplay of different electronic devices which we will discuss now. In Figure 4.6 the communication setup of our electronic devices is illustrated.

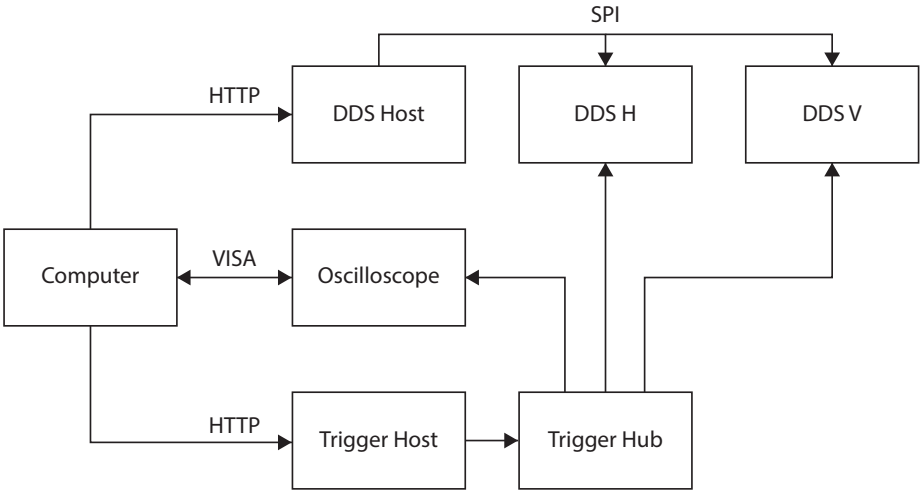

Figure 4.6.: Communication setup of the electronic devices in the experimental setup.

The computer, the trigger host, the oscilloscope and the DDS host are connected to the local area network (LAN). The trigger host and the DDS host are both BeagleBone Black (BBB) that run a hypertext transport protocol (HTTP) server from which the computer can change parameters over the network. The implementation of the HTTP server of the trigger host as well as the schematics of the trigger hub can be found in Appendix A.1. The HTTP service that runs on the DDS host also contains a driver which writes the DDS parameters over to the respective DDS board. The oscilloscope can be controlled through virtual instrument software architecture (VISA). In Listing 4.1 we can see an examplary measurement using a Python module we wrote to abstract away the interaction with the setup.

```python
import time
import control

# enable 100 MHz AOM signal
control.aom()

# supply 100 MHz signal at 80% amplitude to AOD H
control.aod_h(amplitude=.8, frequency=100e6)

# supply 80 to 120 MHz chirp at 100% amplitude to AOD V on trigger
control.aod_v(frequency=[80e6, 120e6], duration=20e-3)

# initialize scope connection
scope = control.MSOX6004A('172.22.22.30')

# put scope into SINGLE mode to capture a single measurement
scope.single()

# wait 1 s until scope is ready
time.sleep(1)

# fire the trigger signal to scope and dds
control.trigger()

# wait 2 s until scope is ready
time.sleep(2)

# load the voltage trace from scope
scope.data()
```

Listing 4.1.: Example usage of the Python module to control the setup.

4.4. Trial run

After we integrated the DDS into the experimental setup, we wanted to test its capabilities. Therefore we wrote a simple script that transforms short letter sequences to a list of frequency pairs that we can playback from the H and V DDS. In Figure 4.7 we see the projected text as captured by the camera. The text projection is created by iterating through a set of frequency pairs, which as we know, correspond to a position offset. For a sufficient exposure of the CCD camera we can capture a time average over all single points just as we plan to do with the optical potentials. Even though we configured the DDS with constant amplitude, we notice that the illumination is not homogenous. In fact we will see that the diffraction efficiency of the AOD depends heavy on the frequency and it will turn out to be a challenging endeavour trying to compensate for this dependency as we will see in the final part of this thesis.

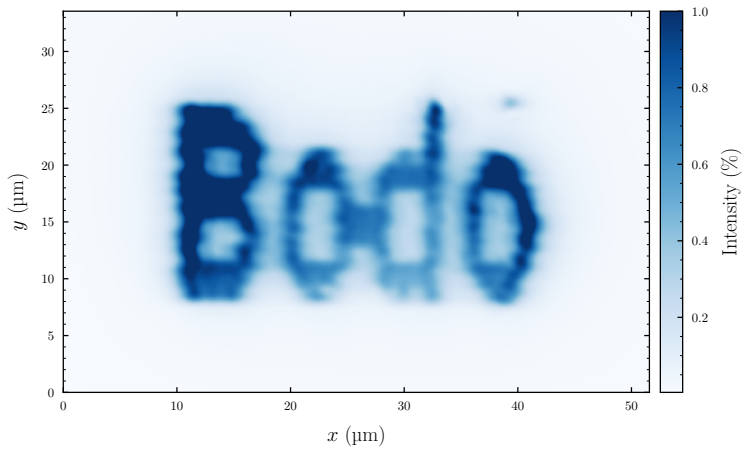

Figure 4.7.: Text projection as captured by the CCD camera.

Chapter 5.

Characterisation of the optical setup

In this short chapter we want to characterize the optical setup introduced in Chapter 4. In particular we want to estimate the performance of the intensity feedback loop and the quality of our alignment by comparing the beam profile with the results reported in Ref. [12].

5.1. Intensity control

In Chapter 4 we stated that the laser intensity is regulated by a control loop using an AOM in the power reduction setup. Without the additional intensity regulation we would observe various intensity drifts from the laser source throughout the measurements as depicted in Figure 5.1 where we can observe short- and long-term oscillations over a large intensity range. The setup used to

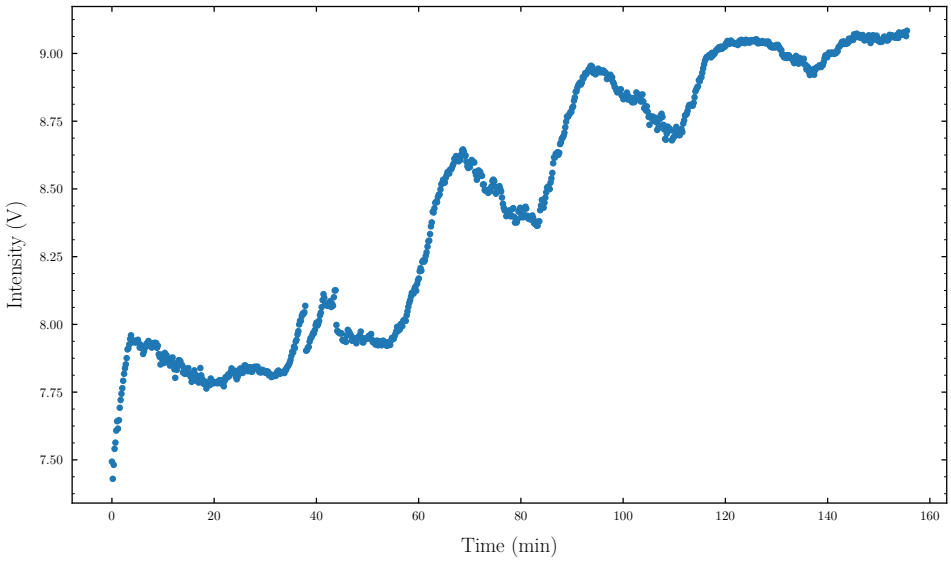

Figure 5.1.: Time evolution of the uncontrolled laser intensity.

record the intensity evolutions is disclosed in Figure 5.2. It differs from the optical setup described

in Chapter 4 by the absence of the AOD and the relocation of Photodiode 2 at the end of the laser beam. The photodiode gain of Photodiode 2 was lowered from 70 dB to 50 dB because the lack of AODs would otherwise cause the photodiode to saturate due to higher intensities. In

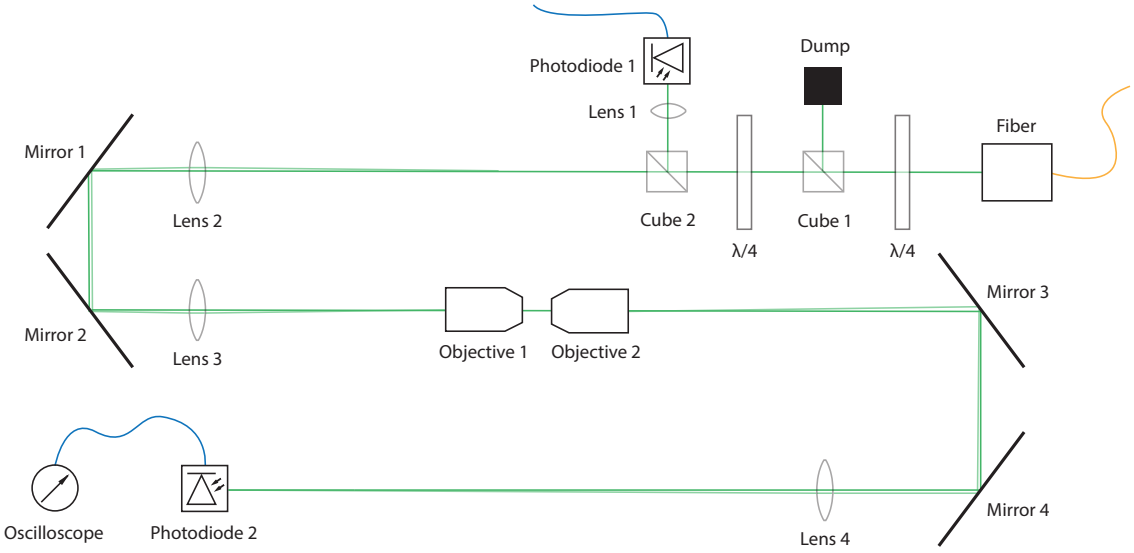

Figure 5.2.: Optical setup and intensity detection. The beam hits Photodiode 2 which is connected to the oscilloscope.

order to to estimate the error contribution due to imperfect intensity regulation, we will conduct a short- and a long-term measurement of the stabilized intensity. Technically a typical photodiode measurement takes about a fraction of a millisecond, yet we can decide on different intervals between the measurements in order to separate short-term from long-term trends like the ones noted in the uncontrolled meausrement. Table 5.1 summarizes the different time scales for the conducted short- and long-term measurement of the intensity control. The voltage time series for

	Short	Long	AOD
Interval	10 s	120 s	3 s
Duration	1 h	16 h	<2 h

Table 5.1.: Interval and duration times of the short- and long-term measurement as well as a typical AOD frequency sweep measurement.

both intensity control measurements are presented in Figure 5.3. The outlier at about 22:45 h was caused by accidently interfering with the setup during measurement. Beside of that incident the long-term intensity seems stable. On a smaller timescale we see that the intensity evolution performs periodic oscillations. Overall we can confirm that the intensity control loop successfully holds the intensity mean, though with small oscillations. In order to estimate the relevance of these small oscillations of the controlled intensity for later measurements, we performed a measurement of the intensity variations introduced by the AOD subject to constant frequency increments for comparison. Table 5.2 presents the statistics of said intensity measurements. We should note that not all of the statistical measurements are directly comparable because of the 20 dB higher photodiode gain used in the AOD frequency sweep measurement. Nevertheless we can directly compare the uncontrolled and the controlled short- and long-term measurements directly. As we divide by the mean μ, the relative standard deviation σ/μ is a scale invariant statistical measure and thereby comparable through measurements conducted with different photodiode gain setting. Comparing the relative standard deviation yields that the intensity drifts are small on a short

Measure	Not-Stabilized	Long	Short	AOD
Mean μ	8.45 V	6.79 V	6.79 V	1.95 V
Minimum	7.43 V	4.88 V	6.77 V	0.00 V
Maximum	6.82 V	6.86 V	6.82 V	9.08 V
Standard Deviation σ	0.49 V	0.09 V	0.01 V	0.54 V
Relative Standard Deviation σ/μ	5.75 %	1.35 %	0.19 %	27.69 %

Table 5.2.: Descriptive statistics of not-stabilized and actively stabilized short- and long-term intensity evolutions as well as a typical AOD frequency sweep measurement for comparison.

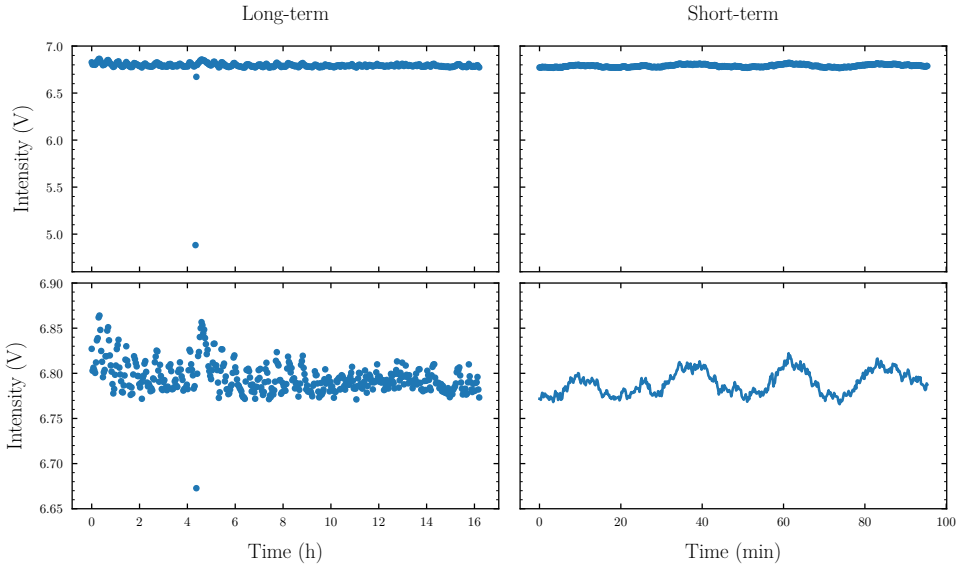

Figure 5.3.: Long- and short-term measurement of the controlled intensity at different voltage scales.

time scale compared to intensity variations in a typcial measurement. In order to compare the intensity deviations further we calculate the relative mean deviation (RMD) via

$$I_{\text{rmd}} = \frac{I - \overline{I}}{\overline{I}}, \tag{5.1}$$

where $\overline{I}$ denotes the intensity mean. In Figure 5.4 the RMD of the not-stabilized and the actively stabilized measurements are presented as boxplots. Boxplots are heavily based on the concept of interquartile range (IQR). The IQR is a scale invariant measure of statistical dispersion and is defined as the inverse of the cummulative distribution function (CDF). The start and end of the boxes inside a boxplot denote the lower (first) quantile Q_1 and the upper (third) quantile Q_3 of the IQR. Expressed through the CDF these read

$$Q_1 = \text{CDF}^{-1}\left(\frac{1}{4}\right) \qquad Q_3 = \text{CDF}^{-1}\left(\frac{3}{4}\right). \tag{5.2}$$

Alternatively one can define Q_1 as the median of the n smallest entries and Q_3 as the median of the n largest entries where the total dataset consists out of $2n$ entries for the even and $2n+1$ entries for the odd case. The whiskers below and atop of the boxes are at $Q_1 \pm 1.5\text{IQR}$. Values outside this range are usually considered outliers and marked as circles. The median is denoted with an orange line. The left boxplot confirms that the oscillations of the controlled intensity are negligible for typical intensity measurements. Further the right boxplot confirms that the intensity control oscillations cover a much smaller range as the uncontrolled oscillations.

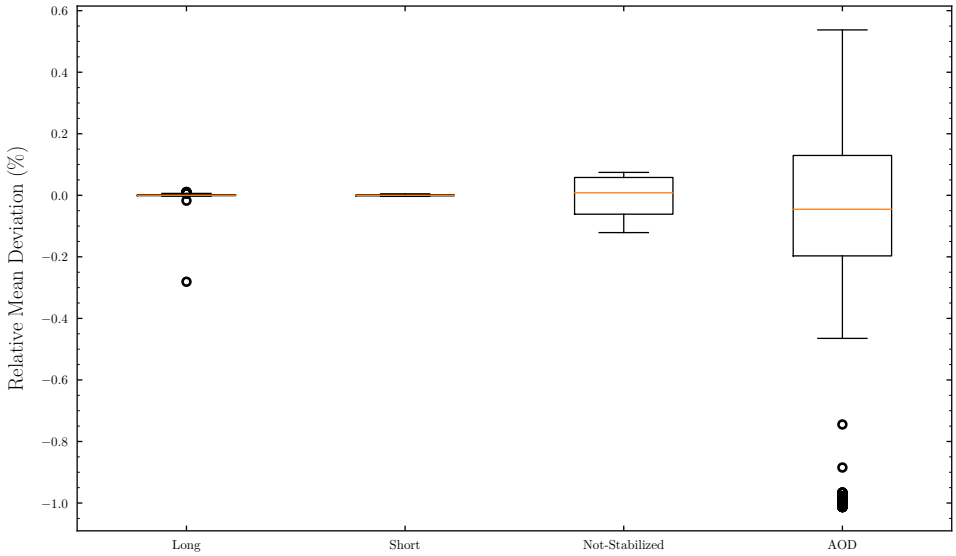

Figure 5.4.: RMD of not-stabilized and actively stabilized long- and short-term measurement as well an actively stabilized AOD intensity measurement.

5.2. Beam profile

Independently of the error introduced by the imperfect intensity control, errors can originate from unideal optical alignment. One way to assess the quality of our alignment is to evaluate the spatial profile of the laser beam as registered with the CCD camera. In Figure 5.5 we present

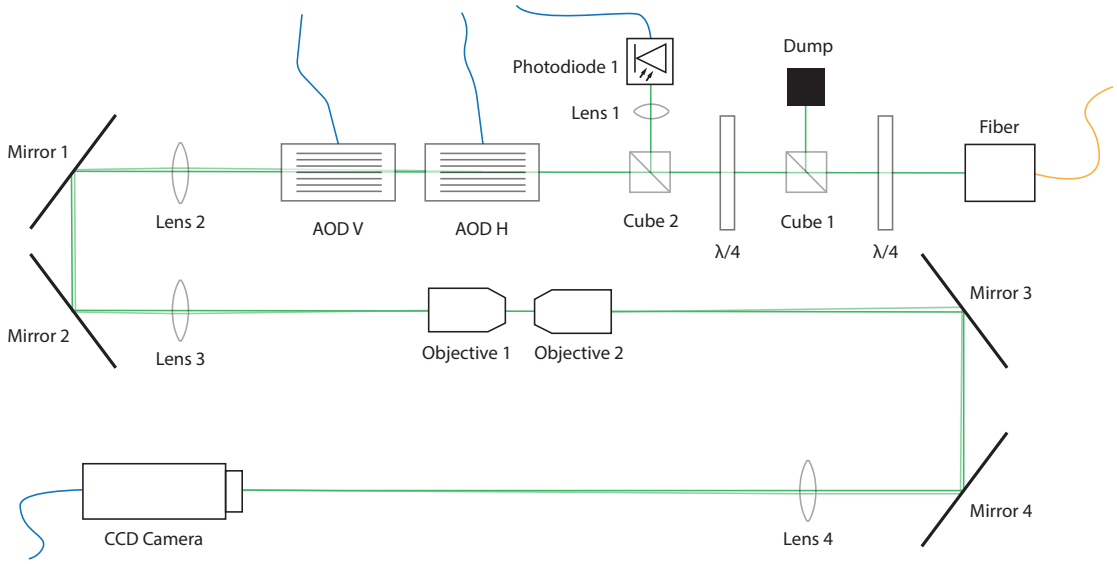

Figure 5.5.: The beam is focused onto the CCD sensor of the camera.

the setup used to measure the spatial beam profile. In comparison to the previous setup we replaced Photodiode 2 with a CCD camera. The AODs are configured at a center frequency of 100 MHz. The distance between Lens 4 and the CCD sensor is chosen such that the laser beam is focused onto the CCD sensor of the camera. Figure 5.6 shows an enlarged image patch of the complete image capture taken with the CCD camera. We can see a strong illuminated circular

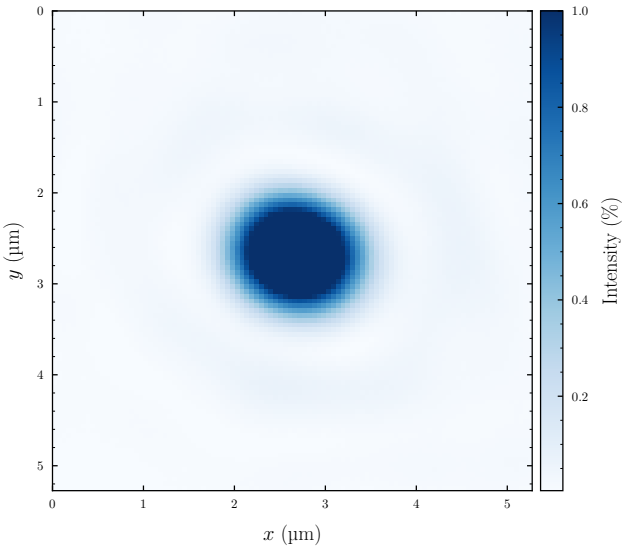

Figure 5.6.: Image of the focused laser beam measured with the CCD camera.

spot in the center of the image with an area of about 2.5 mm. The intensity inside the spot seems homogeneous, however this is caused by a saturation of the pixels in this area. We could reduce the intensity or apply an optical filter to the camera to resolve the intensity gradient inside the spot, but only at the cost of the intensity distribution around the spot. Around the circular spot we can see a diffraction ring. The diffraction ring is well described in [12] and originates from the finite aperture of the objectives. For better comparison of the radial symmetry we performed two

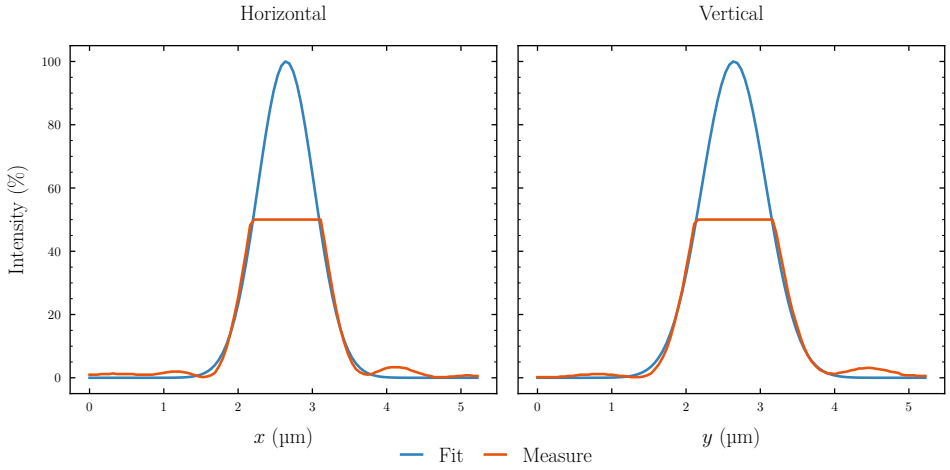

Figure 5.7.: One dimensional perpendicular cut of the two dimensional intensity distribution from the two dimensional beam profile in Figure 5.6 with fitted gaussian curve.

perpendicular cuts and visualized the one dimensional spatial beam distribution in Figure 5.7. In Figure 5.7 we can clearly observe the effects of saturation around the center. The Gaussian fit illustrated how we would expect the intensity to be if we could experimentally resolve it. In contrast to the ideal Gaussian profile we again observe contributions in the wings due to the Airy disc causes by the finite aperture of the objectives in the optical setup, see Figure 4.3. Further we can clearly observe an assymmetry in the intensity distributions in the wings which means that

our alignment is not perfect. Using

$$\mathrm{FWHM} = 2\sqrt{2\ln 2}\sigma, \tag{5.3}$$

we can find the from the Gaussian fit, being 0.89 µm for the horizontal and 1.02 µm for the vertical axis of the beam in the atomic plane.

We can confirm the results reported in [12] that the spatial beam profile equals a two dimensional Airy disk caused by the finite aperture of the objectives. Further we observe slight assymmetries in the diffraction ring suggesting inperfect alignment. Though asymetries in the spatial beam profile are present, we do not see any further complications as the intensity measurements with the photodiode will cover the complete beam profile.

Chapter 6.

Digital signal synthesis

The previous chapters have covered the physics of our application and we were able to recover some technical requirements imposed on our implementation. In this chapter we will review the fundamentals of digital signal synthesis, the theory on which the DDS — our RF signal source to control the AOD — are based on. DDS offer some distinct advantages over traditional analog synthesizer. For one they can cover a wide frequency range with high tuning resolution. In contrast analog devices have to be fitted to a narrow operation range and are subject to variations caused by aging, thermal drift and manufacturing. In addition DDS permit extremly fast, phase-continous frequency changes, without the loop-settling behaviour known to analog devices. Overall these advantages make the DDS an attractive solution for our application where it is used as RF signal source [26].

6.1. Operating principle

Figure 6.1 depicts a flow diagram of the components that make up a simple DDS. Given a system clock frequency f_{sys} and the desired output frequency f_{out} one can derive the phase accumulator increment

$$\Delta\varphi = \left\lceil \frac{f_{\mathrm{out}}}{f_{\mathrm{sys}}} 2^N \right\rceil , \tag{6.1}$$

where N denotes the number of bits the phase accumulator can store and $\lceil\cdot\rceil$ is the ceiling function. For every clock cycle the phase accumulator is incremented by $\Delta\varphi$. On overflow of the accumulator

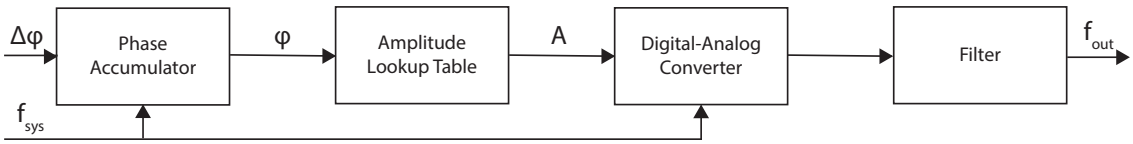

Figure 6.1.: Signal flow through a simple DDS. The output frequency determines a phase step $\Delta\varphi$ by which the accumulator is incremented at each clock cycle. The value of the phase accumulator is used for amplitude lookup of the desired output signal shape. A digital to analog converter (DAC) samples the output signal which then is filtered to smooth the discrete DAC output.

a new signal period starts. The phase accumulator value is used to lookup the corresponding amplitude value of the desired output signal shape. For example one can use a lookup table with

the values of a sinusoidal output signal. Alternatively one can omit the lookup table and output a sawtooth output signal by suppling the phase accumulator output directly to the DAC or a square wave signal output by suppling the most significant bit directly. Finally a DAC converts the digital amplitude value to an analog signal. An optional analog filter can be used to smooth the discrete output. Table 6.1 discloses system parameters used for our DDS model and the AD9910 we use

	Example	AD9910
Phase Accumulator Precision N	8 bit	32 bit
Digital-Analog-Converter Precision P	14 bit	8 bit
System Clock f_{sys}	1 GHz	1 GHz
Signal Frequency f_{out}	100 MHz	100 MHz

Table 6.1.: System parameters used for our simplified DDS model and used in the AD9910.

in our setup [27]. Except for the precision which in practice is not the same accross the phase accumulator, lookup table and DAC our model parameters are choosen to be similar to the ones used in the setup. In Figure 6.2 the signal of our model DDS at different processing stages with the model parameters from table 6.1 are illustrated. In the first column of Figure 6.2 we can see

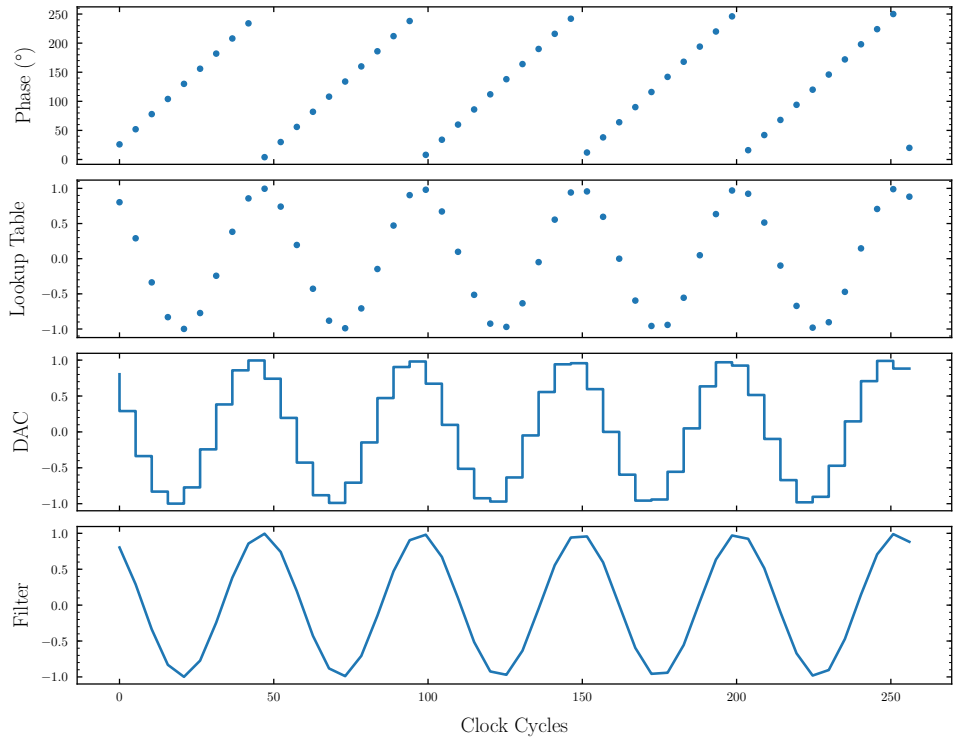

Figure 6.2.: Signal outputs at different stages in a simple DDS. The phase accumulator is incremented at each clock cycle by $\Delta\phi$. The phase accumulator value is used to lookup a sinusoidal amplitude value that is supplied to a DAC. The final result is smoothed using a filter.

how the phase accumulator is incremented on every clock iteration and resets on overflow. In the second column the lookup table has been used to return the corresponding cosine amplitude. We can see a difference in output shape between even and odd samples. This is caused by the fact that the phase increment is not a divisor of the phase accumulator size and we will later discuss workarounds.

6.1.1. Clock generation

The Nyquist-Shannon sampling theorem states that for a given sample rate a perfect reconstruction is guaranteed possible for $f_{\text{out}} < f_{\text{samp}}/2$. Until now we have considered the system clock frequency $f_{\text{sys}} = f_{\text{samp}}$ as given. In practice reliable reference signals are clocked below the desired output range and thereby cannot directly be used as system clock according to the Nyquist-Shannon sampling theorem. In Figure 6.3 the system clock generation from a reference signal is illustrated.

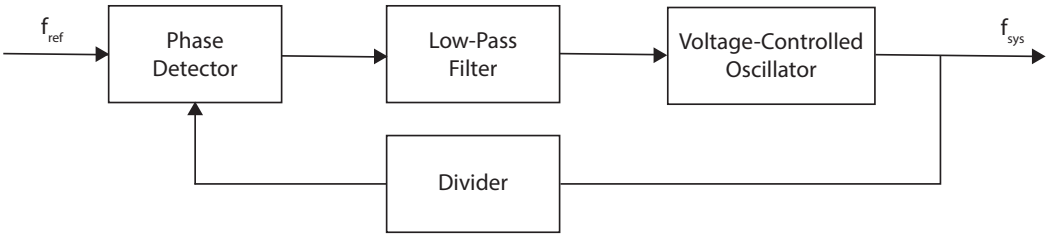

Figure 6.3.: Block diagram of the system clock generation from reference clock through phase-locked-loop (PLL) and divider.

The phase detector yields a non-linear error response comparing the phase of the voltage-controlled oscillator (VCO) with the phase of the reference signal. A low-pass filter removes fast oscillations from the phase detector output. The VCO changes its phase according to the error signal. One can use a system clock of a multiple frequency of the reference clock by using a frequency divider in between the phase detector and the output of the VCO. A divider of $M \in \mathbb{N}$ results in a system clock running at $f_{\text{sys}} = M f_{\text{ref}}$.

6.1.2. Parameter modulation

So far we only discussed the case of frequency modulation of the generated output signal, however, we will see that it can be easily extended to support amplitude and phase modulation too. In

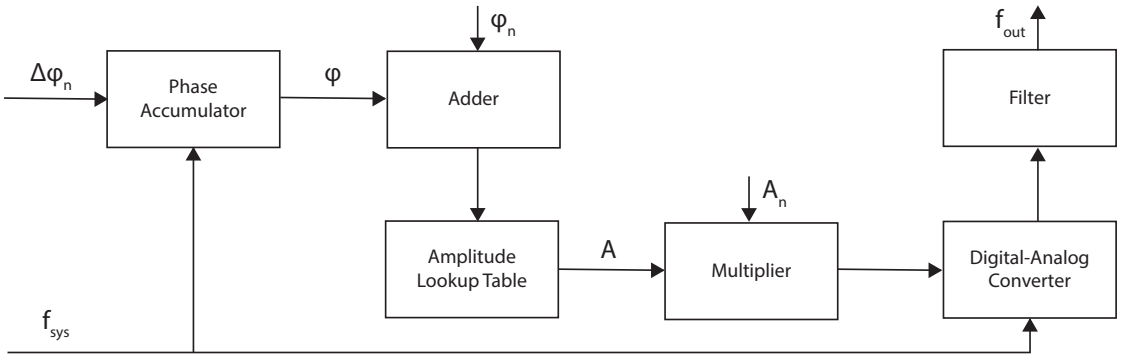

Figure 6.4.: DDS architecture supporting modulation of frequency, amplitude and phase offset parameters. Phase accumulator increment $\Delta\varphi_n(t)$ is now time dependent. The phase offset $\varphi_n(t)$ is also time dependent and is added as a last step to the phase accumulator before supplied to the DAC. The time dependent amplitude parameter $A_n(t)$ is multiplied with the amplitude obtained from the lookup table.

Figure 6.4 we can see one realization of an architecture that supports amplitude, frequency and

phase modulation. The main components are the same as in Figure 6.1. In addition we have an adder for a time dependent phase offset and a multiplier for the digital amplitude value obtained from the lookup table. The time dependence of the parameters can be either determined by reading from memory or through generation of another circuit. In a later section we will discuss the case of a linear frequency sweep provided by a digital ramp.

6.2. Quantization effects

At the beginning of this chapter we elaborated greatly on the advantages that digital signal synthesis has to offer. Yet we know that every technical design involves its unqiue set of compromises. One important part in any engineering process is to carefully evaluate the implications of these compromises. In that sense we will discuss the side-effects arising from the digital nature of digital signal synthesis and what methods exist to reduce them.

Phase jitter

Phase jitter is created when one configures an output frequency for which $\Delta\varphi$ is not a divider of 2^N. In this case a phase error builds up in each clock cycle [28]. According to

$$\frac{f_{\text{out}}}{f_{\text{sys}}} 2^N - \Delta\varphi, \tag{6.2}$$

with the phase accumulator increment $\Delta\varphi$ defined in eq. (6.1), we have a phase error of 0.4 per clock cycle for the model system parameters listed in Table 6.1. In Figure 6.5 the phase error

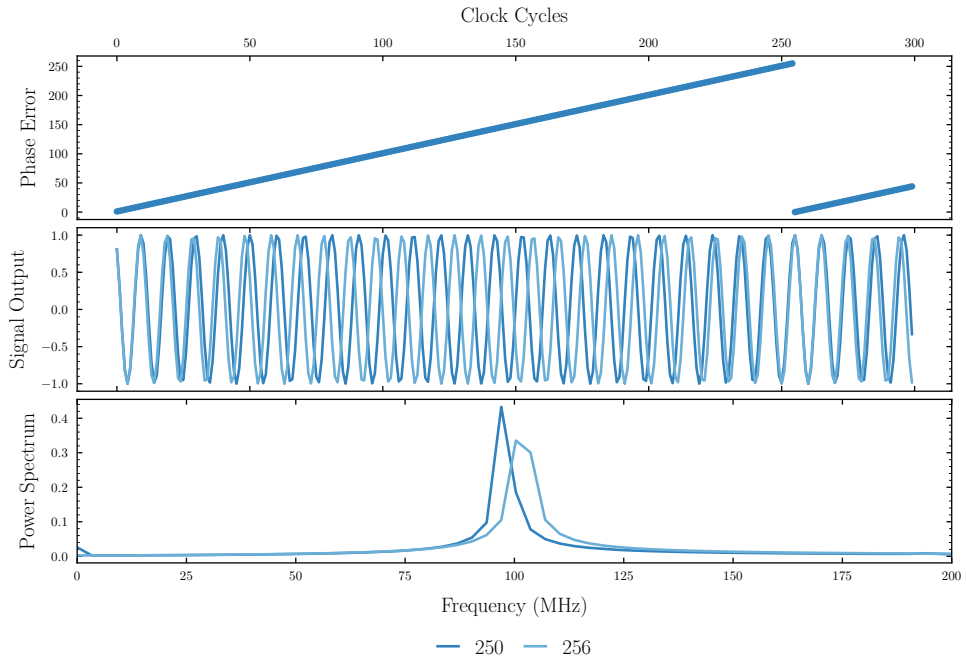

Figure 6.5.: Phase error for system model parameters in Table 6.1 when comparing phase accumulator with $2^N = 256$ and 250 values.

is visualized for a phase accumulator with $2^N = 256$ values and 250 values. The later phase

accumulator value yields zero for the phase error defined in eq. (6.2) and thereby represents the ideal signal. In the first row of Figure 6.5 we can see how the phase error builds up with every clock cycle. After 255 cycles the phase error resets. In the second row we can see how the output signal with phase error differs from the ideal output signal where no phase error is present. In the last row we see the power spectrum of the ideal and erroneous output signal. Because the instantaneous frequency relates to the change in phase of a periodic signal, we can see how the linear increasing phase error shifts the output frequency to the right.

Phase truncation

Phase truncation occurs because the amplitude lookup table and DAC usually have a reduced precision P compared to the phase accumulator. Fortunately there are many procedures to use the limited memory of a sinewave lookup table more efficiently. For example one can reduce the sinewave data to the domain from 0 to $\pi/4$ and use symmetry to infer the values from $\pi/4$ to 2π. Sophisticated compressions methods allow compression ratios up to 165:1 [29] so that in practice phase truncation is not a problem.

There of course exists other sources of signal imperfection, for instance because of PLL errors, not covered in this section from which many can be described analytically [30].

6.3. Frequency response

Beside the previously discussed signal shape deviations caused by finite precision, sampling theory predicts a sinc frequency response of the amplitude for the DAC [31]. Let us considers the discrete-time signal obtained from the amplitude lookup table of the DDS

$$x(t) = A(t) \sum_n \delta(t - nT) = \sum_n A(nT)\delta(t - nT) = \sum_n A_n \delta(t - nT), \tag{6.3}$$

where we define the delta distribution to be

$$\delta \colon \mathbb{R} \to \{0, \infty\} \tag{6.4}$$

$$t \mapsto \delta(t) := \begin{cases} \infty, & \text{if } t = 0 \\ 0, & \text{otherwise} \end{cases}, \tag{6.5}$$

and the sum is evaluated over the total number of samples and $T = 1/f_{\text{sys}}$ denotes the sampling period. Most DAC — including the DAC integrated into the AD9910 — perform signal reconstruction by zero-order hold. In zero-order hold a sample is hold for one sample interval, this can be expressed by

$$y(t) = \sum_n A_n \operatorname{rect}\left(\frac{t - Tn}{T}\right), \tag{6.6}$$

where the sum has to be taken over the number of sampled points, and

$$\operatorname{rect} \colon \mathbb{R} \to \{0, 1\} \tag{6.7}$$

$$t \mapsto \operatorname{rect}(t) := \begin{cases} 1, & \text{if } 0 \leq t < 1 \\ 0, & \text{otherwise} \end{cases}, \tag{6.8}$$

being the piecewise-constant output signal of the DAC. The DAC output can be modeleled through a linear transfer function h that relates to the input x and output signal y by convolution

$$y(t) = (x \circledast h)(t). \tag{6.9}$$

The sampled eq. (6.3) and the reconstructed signal eq. (6.6) in the frequency domain read

$$X(\omega) = \sum_n x_n e^{-i\omega nT} \tag{6.10}$$

$$Y(\omega) = \sum_n x_n e^{-i\omega nT} T e^{-i\omega T/2} \operatorname{sinc}\left(\frac{\omega T}{2}\right), \tag{6.11}$$

where we define the sinc function to be

$$\operatorname{sinc}\colon \mathbb{R} \to \mathbb{R} \tag{6.12}$$

$$x \mapsto \operatorname{sinc}(x) := \begin{cases} \frac{\sin(x)}{x}, & t \in \mathbb{R} \setminus \{0\} \\ 1, & t = 0 \end{cases}. \tag{6.13}$$

According to the Convolution theorem the convolution of two functions in the time domain equals the product of the two functions in the frequency domain, thus by using

$$Y(\omega) = X(\omega)H(\omega), \tag{6.14}$$

eq. (6.10) and eq. (6.11), we can easily read of the transfer function in the frequency domain

$$H(\omega) = T e^{-i\omega T/2} \operatorname{sinc}\left(\frac{\omega T}{2}\right). \tag{6.15}$$

As we are interested in the relative power of the DAC integrated into the DDS we need to look at the relative power transfer with respect to the output frequency f_{out}

$$\left|\frac{H\left(f_{\text{out}}\right)}{f_{\text{sys}}}\right|^2 = \operatorname{sinc}^2\left(\pi \frac{f_{\text{out}}}{f_{\text{sys}}}\right). \tag{6.16}$$

We visualized the frequency roll-off of the DAC in Figure 6.6 from zero to the Nyquist frequency $f_{\text{sys}}/2$. In the second plot we show the frequency range 80 MHz to 120 MHz which we will use as

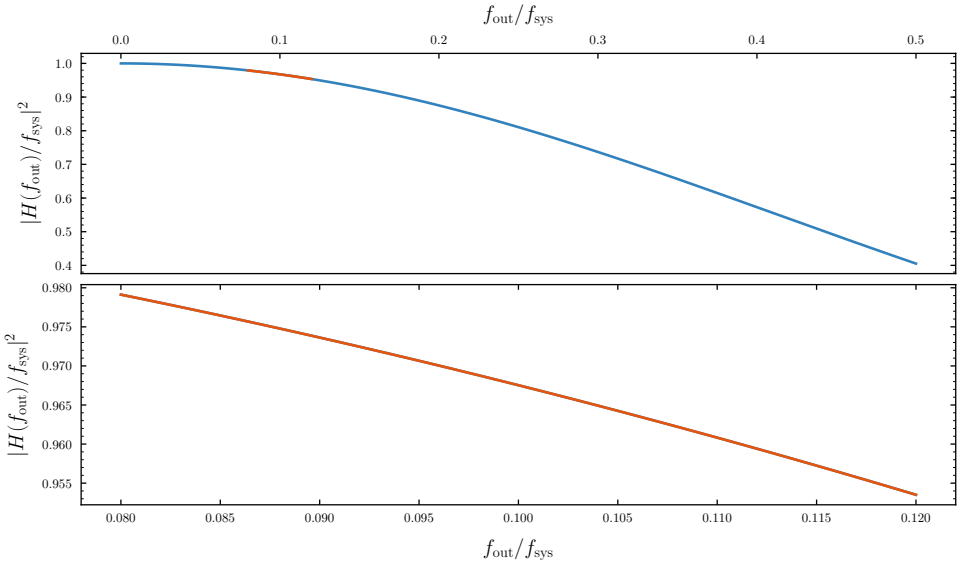

Figure 6.6.: Power transfer of the DAC according to the zero-order hold model with respect to relative output frequency from zero to the Nyquist frequency $f_{\text{sys}}/2$. In the second plot we see the power transfer for the later operating range of the DDS.

the operating range for our DDS. For said operating range the power falls off linearly by about 2.6 %.

6.4. Memory playback

In this and the next section we will discuss frequency and amplitude modulation by the digital ramp and memory playback integrated into the AD9910, therefore the following insights will be very specific to the AD9910. The digital ramp is used to implement sweep modulation with constant increments. In our case we will use the digital ramp to sweep the frequency applied to the AOD from 80 MHz to 120 MHz. The playback mode allows modulation from memory. We can use it to define up to 1024 distinct amplitude values in order to indirectly modulate the efficiency of the diffraction of the AOD. Both digital ramp and memory playback are controled by a timer that is clocked with

$$f_{\text{timer}} = f_{\text{sys}}/4 = 250\,\text{MHz}. \tag{6.17}$$

The sample interval of the memory playback is controlled by a 16 bit playback rate word

$$\Delta t_{\text{mem}} = \frac{P}{f_{\text{timer}}} = \frac{4P}{f_{\text{sys}}}. \tag{6.18}$$

In Figure 6.7 we illustrate the playback sample interval and total playback duration when using the complete playback memory in dependency of the playback rate word P. In Table 6.2 we

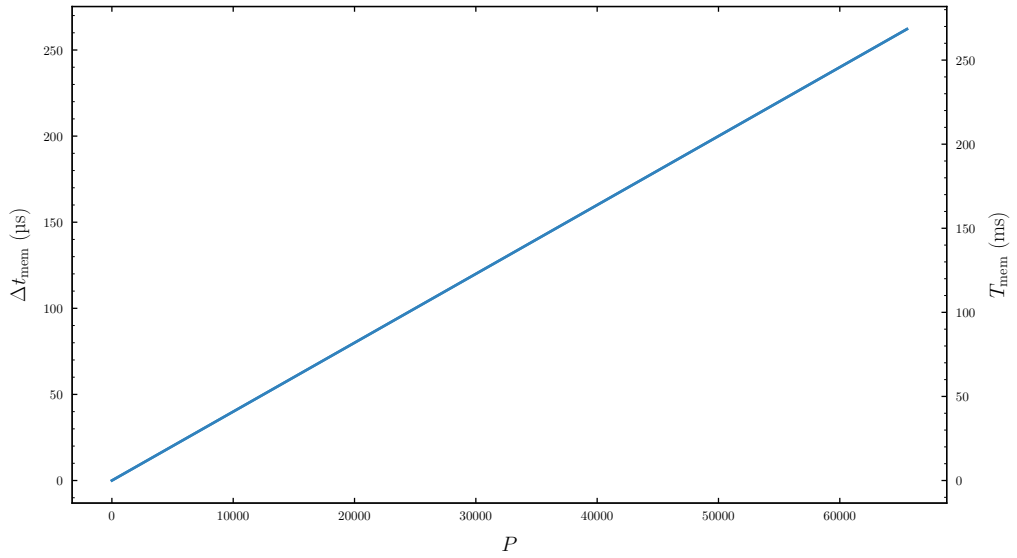

Figure 6.7.: Playback sample interval and total playback duration when using the complete 1024 memory points in dependency of the playback rate word P.

present the minimal and maximal playback parameters. The maximum duration of one iteration through all playback values T will limit the duration of the digital ramp as we will see later.

Rate Word P	Sample Interval Δt_{mem}	Duration T_{mem}
1	4 ns	4.096 µs
65 536	262.144 µs	268.435 456 ms

Table 6.2.: Minimal and maximal playback parameters of the AD9910 according to eq. (6.18) with $f_{\text{sys}} = 1\,\text{GHz}$.

6.5. Digital ramp

The digital ramp allows amplitude, frequency or phase offset modulation with constant increments. In our setup we use the digital ramp to sweep the frequency range 80 MHz to 120 MHz to change the beam deflection angle via AOD. In Table 6.3 the register of the digital ramp to perform frequency increments are listed. The lower and upper limits are related to the start and final

Lower Limit L	Upper Limit U	Step Size S	Step Rate R
32 bit	32 bit	32 bit	16 bit

Table 6.3.: Digital ramp register that control the frequency and their respective presicion.

frequency of a sweep by

$$L = \left\lfloor 2^{32} \frac{f_{\text{start}}}{f_{\text{sys}}} \right\rceil \qquad\qquad U = \left\lfloor 2^{32} \frac{f_{\text{final}}}{f_{\text{sys}}} \right\rceil, \tag{6.19}$$

where $\lfloor \cdot \rceil$ maps to the closest integer. In Table 6.4 we present the digital ramp limit register values for a frequency sweep from 80 MHz to 120 MHz as used for later measurements. The slope rate R

Register	Value	Quantity
Lower Limit L	343 597 384	80 MHz
Upper Limit U	515 396 076	120 MHz

Table 6.4.: Digital ramp limit registers for a frequency sweep from 80 MHz to 120 MHz.

and the step size S relate to the frequency and time increments via

$$\Delta t_{\text{ramp}} = \frac{R}{f_{\text{timer}}} = \frac{4R}{f_{\text{sys}}} \qquad\qquad \Delta f_{\text{ramp}} = \frac{S}{2^{32}} f_{\text{sys}}. \tag{6.20}$$

In the driver we set R and S indirectly through the sweep duration

$$T_{\text{ramp}} = \frac{U - L}{S} \frac{4R}{f_{\text{sys}}} \Delta t_{\text{ramp}}. \tag{6.21}$$

The integer ratio R/S is found using best-ratio approximation as described in Ref. [32]. In Table 6.5 the step register values of the digital ramp for the most common sweep duration of 260 ms used in our measurements are listed. The increments reported in Table 6.5 are converted internally in

Register	Value	Quantity
Step Size S	42 949 673	10 MHz
Step Rate R	16 250 112	65 ms

Table 6.5.: Digital ramp step registers for a frequency sweep from 80 MHz to 120 MHz with duration $T_{\text{ramp}} = 260$ ms.

the AD9910 and applied to the phase accumulator of the AD9910, thus even though the step size and rate are large compared to the sweep duration and frequency range, the effective frequency increments are of finer scale as we later measurements will show. Unfortunately the datasheet of the AD9910 [27] does not disclose any details on the exact conversion of the digital ramp steps to the phase accumulator, such that we cannot estimate the effective frequency resolution of the digital ramp of the AD9910.

6.6. Frequency and time resolution

Although we cannot give the exact frequency resolution imposed by the digital ramp of the AD9910, we can compare the possible time scales of the digital ramp and memory playback mode with the time scales found in chapter 3. Furthermore the specified frequency resolution of 230 mHz in the constant frequency operation mode of the DDS can give us a rough estimate of the achievable spatial resolution.

The time scale of the AD9910 are limited by the playback duration time

$$T_{\text{mem}} = N\frac{4P}{f_{\text{sys}}}, \tag{6.22}$$

where N is the number of memory words used. The AD9910 supports up to $N = 1024$ memory words. Using the fact that P is of 16 bit precision we can calculate the minimal and maximal durations times for the DDS. In Table 6.6 we are presented the possible time scales imposed by

Memory Words N	Playback Rate P	Maximum Duration T
1	1	4 ns
1024	1	4 µs
1	65 536	262 µs
1024	65 536	268 ms

Table 6.6.: Time scales of the AD9910 imposed by the technical limits of the playback duration time of the AD9910.

the playback duration time of the AD9910. From chapter 3 we know that we need to operate on a time scale of below 10 µs. We can see that for $P = 1$ and $N = 1024$ we could — in principle — achieve such duration times. If we use the memory playback to modulate the frequencies, we could address up to 1024 distinct positions on the lattice. The frequency resolution of the AD9910 is given with $\Delta f = 230$ mHz [27] which translates to a spatial resolution using eq. (4.2) of about

$$\Delta x \approx \Delta y \approx 8\,\text{pm}, \tag{6.23}$$

which is smaller than the actual laser wavelength. We therefore conclude that the frequency and time resolution of the DDS are in theory sufficient to implement the time-averaged perturbation potentials discussed in chapter 2.

Chapter 7.

Characterisation of the electronic setup

By the time the RF signal has reached the acoustic transducer, it has been synthesized from a reference signal, amplified, and matched to the impedance of the AOD transducer. We are going to inspect the RF signal characteristics at each transmission and find that each stage unintentionally carries out frequency dependent amplitude characteristics which, as we will see in the next chapter, are responsible for the complex intensity distribution observed with the photodiode.

7.1. Digital signal synthesizer

We already covered the fundamental functionality of the DDS in Chapter 6 and its integration in our experimental setup in Section 4.2.1. In this chapter we will discuss measurements of the frequency and the amplitude characteristics.

Physical analysis of the DDS output RF signal is in fact no simple endeavour as usual operation time scales are of many magnitudes greater than the signal periodicity. The procedure we used to resolve this circumstance is depcited in Figure 7.1. The strategy consists of capturing multiple,

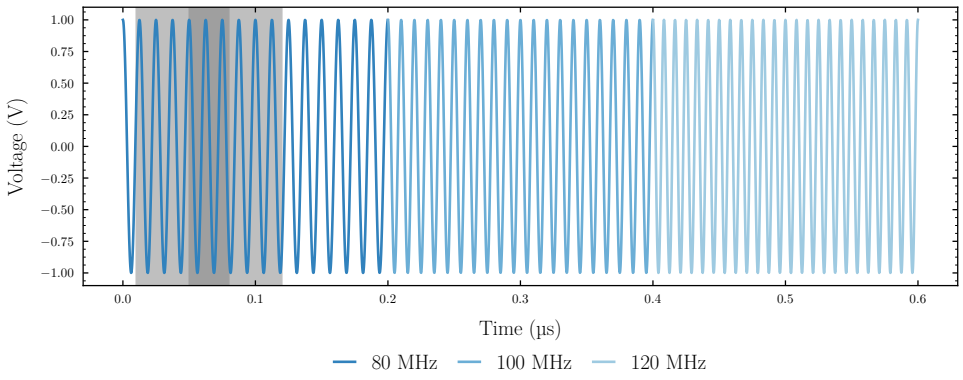

Figure 7.1.: Idealized DDS signal output with constant frequency increments. The measured window only captures a subset (gray) of the complete modulation (shades of blue).

small time windows of the signal (gray) which delayed would cover the complete signal trace (blue).

The experimental setup used to reailize this concept is schematically drawn in Figure 7.2. In

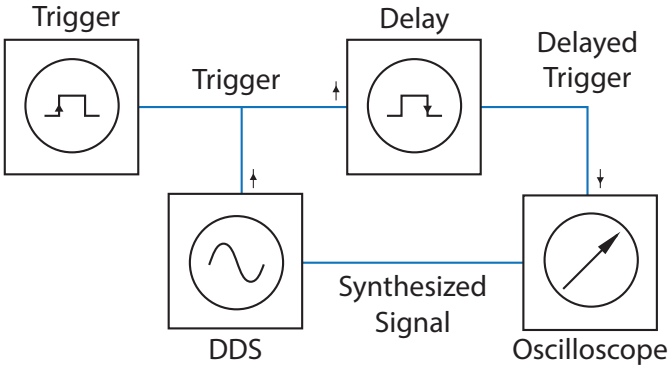

Figure 7.2.: Measurement setup of the synthesizer signal. By inserting a pulse generator in between the trigger source and the oscilloscope we can delay the capture window of the oscilloscope by the pulse width.

between the oscilloscope and the trigger source we inserted a pulse generator. The pulse generator width equals the delay time of the oscilloscope and the oscilloscope is configured to capture on the falling edge of the signal generated by the pulse generator. Further the oscilloscope's impedance was configured to 50 as high impedance measurements in the high frequency regime are subject to reflection and inductance effects. In Table 7.1 we can find an overview of the experimental parameters used. The specified frequency range is motivated to cover the greatest possible spatial

Frequency Range f	Sweep Duration T_s	Window Duration T_w	Number Windows N_w
80 MHz to 120 MHz	30 ms	50 µs	300

Table 7.1.: Experimental parameters used to inspect the output RF signal of the DDS.

dimensions permitted by the dimensions of the optics. According to eq. (4.2) this translates to a spatial resolution in the atomic plane of about 146 µm (typical atomic clouds are with 30 µm much smaller). Sweep and window duration were selected as a compromise between the oscilloscope being able to resolve the signal fine enough to perform fast-fourier-transform (FFT) and the sweep duration being comparable to later experiments. The time delay was incremented in N_w steps until $T_s = T_w$, thus we will capture N_w overlapping windows.

Frequency spectrum

For an ideal linear frequency sweep we would expect a continuous increase of the frequency with respect to time, yet we know that the DDS makes use of digital signal processing methods which suggests a discrete frequency spectrum. To help us expose the characteristics of the digital frequency sweep we will utilize a spectrogram. A spectrogram visualizes how the frequency spectrum varies in time. One way to obtain a spectrogram is to partition the data into overlapping time chunks while performing FFT which allows us to combine time and frequency domain specific characteristics. In our case we choose the relative spectral power to be encoded as color. Figure 7.3 depicts four spectrograms, each taken at a different time window during the frequency sweep. The first spectrogram captures the start of the frequency sweep as can be read from the time scale. The first time window does not disclose any signal. This phenomena will be observed frequently. For unknown reasons the output signal of the DDS is absent for multiple microseconds after the DDS receives the external trigger signal. The exact duration of the trigger delay varies around

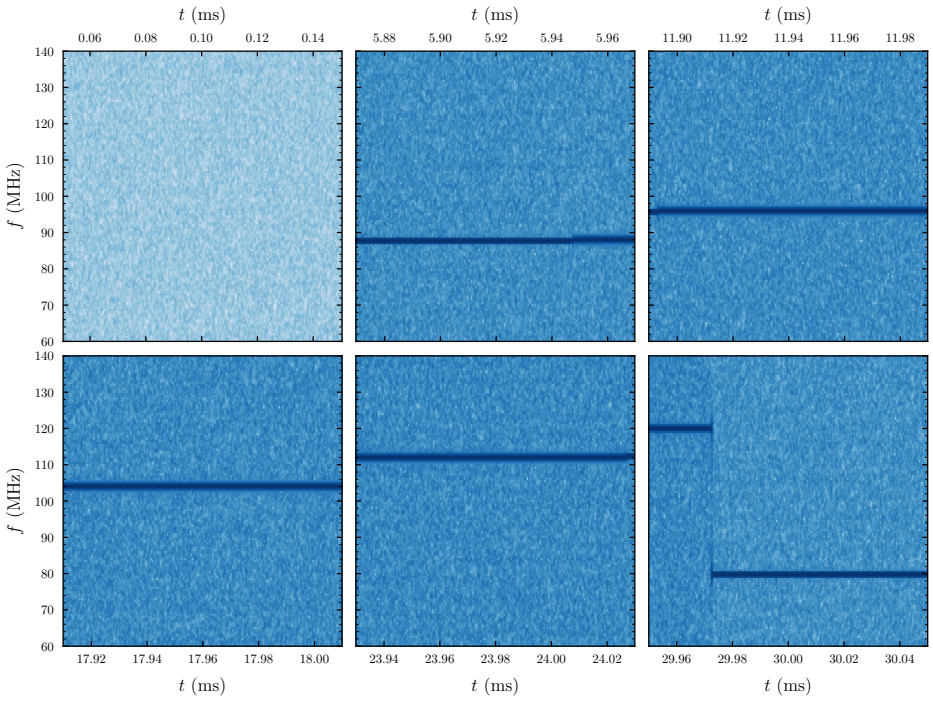

Figure 7.3.: Spectrogram of delayed time windows with width 100 µs of the DDS output signal configured to perform a linear frequency sweep. For an ideal linear sweep we would expect a linear timeline of the frequency, instead we observe a discrete set of frequencies.

4 ms but does not affect the internal state of the DDS as the first measured frequency matches the theoretically expected frequency according to the ramp. If we take a look at the following spectrogram windows we can see how the DDS outputs a constant frequency over a short time period (100 µs), therefore the frequency range consists of discrete frequencies. We can actually even observe such a frequency increment in the second, third and fifth spectrogram. Finally in the last spectrogram the frequency drops back to the initial value — a side effect of the DDS sweep mode which unfortunately is the only mode, that supports an external trigger signal. In Chapter 6 we were unable to make a statement about the frequency resolution of the digital ramp. Therefore we visualized the frequency evolution with each delayed measurement in Figure 7.4. Neglecting the first 50 measurements because of the trigger hole, we find that on average the frequency increments by about 310 kHz. Using eq. (4.2) this relates to a spatial resolution of about 1.1 µm.

Amplitude frequency response

In the Fourier space we can locate the dominant frequency at the maximum of the power spectrum. That in mind we can reduce the previous obtained time window measurements to pairs of dominant frequencies and maximum amplitude. Under the assumption that the maximum voltage per measurement is approximately the mean peak-to-peak amplitude of the signal we can find the amplitude frequency response spectrum with little effort. Figure 7.5 visualizes the described routine for the DDS assigned to the H and V AOD with frequency control by digital ramp and manual increments. The peak-to-peak amplitude of the synthesizser signal is constant with small noise contributions. On a closer view we can see that the oscilloscopes voltage resolution is at its limit, thus we only observe discrete voltage steps. We conclude from Figure 7.5 that the

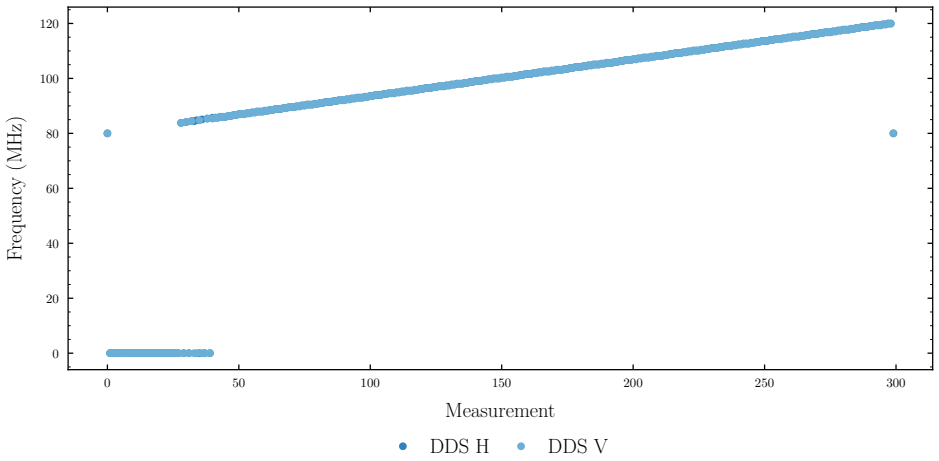

Figure 7.4.: Most dominant frequency in the FFT spectrum for each (delayed) measurement during a frequency sweep of the DDS.

amplitude response of the DDS is independent of the output frequency and the method used to provide frequency increments. The sinc response we theorized to cause a drop of about 2 % of the amplitude in Chapter 6 is not observable in our measurements.

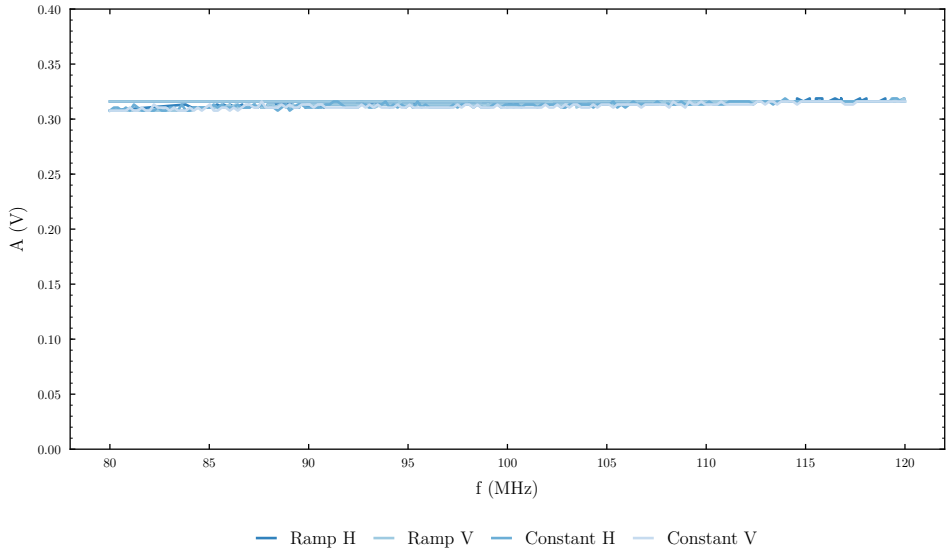

Figure 7.5.: Amplitude frequency response of the DDS signal sources for the H and V AOD. The frequency increments are performed through the integrated digital ramp and manually.

7.2. Power amplifier

The piezoelectric attached to the acousto-optic crystal inside the AOD elements has to emit acoustic waves strong enough to propagate through the crystal of the AOD. The power demands specified by the AOD are not met by the DDS, therefore we have to employ a power amplifier between the DDS and the AOD. Even though we previously concluded that the DDS signal amplitude is independent of the output frequency, the power amplifier can introduce new frequency dependent characteristics which we dedicate ourselves to in this section.

Amplitude frequency response

The measurement procedure described in the previous section is still valid for the now amplified signal of strength 33 dBm. At the usual 50 in between coaxial cables this corresponds to an approximate voltage of 10 V. In order to protect the oscilloscope against potential damage caused by too much power, we inserted a chain of attentuators (order given from coaxial cable to oscilloscope): 1 dB – 3 dB – 3 dB – 6 dB – 10 dB – 10 dB. The order was chosen in such a way to distribute heat uniformly accross the attentuators. The total damping of this configuration yields 33 dB which should give us the same signal power as before from the DDS. Figure 7.6 presents the damped output signal after amplification for the two distinct (H, V) amplifiers and DDS signals for the same input frequencies as in the previous measurement. In comparison to the DDS response the amplifier introduces small ripple. Again, we cannot identify significant differences between the type of frequency increment used. Although these effects are small in terms of voltage it is difficult to relate them to the overall power response as only voltage but not current was measured.

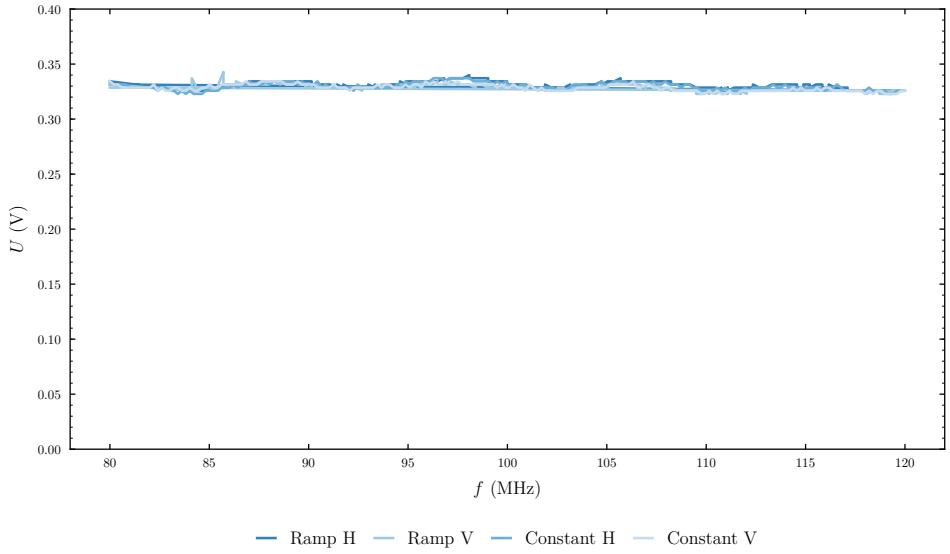

Figure 7.6.: Amplitude frequency response of the DDS signal after power amplification. In comparison to the DDS we observe very small oscillations.

Network analyzer transmission

We previously discovered that the amplifier amends the frequency amplitude response, nevertheless it is difficult to isolate the actual influence of the amplifier. Therefore we conducted more detailed measurements of the amplifiers power transmission with the network analyzer. The network analyzer is a device that can measure reflection and transmission parameters of electric components. As it was exactly built for these types of measurements, we expect it to have more significance, then the previous measurement. As in the measurement with the oscilloscope we also haveto protect the network analyzer against the output power of the amplifier. This time we used a single 30 dB attentuator in between the network analyzer input and the power amplifier output. In Figure 7.7 we see the frequency transmission spectrum obtained through the network analyzer connected to the horizontal and vertical amplifiers. We can confirm an offset of the amplification gain between both amplifiers. If we assume a power amplification difference of $L = 0.2\,\mathrm{dB}$, i.e. between 80 MHz and 115 MHz with the V amplifier, according to

$$P = P_0 10^{L/10\,\mathrm{dB}}, \tag{7.1}$$

and $P_0 = 2\,\mathrm{W}$ we would have to expect a drop of up to 0.05 W in power. Unfortunately we cannot say in how far this is a relevant magnitude for the AOD.

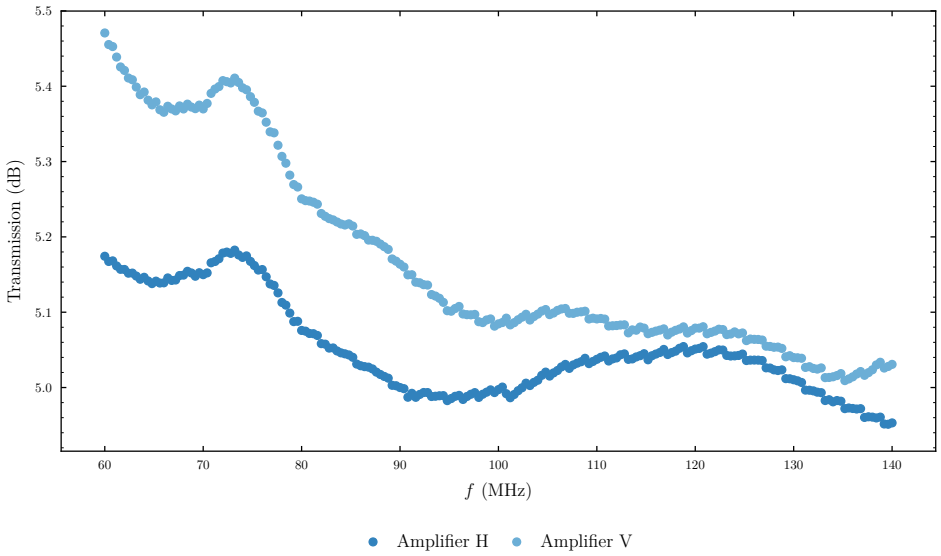

Figure 7.7.: Frequency transmission spectrum obtained via the network analyzer of the horziontal and vertical amplifiers.

7.3. Acoustic transducer

In the previous sections we explored the signal transfer of the synthesis and amplification stage. The last stage that is accessable to us concerns the power reflection at the AOD itself. From the reflection we may estimate power transmission characteristics, hence for a large reflection we would expect a small transmission and in that sense less beam intensity in the first diffraction order.

7.3.1. Reflection spectrum

The power reflection measurements were conducted with the network analyzer which we have introduced in the previous section. In a first embodiment of the experiment we directly supplied the AOD through a coaxial cable of the network analyzer with power and measured the reflection. In a second embodiment we used a directional coupler to supply the respective amplifier with a signal and measure the reflection through a directional coupler.

Direct connection

Figure 7.8 visualizes the power reflection spectrum of both AOD elements when directly connected to the network analyzer at a maximum output power of 10 dB m. The network analyzer port supplies the signal and measures its reflection. The most interesting finding in Figure 7.8 is that the power reflection shows very different behaviour for the distinct AOD elements. The AOD anticipated for the vertical deflection is most transmissive at 97 MHz with transmission falling of on both sides while the AOD anticipated for the horizontal deflection has two local transmission maxima and a rather bad transmision near the center frequency.

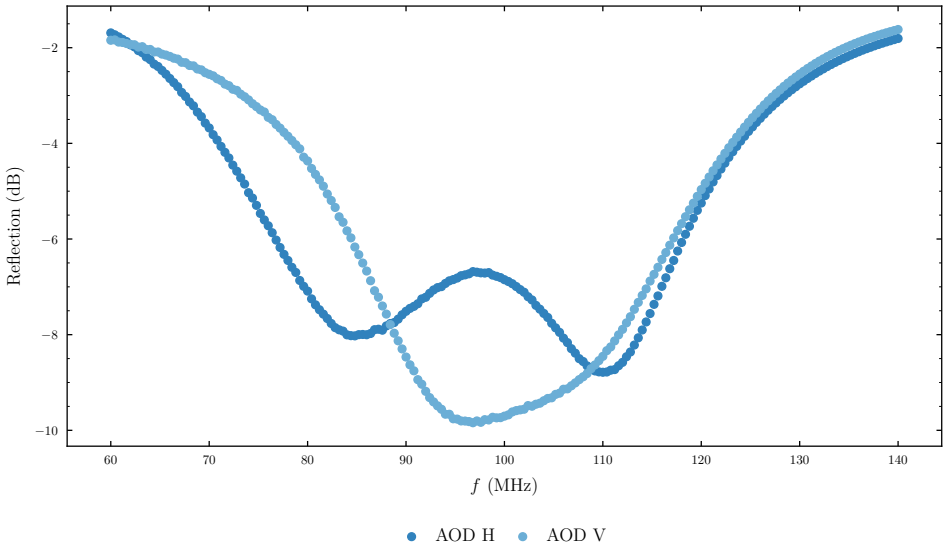

Figure 7.8.: Signal reflection of the two different AOD when directly connected to the network analyzer.

Amplified coupled connection

In the second procedure we amplify the signal and couple the network analyzer through a directional coupler to measure the refleciton. This is done in order to avoid harm to the network analyzer as the network analyzer is not able to handle 2 W signals. The direct-coupler is an apparatus comprising a coaxial input and output port as well as a coaxial input reflection and output reflection port. It is disignated to measure the reflection of a (possible) high power signal without jeopardizing measurement equipement. In Figure 7.11 we see the reflection spectrum for the case that we provide the network analyzer output signal to the input of the directional coupler and connect the reflection output of the directional coupler with the second network analyzer port while the remaining ports are under 50 closure. We note that the reflection measured through the directional coupler is lowered by many orders of magnitude compared to the input signal but essentially of the same shape. The noise in the reflection is very high because of the low power supplied into the directional coupler. We now use the directional coupler to measure the output reflection at the AOD elements after the signal was amplified. The setup is depicted in Figure 7.10. The network analyzer on the left-hand side supplies an input signal to the amplifier. The input signal changes linear in frequency. The output signal of the amplifier is connected through a directional coupler with the acousto-optic element. The directional coupler allows to measure input and output reflection. In Figure 7.9 we see the effective reflection spectrum for the distinct AOD elements. The effective reflection spectrum is obtained when subtracting the input reflection from the output reflection.

Comparison

In the previous part we saw that the reflection spectrum does not show any power dependence, thus we should be able to compare the spectrum we obtained directly with the amplified result. In Figure 7.12 we can see how there is additional reflection from the amplifier, nevertheless the global characteristics remain the same.

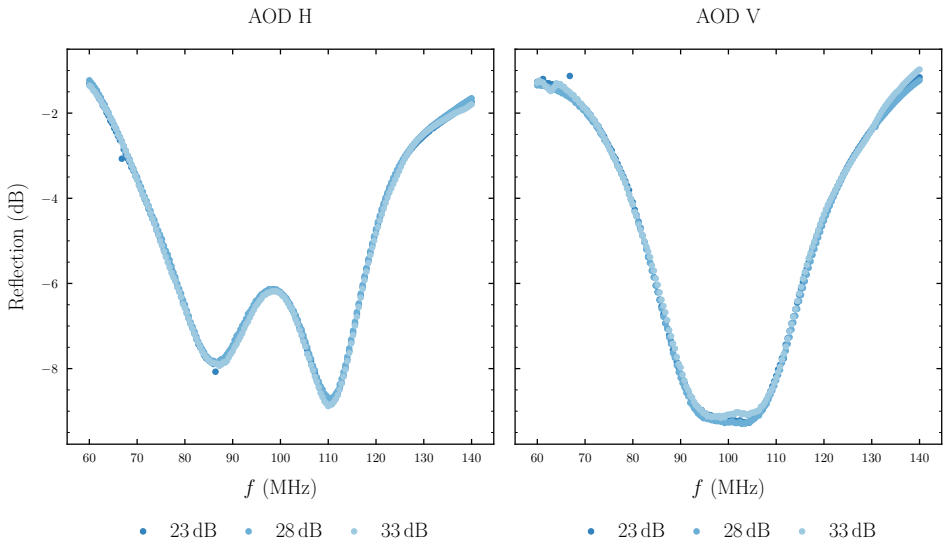

Figure 7.9.: Reflection at the direct-coupler output after amplification of the network analyzer input signal for different amplifications with reference to 1 mW. We see that the applied power does not affect the spectrum.

Summary

Distinct AOD elements show different power transmission characteristics independent of the applied power. A detailed examination of the AOD elements discloses different impedance matching circuits. Impedance matching is used to reduce power reflection by providing a constant input resistance of 50 accross a wide frequency range. Still the impedance differs between the AODs. We assume that the crystal properties, i.e. cutting angle or purity, are responsible for that. This is supported by the fact that the impedance matching circuits differ between the AOD elements.

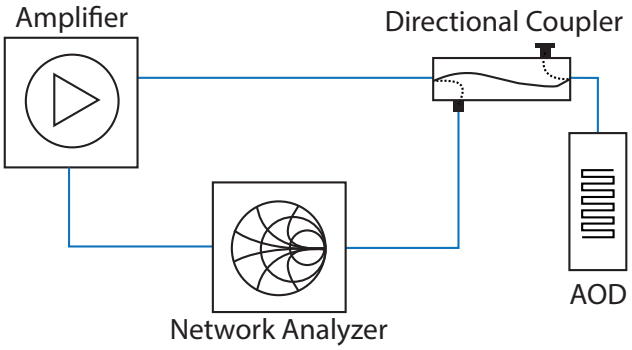

Figure 7.10.: Experimental setup to measure the reflection at the acousto-optic transducer. The network analyzer supplies an input signal to the amplifier. The output signal of the amplifier is connected through a directional coupler with the acousto-optic element. The directional coupler allows to safely measure input and output reflection.

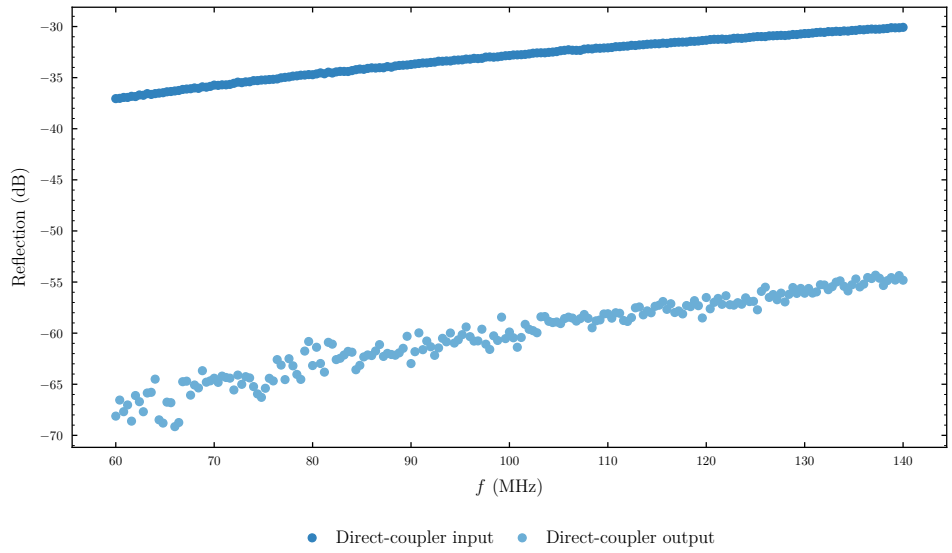

Figure 7.11.: Input power reflection when supplying the directional coupler with −10 dB m input signal and reflection at the closed output of the directional coupler while other ports are closed with 50 .

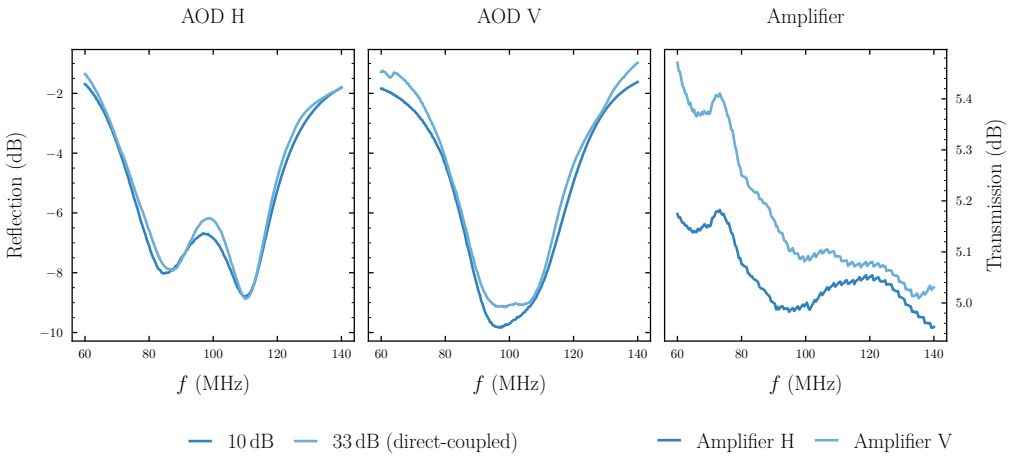

Figure 7.12.: Reflection from amplified input signal and direct signal as well as transmission spectrum from the amplifier. We can see that the better amplification left of 90 MHz slightly changes the reflection spectrum of the AOD.

Chapter 8.

Characterisation of the acousto-optic deflectors

In the previous chapter we seeked for different aspects of the RF signal powering the AOD elements and found that the electronic equipement provides an overall stable signal for the AOD. In this chapter we want to explore the diffraction efficiency characteristics of the AODs subject to the different frequency and amplitude parameters one can configure the DDS with. In the end we will find that the intensity shows highly non-linear behaviour with respect to the RF signal parameters.

8.1. Difference between individual acousto-optic deflectors

Our optical setup uses a single two dimensional AOD that comprises two AOD elements perpendicular to each other. At first we want to examine the behaviour of the individual AOD elements in comparison to each other. In particular we are interested if and how the elements differ.

8.1.1. Individual acousto-optic deflectors

For the following experiment we will only leave one AOD element mounted in the casing depicted in Figure 4.1. The other slot will be empty. Then we will exchange socket positions for each respective AOD element and measure the beam intensity subject to the linear frequency sweep from 80 MHz to 120 MHz over a duration of 260 ms and the configured DDS amplitude. As RF signal source the amplifier and DDS combination intended for the horizontal AOD element was used to avoid influences of the amplification offset between the two amplifiers. The results for the four configurations (horizontal element in horizontal slot, horizontal element in vertical slot, vertical element in horizontal slot and vertical element in vertical slot) are visualized as heatmaps in Figure 8.1. The color values are normalized in between the different heatmaps and can be related to the measured voltage from the photodiode via the colorbar on the right-hand side. Oddly enough we observe that both AODs differ strongly in their respective intensity transmission behaviour depending on their slot position. Furthermore we observe that the intensity transmission is much higher in the case of the horizontal AOD element mounted to the intended horizontal slot compared to all other configurations. In addition we can see that the intensity map measured with the horizontal AOD displays a jump. The highest intensity transmission is obtained for relative amplitudes configured between 60 % and 90 % with large dependence on the frequency. Another interesting observation is that the intensity transmission seems very similar for the horizontal

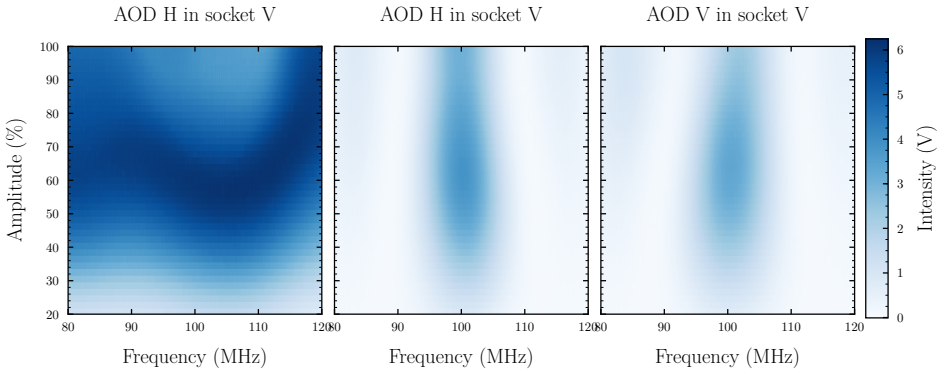

Figure 8.1.: Intensity distribution over linear frequency sweep at different configured DDS amplitudes for different individual AOD configurations.

element in the vertical slot and the vertical element in the vertical slot whose map also seems more symmetric with respect to the frequency axis. In fact for these configurations the amplitude dependence seems to be essentially independent of the frequency dependence. We assume that the individual elements are designed for different polarisation angles. In order to prove this hypothesis we added a tunable $\lambda/2$ retarder plate after Cube 2. Tuning the $\lambda/2$ retarder before Cube 2 would change the intensity fraction that gets redirected into the beam dump as Cube 2 is a beam splitter sensible to polarisation. In Figure 8.2 the intensity transmission of the H AOD in the H slot at

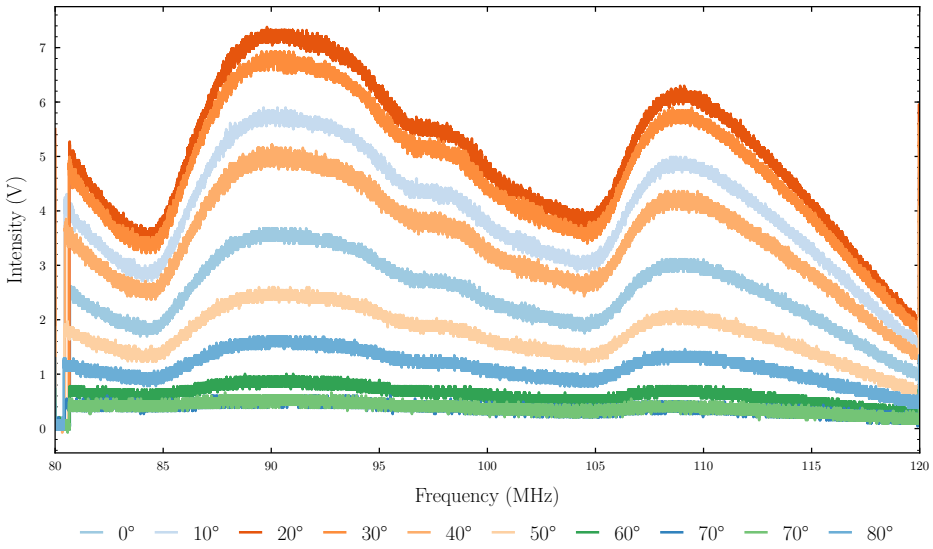

Figure 8.2.: Intensity transmission of the H AOD in the H slot at maximum output amplitude for different angles of the $\lambda/2$ plate.

maximum RF amplitude is presented for different polarisation angles. The polarisation angles are the remainder left after division by 90° of the angles read of from the retarder plate mount. The reason behind this step is that a rotation of a retarder plate by ϕ effectively changes the polarisation angle by 2ϕ. Further the polarisation angles are uniquely contained in the range $[0°, 180°[$. We note the maximum intensity transmission of the H AOD at 20° and the minimum intensity transmission at around 70°. The difference between the polarisation angle at minimum and maximum intensity is about 50° which is close to 45° that would suggest that intensity minimum and maximum are located at the respective perpendicular polarisation axis. In Figure 8.3 the intensity transmission

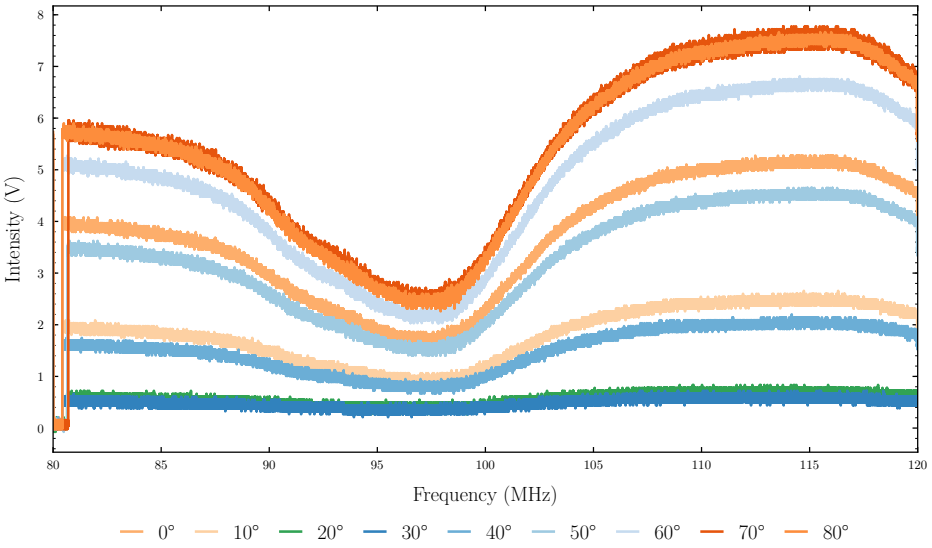

Figure 8.3.: Intensity transmission of the V AOD in the V slot at maximum output amplitude for different angles of the $\lambda/2$ plate.

subject to the polarisation angle of the V AOD in the V slot is shown. We again observe a difference of about 45° between the polarisation angles at maximum and minimum intensity transmission. Finally we want to compare the polarisation angles between the individual AODs. Therefore we extracted the intensity transmission at 100 MHz frequency for both AOD measurements and plotted them against the polarisation angle in Figure 8.4. We observe a sinusoidal shaped intensity response as a function of the angle for the H and V AOD which seem to be out of phase by nearly 90°. This, however, makes sense as the polarisation in the first diffraction order is rotated by 90°.

The 2D AOD casing allows to rotate the individual AOD elements. So far we choose the rotation angle of the AOD elements that maximizes the intensity transmission at the center frequency. What would we obtain if we tilted the rotation angle a bit to the left and to the right? In Figure 8.5 we find the answer to this question. We observe changes in shape and overall intensity with respect to the incident angle. We should note that small changes in the incident angle cause already large deflections of the beam, thus it is not guaranteed that the left and right measurements are free from aperture effects. Nevertheless we can record that the incident beam angle is an important parameter in the intensity transmission of the AODs. In particular we need to consider the incident beam angle for the 2D AOD configuration.

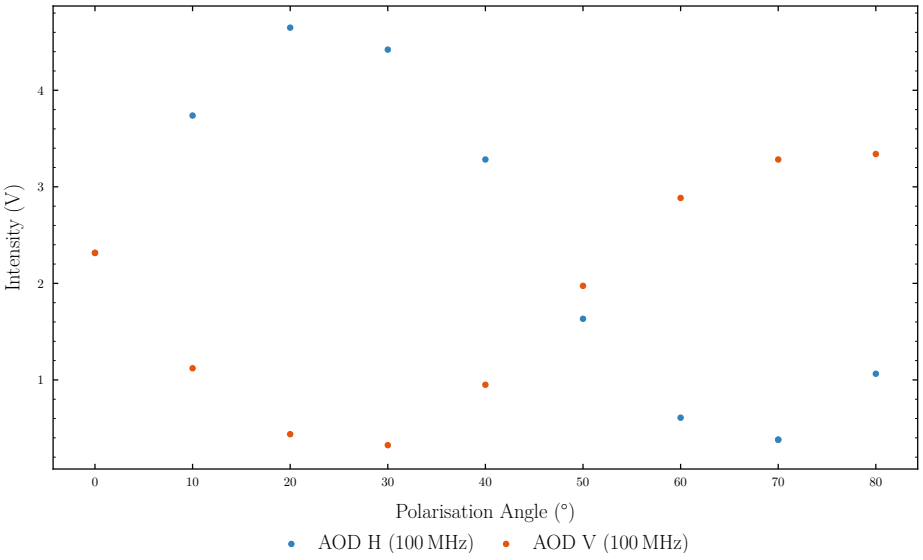

Figure 8.4.: Intensity transmission of the H and V AOD at 100 MHz and maximum output amplitude for different polarisation angles.

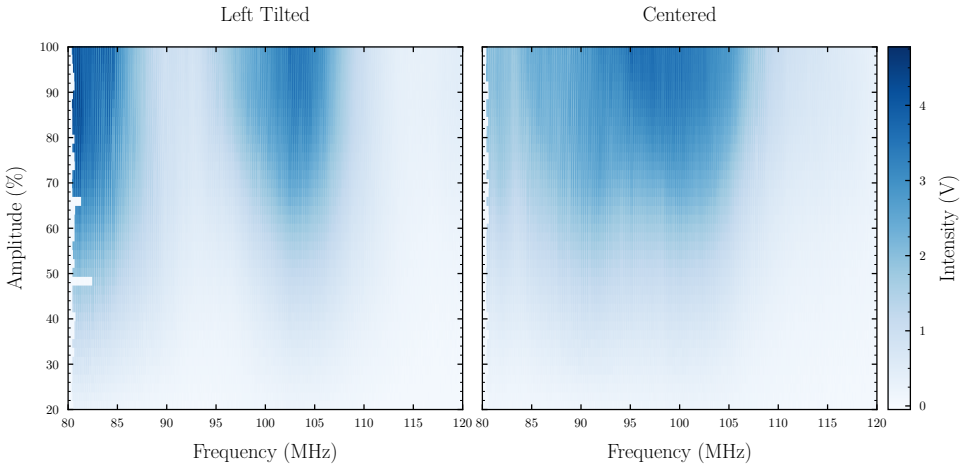

Figure 8.5.: Intensity distribution at different amplitudes for tilted individual AODs. We observe that the intensity decreases if the incident angle deviates from 90°.

8.2. 2D intensity distribution

In the present section we now want to explore the intensity transmission for a two dimensional sweep as intended to be used for the optical potentials.

The experimental setup is similar to the previous setups and is shown in Figure 8.6. We have both AODs mounted in their anticipated position. The AOD elements are aligned to maximize intensity at the center frequency. The laser beam is directed into Photodiode 2 where we measure the intensity with respect to the configured DDS signal.

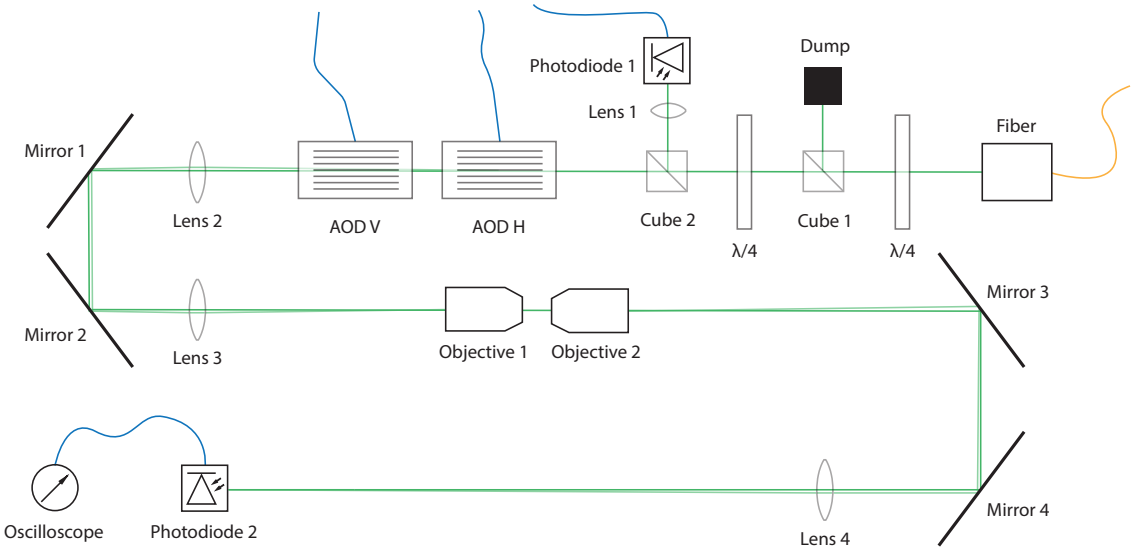

Figure 8.6.: Experimental setup used to measure the intensity transmission of the 2D AOD in dependence of the configured DDS signal.

Digital ramp frequency sweep

In a first attempt we configure a first DDS to output a constant frequency whereas a second DDS is configured to do a frequency sweep using the internal digital ramp. After one such sweep the constant frequency output of the first DDS is increased and the measurement repeats. The procedure is repeated until the first DDS covered the same frequency range as the second DDS. In Figure 8.7 we present the intensity measured at the second photodiode in the setup shown in Figure 8.6. On the left-hand map the first DDS is the DDS responsible for translations in the vertical direction whereas the second DDS is responsible for translations in horizontal direction. The frequency sweep performed by the digital ramp is more dense compared to the frequency sweep performed through the driver. We of course could also perform increments through the driver with the same precision as the digital ramp, this, however, would make measurements much more time consuming. As the differences in Figure 8.7 are of only subtile nature we additionally reveal the absolute difference between both maps in Figure 8.8. We observe nearly a binary map of dark and bright blue areas whereas the dark area can be intepreted as small and the bright area as large difference. The binary nature of the absolute difference could be interpreted as a fixed offset in the power level between the H and V RF signal supplied to the AODs. In areas of small intensity difference (dark blue) the ouptut level may be sufficient to saturate the acousto-optics. However we must admit that these are simply suggestions and need further evidence.

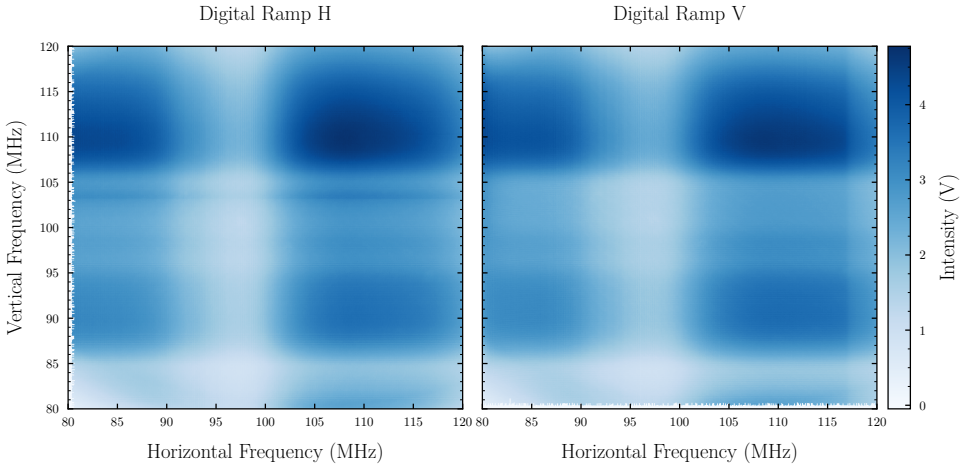

Figure 8.7.: Intensity measured as voltage at the photodiode in dependence of the horizontal and vertical applied frequency signal to the AOD. The left map is obtained by enabling the digital ramp on the horizontal DDS whereas the vertical DDS is configured to output a constant frequency which is manually increased after each measurement. On the right-hand side map the roles are exchanged.

Constant sampled frequencies

In section 7.2 we did not find differences in the amplitude frequency response of the amplified RF signal between frequency increments performed by the internal digital ramp of the DDS and frequency increments performed by manually updating the output frequency through the driver. Yet, it remains open if differences arise in the transmission frequency response of the AOD as the AOD is not a purely electronic device. To partly answer this question we sampled random frequency pairs over a two dimensional uniform distribution and passed them as constant frequency parameter to the respective DDS through the driver interface. The yielded intensity distribution is visualized in Figure 8.9. We note that in comparison to Figure 8.7 the intensity differences are more concentrated around the vertical axis. We believe that acousto-optics possess a non-instantaneous frequency response characteristic that requires further investigation.

Different radio frequency signal source

In the previous two sections we found that the AODs are independent of the method used to perform the frequency increments. In order to further gather further proof, we decided to replace one DDS with a high-quality signal generator while the other DDS was configured to output a constant 100 MHz signal. The output level of the signal generator was configured to match the output level of the DDS and amplified using the usual power amplifier. Figure 8.10 discloses the different intensity transmission registered by the photodiode for a frequency sweep performed by the DDS through the digital ramp and by the signal generator. In comparison to the DDS the signal generator does not support continous frequency changes as we can see from the intensity drops between the frequency increments of the signal generator trace. Further ignoring these intensity drops we observe that the global response characteristics differ in particular at the begin of the frequency sweep and at the center. As the power amplifier remains unchanged through the measurements and the output voltage of the signal sources are independent of frequency, we are only left with two explainations. For one the power supplied to the AOD could differ as we did not measure the current response. On the other hand the frequency drops in between frequency

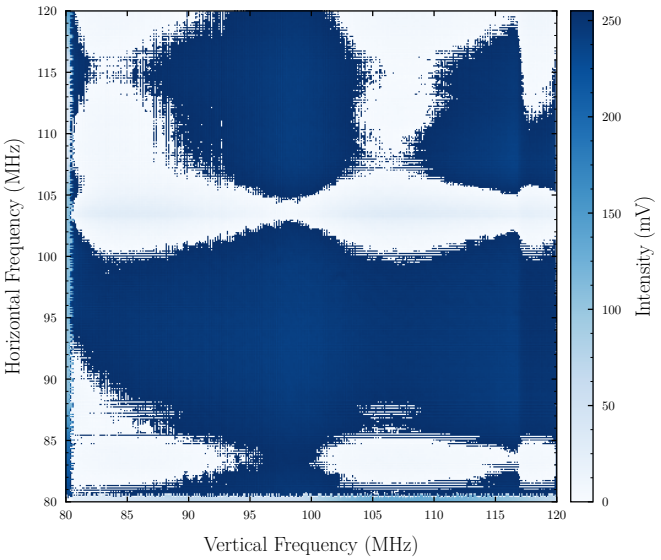

Figure 8.8.: Absolute difference between the 2D intensity distribution performed with the digital ramp configured set to different axes.

increments of the signal generator could cause the observed characteristis. The later hyphothesis would also confirm the result of the previous sections in which we found a different transmission characteristic for different frequency sampling strategies.

Summary

In summary we found that the intensity transmission of the AODs show a highly non-linear dependence in the applied power and the method used for frequency sampling. It would be interesting to continue to explore the intensity transmission subject to the effective power of the RF signal applied to the AOD. So far we only know that the voltage of the RF signal of the DDS is constant over our frequency range of 80 MHz to 120 MHz, however, we cannot make any statements with respect to the current characteristics. All in all there are too many factors to consider to describe with a simple analytical model and we will further try to work with a model-free optimization procedure in the next chapter in order to minimize the intensity transmission variance and produce a constant laser intensity in the atom plane.

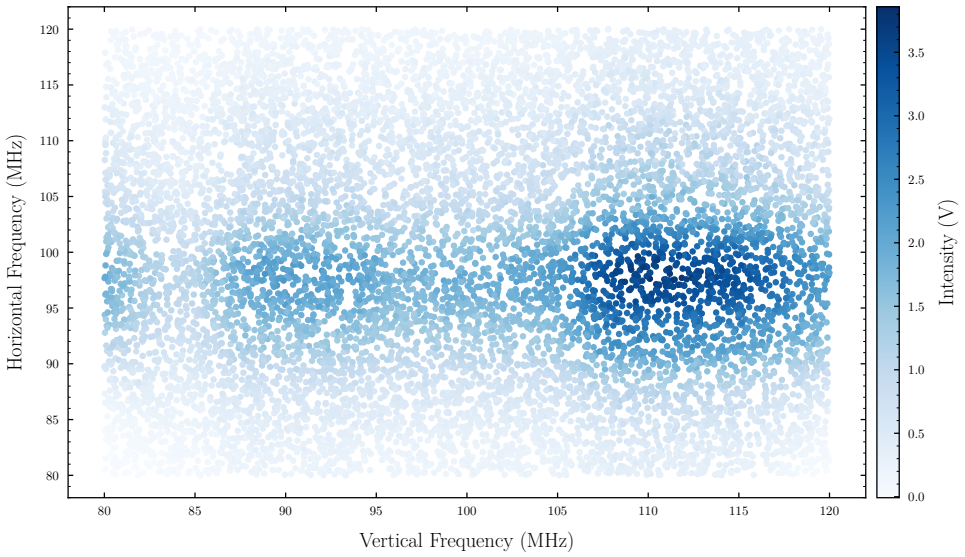

Figure 8.9.: Intensity measured as voltage at the photodiode in dependence of the horizontal and vertical applied frequency signal to the AOD. Frequency pairs are sampled over a uniform distribution and then passed as constant output frequency paramter to the DDS.

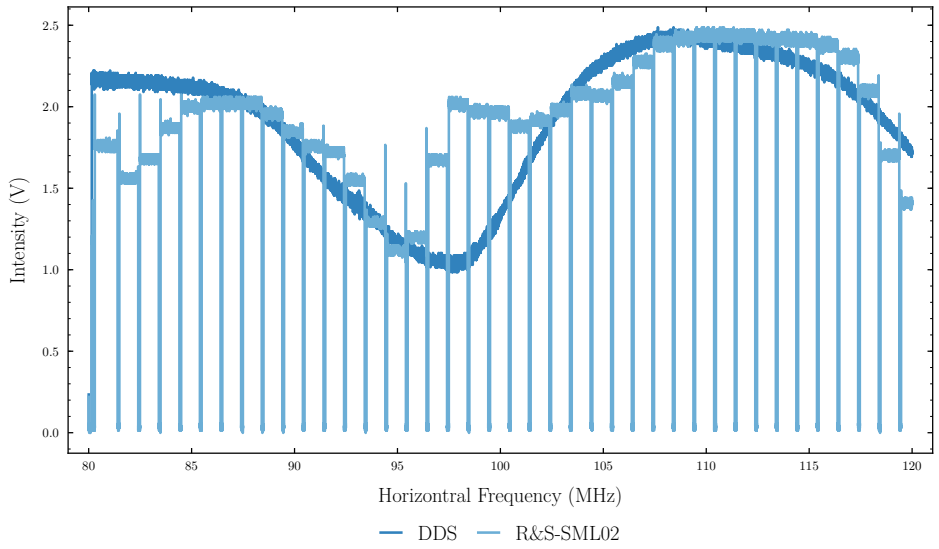

Figure 8.10.: Intensity measured as voltage at the photodiode with one AOD at constant center frequency supplied by a DDS and the other AOD performing a linear frequency sweep with the DDS and a high-quality signal generator.

8.3. Diffraction efficiency optimization

The previous two chapters addressed the characteristics of the RF signal and the intensity transmission of the AOD. Therewith the groundwork has been set out to finally approach the mission of minimizing the intensity variance to obtain a homogenous optical potential.

But how do we minimize the intensity variance? The DDS permits to read $N = 1024$ amplitude values from memory. The optimization problem therefore is to minimize the variance of the intensity distribution $I(A)$ subject to an amplitude vector $A \in [0, 1]^N$. The conclusions drawn from the intensity measurements suggest that we have to expect non-linear, irregular behaviour in $I(A)$, and indeed first attempts to model $I(A)$ through polynomial fits, multilayer perceptron networks and least-squared minimizations have failed.

During these optimization procedures we observed that changing an amplitude value $A_i \in A$ does affect the intensity voltage at subsequent $A_{i+1}, \ldots, A_N$. Fortunately we found that by respecting the amplitude order with respect to increasing frequency during optimization we where able to bypass these effects. Further we created amplitude segments $(A_j, \ldots, A_{j+m})$ consisting of m ordered amplitude values to reduce the optimization time. Optimization then was performed through random search which was proven to yield better results as grid search [33].

Overview

First, we want to provide an overview of the final optimization results obtained at different hyperparameters for the random search. The hyperparameter includes the number of amplitude segments N/m and the target intensity. In Figure 8.11 we present the final optimization results for target intensities of 800 mV, 1000 mV and 1200 mV and amplitude segments $8, 16, 32$. We observe heavy oscillations for amplitude segments greater than eight. The optimization results using 16 amplitude segments performs better than the run with 32 amplitude segments. At present we have no explainations for this behaviour. For the sake of simplicity we will limit us to the case of eight amplitude segments. In Figure 8.12 we have a closer view on the first column of Figure 8.11.

Process

We now want to elaborate on the optimization process. We limit ourselves to the optimization process with eight amplitude segments as it was the most successful one and can be covered completly with eight plots. In Figure 8.13 we see the intensity and amplitude at different optimization stages. At each stage one amplitude segment is sampled from a uniform distribution over $[0.2, 0.8]$. The intensity segment associated with this amplitude segment is then used to calculate the mean squarred error (MSE) and compare it to the previous best MSE. If the new MSE is less than the previous best MSE the previous best MSE is updated and the amplitude segment value is saved. This procedure is repeated 500 times. Every time a new best value was found we saved the data. For the diagrams we choose the four most separated iteration steps to visualize the process of the optimization.

If we take a look at the succeeding segment from the currently optimized amplitude segment we observe that these differ for different amplitude values and henceforth confirms that amplitude values are not independent but affect subsequent segments.

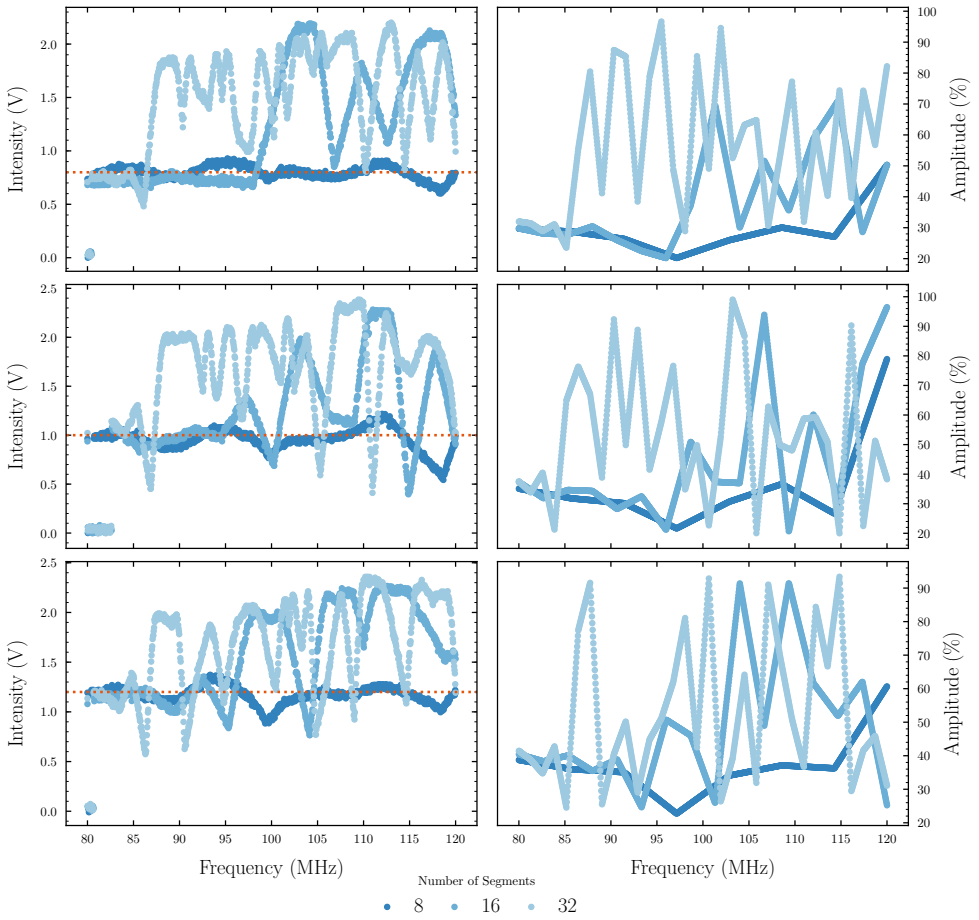

Figure 8.11.: Minimized intensity variance for different target intensities and number of amplitude segments. We note heavy oscillations for amplitude segments greater than eight.

Failure

With the optimization showing reasonable convergence for eight amplitude segments we would expect it to improve if we choose more amplitude segments, yet we observed heavy oscillations. In this section we want to check the optimization process in the case of 32 amplitude segments to investigate in the possible origins of the optimization failure. In Figure 8.14 we can see the optimization progress for selected amplitude segments of the optimization run with 32 segments. We observe that non-linear oscillations increase during the optimization process.

Summary

Our attemps to minimize the intensity variance where of mixed success. On the one hand we were able to minimize the intensity deviation down to 100 mV, on the other hand we were not able to train any model on the intensity response that would allow fast optimization or even predicition of the expected intensity response given an amplitude configuration.

However, we also found that irregularities arise when increasing the number of amplitude segments. We suspect that fast changes of the output amplitude draws power that may non-deterministically

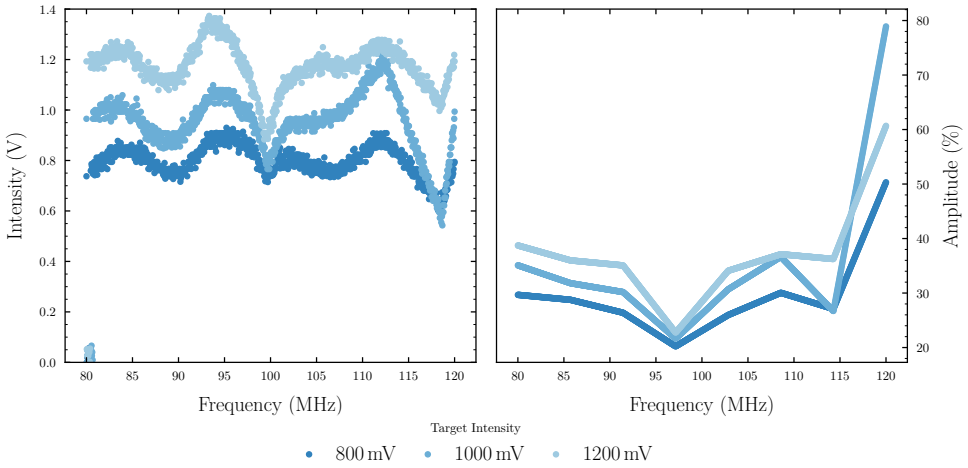

Figure 8.12.: Final result of the intensity variance minimization and the corresponding amplitude segment values obtained through random search with eight independent amplitude segments.

affect the next clock cycle inside the DDS. Given that the one dimensional optimizations already required multiple hours to run and the non-linear response between amplitude segments we do not believe that it is not within the capabilites of our present setup to compensate for the two dimensional intensity distribution measured in the previous chapter.

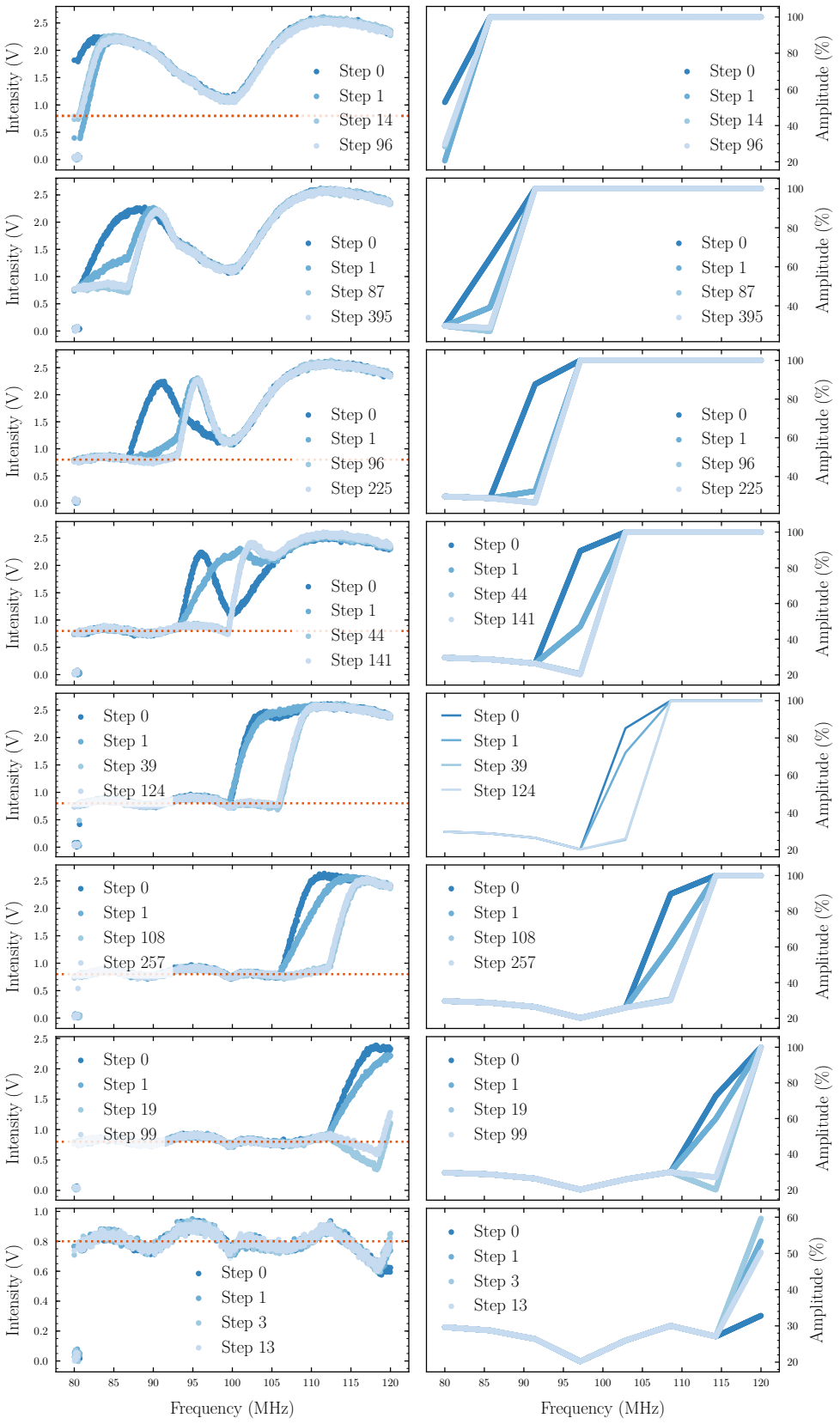

Figure 8.13.: Intensity and amplitude at different stages of the optimization process. In each column a different amplitude segment is optimized. The different traces in each plot mark the respective iteration.

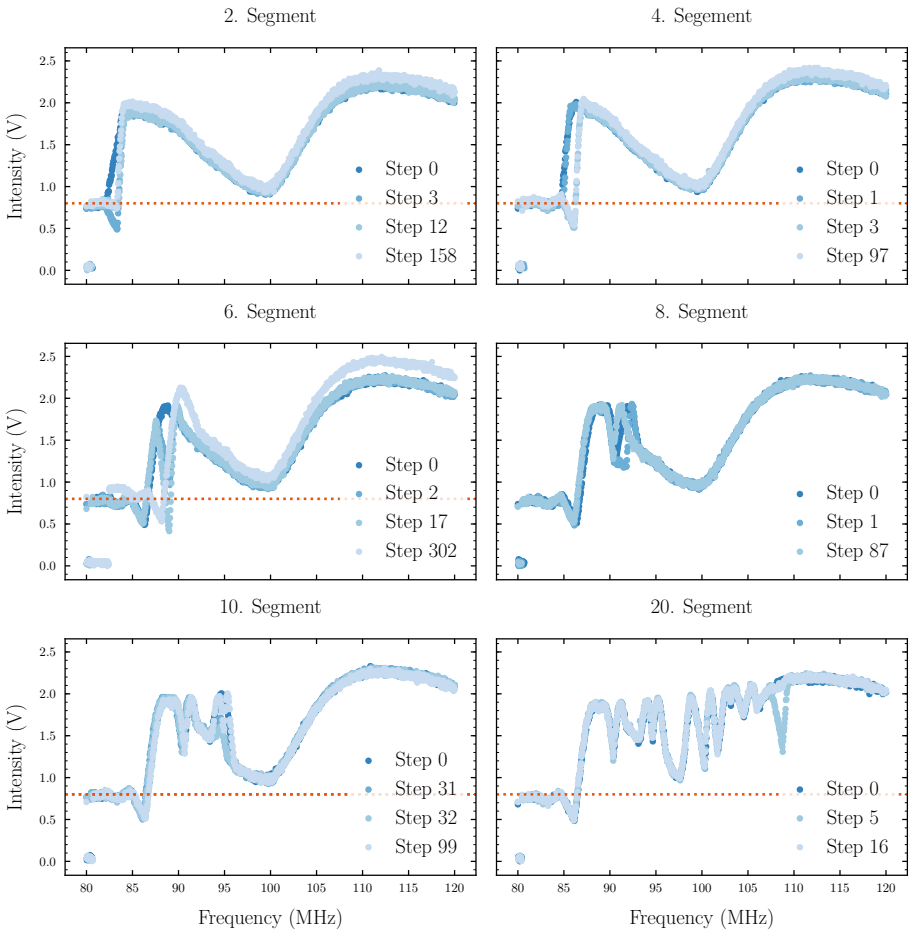

Figure 8.14.: Optimization progress for the 2.,4.,6.,8.,10. and 20. amplitude segment of the failed optimization run with 32 amplitude segments. We can see that with increasing amplitude segments the non-linear response following the optimized amplitude segment increases.

Chapter 9.

Summary and outlook

We began this thesis with an introduction to the field of ultracold atoms in optical lattices and motivated the need for local time-averaged optical potentials as an alternative to harmonic traps, as well as a pathway for new potential dynamics. From there we dove into the physics of atoms in optical lattices, in order to obtain an understanding of the requirements placed on our technical implementation. In this context we found that the deflection of our optical perurbation needs to operate on a time scale of about 100 kHz and that we need a tightly focused laser beam in order to create high-precision perturbation potentials. Fortunately Hertlein has already proven in Ref. [12] that our optical setup is capable of creating such high-precision beams in the atom plane. So we were left with exploring the limitations of our electronic and acousto-optic setup.

In Chapter 6 we concluded that digital signal synthesis is in theory an ideal platform for us to create a stable, phase continous, high-precision RF signal and in fact measurements in Chapter 7 have proven mostly good characteristics of the used AD9910 DDS. However, we also found that our AD9910 implementation shows a signal delay when receiving an external trigger of up to 40 µs which is a deal breaker as we need to operate on time scales below 10 µs. Furthermore the frequency resolution of the digital ramp may be too low to create spatially continous potentials (depending on the lattice parameters) in the atom plane. Howsoever we need to recognize that the AD9910 is sold as a general purpose DDS. It is likely that there are other DDS that suit our demands better or that one can create an own DDS design using field programmable gate array (FPGA).

In the second part of our work we investigated the characteristics of our 2D AOD. We found that the AODs exhibit a non-linear response to the relative amplitude and frequency of the applied RF signal. It remains open if it is the AOD to blame for or if there are electronic effects we did not unveal. Evidence that points into the direction that there may be electronic defects contributing to the non-linear characteristic of the AOD where found in Section 8.2 where we used a signal generator to perform a frequency sweep and found differences in the diffraction efficiency spectrum. We would like to check if these observed differences are due to different current characteristics. So far we only measured the voltage amplitude of the amplified DDS where we did not observe a significant frequency dependency.

We would also like to dig deeper into the theory of acousto-optics to check if there are any reports of the observed characteristics and if there are workarounds. In addition we would find theoretical evidence that our acousto-optics can handle the targeted time scales. It may be very well the case that the speed of sound inside the acousto-optics is too slow to deflect the laser beam on our required time scale. This would also explain the instability we observed in the attempt to minimize the variance of the diffraction efficiency. Good literature that should answer these and more questions can be found in Ref. [34] and Ref. [25].

In case that the AODs do show theoretial limitations, or we can exclude electronic defects for the observed characteristics and we need to accept these characteristics as given, we could also investigate electro-optical deflectors (EOD)s. EODs utilize the electro-optical effect to deflect a laser beam. Usually electrical fields are well understood and controllable, such that these do not fall under the same limitations as the AODs, however EODs require high voltages which may cause other problems.

Finally there are also interesting industrial applications to consider if the outstanding issues can be resolved. For example the field of ophthalmologics covers a wide range of opportunities for precision laser control like corrective eye surgeries which according to [35], [36] and [37] make use of mechanical deflectors. Certainly there are also industrial applications in solid-state industries, yet we did not check up closer.

Glossary

AD9910 a direct digital synthesizer from Analog Devices.

SI International System of Units.

Acronyms

1D one-dimensional.

2D two-dimensional.

3D three-dimensional.

AOD acousto-optic deflector.

AOM acousto-optic modulator.

CCD charge-coupled device.

CDF cummulative distribution function.

DAC digital to analog converter.

DDS direct-digital synthesizer.

FFT fast-fourier-transform.

FPGA field programmable gate array.

FWHM full width at half maximum.

H horizontal.

IQR interquartile range.

MOT magneto-optical trap.

MSE mean squarred error.

PLL phase-locked-loop.

RF radio frequency.

RMD relative mean deviation.

RWA rotating wave approximation.

SMF single-mode optical fiber.

V vertical.

VCO voltage-controlled oscillator.

List of Figures

1.1. Apparatus of the cesium experiment. On the left-hand side an oven heats up the cesium source. A 2D MOT generates a particle beam twoards the pipe running through the Zeeman slower in the center. The Zeeman slower creates a magnetic field gradient, such that the atoms are in resonance with a cooling laser antiparallel to their flight direction. In the 3D MOT atoms are cooled even further until they are transported to a glass cell where they are loaded into the optical lattice and the actual experiments are conducted. Thank you to Till Klostermann and Hendrik v. Raven for providing the cesium apparatus render. 7
1.2. Simple square 2D optical lattice. The atoms (blue points) sit on their respective lattice site created by the superposition of two periodic potentials. 8
1.3. Simple square 2D optical lattice with local barrier potential. The local barrier potential confines atoms inside the green box in a finite homogeneous lattice potential. 9
1.4. Simple square 2D optical lattice with local pot potential. The local potental pot draws particles from the unperturbated lattice potential to a confined area. 11

2.1. Illustration of Gaussian beam parameters from Ref. [19] translated into English with changed radius of curvature. 15
2.2. Local pot potential and lattice potential in recoil energies. The pot potential is created by targetting multiple focus points close to each other. Over average this yields a kind of potential valley. 17
2.3. Local barrier potential and lattice potential in recoil energies. The barrier potential is created by targetting two different focus points with the perturbation beam (first two rows). If both focus points are targetted in a sufficiently short period an average potential (last row) can be created. 18

3.1. Probability density of the wave functions of the harmonic approximation of the lattice potential. 20
3.2. Energy band structure for $N = 51$ lattice sites and various lattice potential depths V_0. 23
3.3. Minimum and maximum energy range for the first four energy bands with the energy levels derived from the harmonic approximation. 23
3.4. Nearest-neighbor hopping energy derived from the exact numerical calculations, the tight-binding approximation and an analytical proxmity eq. (3.33). 25
3.5. Hopping energies for different neighbour ranges. 26
3.6. Nearest-neighbor hopping energy as frequency and relative energy band differences with respect as frequency. 26

4.1. Drawing of the used 2D AOD. 28
4.2. Optical configuration of the power reduction section. 29
4.3. Optical configuration of the beam deflection section. 30
4.4. Electronic setup used to control the electro-optic devices. 31
4.5. Block diagram of a PID feedback loop. 32

4.6. Communication setup of the electronic devices in the experimental setup. 33
4.7. Text projection as captured by the CCD camera. 35

5.1. Time evolution of the uncontrolled laser intensity. 36
5.2. Optical setup and intensity detection. The beam hits Photodiode 2 which is connected to the oscilloscope. 37
5.3. Long- and short-term measurement of the controlled intensity at different voltage scales. 38
5.4. RMD of not-stabilized and actively stabilized long- and short-term measurement as well an actively stabilized AOD intensity measurement. 39
5.5. The beam is focused onto the CCD sensor of the camera. 39
5.6. Image of the focused laser beam measured with the CCD camera. 40
5.7. One dimensional perpendicular cut of the two dimensional intensity distribution from the two dimensional beam profile in Figure 5.6 with fitted gaussian curve. . 40

6.1. Signal flow through a simple DDS. The output frequency determines a phase step $\Delta\varphi$ by which the accumulator is incremented at each clock cycle. The value of the phase accumulator is used for amplitude lookup of the desired output signal shape. A DAC samples the output signal which then is filtered to smooth the discrete DAC output. 42
6.2. Signal outputs at different stages in a simple DDS. The phase accumulator is incremented at each clock cycle by $\Delta\phi$. The phase accumulator value is used to lookup a sinusoidal amplitude value that is supplied to a DAC. The final result is smoothed using a filter. 43
6.3. Block diagram of the system clock generation from reference clock through PLL and divider. 44
6.4. DDS architecture supporting modulation of frequency, amplitude and phase offset parameters. Phase accumulator increment $\Delta\varphi_n(t)$ is now time dependent. The phase offset $\varphi_n(t)$ is also time dependent and is added as a last step to the phase accumulator before supplied to the DAC. The time dependent amplitude parameter $A_n(t)$ is multiplied with the amplitude obtained from the lookup table. 44
6.5. Phase error for system model parameters in Table 6.1 when comparing phase accumulator with $2^N = 256$ and 250 values. 45
6.6. Power transfer of the DAC according to the zero-order hold model with respect to relative output frequency from zero to the Nyquist frequency $f_{\mathrm{sys}}/2$. In the second plot we see the power transfer for the later operating range of the DDS. 47
6.7. Playback sample interval and total playback duration when using the complete 1024 memory points in dependency of the playback rate word P. 48

7.1. Idealized DDS signal output with constant frequency increments. The measured window only captures a subset (gray) of the complete modulation (shades of blue). 51
7.2. Measurement setup of the synthesizer signal. By inserting a pulse generator in between the trigger source and the oscilloscope we can delay the capture window of the oscilloscope by the pulse width. 52
7.3. Spectrogram of delayed time windows with width 100 µs of the DDS output signal configured to perform a linear frequency sweep. For an ideal linear sweep we would expect a linear timeline of the frequency, instead we observe a discrete set of frequencies. 53
7.4. Most dominant frequency in the FFT spectrum for each (delayed) measurement during a frequency sweep of the DDS. 54
7.5. Amplitude frequency response of the DDS signal sources for the H and V AOD. The frequency increments are performed through the integrated digital ramp and manually. 55

7.6. Amplitude frequency response of the DDS signal after power amplification. In comparison to the DDS we observe very small oscillations. 56
7.7. Frequency transmission spectrum obtained via the network analyzer of the horzional and vertical amplifiers. 57
7.8. Signal reflection of the two different AOD when directly connected to the network analyzer. 58
7.9. Reflection at the direct-coupler output after amplification of the network analyzer input signal for different amplifications with reference to 1 mW. We see that the applied power does not affect the spectrum. 59
7.10. Experimental setup to measure the reflection at the acousto-optic transducer. The network analyzer supplies an input signal to the amplifier. The output signal of the amplifier is connected through a directional coupler with the acousto-optic element. The directional coupler allows to safely measure input and output reflection. . . . 59
7.11. Input power reflection when supplying the directional coupler with $-10\,\mathrm{dB\,m}$ input signal and reflection at the closed output of the directional coupler while other ports are closed with 50 60
7.12. Reflection from amplified input signal and direct signal as well as transmission spectrum from the amplifier. We can see that the better amplification left of 90 MHz slightly changes the reflection spectrum of the AOD. 60

8.1. Intensity distribution over linear frequency sweep at different configured DDS amplitudes for different individual AOD configurations. 62
8.2. Intensity transmission of the H AOD in the H slot at maximum output amplitude for different angles of the $\lambda/2$ plate. 62
8.3. Intensity transmission of the V AOD in the V slot at maximum output amplitude for different angles of the $\lambda/2$ plate. 63
8.4. Intensity transmission of the H and V AOD at 100 MHz and maximum output amplitude for different polarisation angles. 64
8.5. Intensity distribution at different amplitudes for tilted individual AODs. We observe that the intensity decreases if the incident angle deviates from 90°. 64
8.6. Experimental setup used to measure the intensity transmission of the 2D AOD in dependence of the configured DDS signal. 65
8.7. Intensity measured as voltage at the photodiode in dependence of the horizontal and vertical applied frequency signal to the AOD. The left map is obtained by enabling the digital ramp on the horizontal DDS whereas the vertical DDS is configured to output a constant frequency which is manually increased after each measurement. On the right-hand side map the roles are exchanged. 66
8.8. Absolute difference between the 2D intensity distribution performed with the digital ramp configured set to different axes. 67
8.9. Intensity measured as voltage at the photodiode in dependence of the horizontal and vertical applied frequency signal to the AOD. Frequency pairs are sampled over a uniform distribution and then passed as constant output frequency paramter to the DDS. 68
8.10. Intensity measured as voltage at the photodiode with one AOD at constant center frequency supplied by a DDS and the other AOD performing a linear frequency sweep with the DDS and a high-quality signal generator. 68
8.11. Minimized intensity variance for different target intensities and number of amplitude segments. We note heavy oscillations for amplitude segments greater than eight. . 70
8.12. Final result of the intensity variance minimization and the corresponding amplitude segment values obtained through random search with eight independent amplitude segments. 71
8.13. Intensity and amplitude at different stages of the optimization process. In each column a different amplitude segment is optimized. The different traces in each plot mark the respective iteration. 72

8.14. Optimization progress for the 2.,4.,6.,8.,10. and 20. amplitude segment of the failed optimization run with 32 amplitude segments. We can see that with increasing amplitude segments the non-linear response following the optimized amplitude segment increases. 73

A.1. Elecronic circuit schematics of the trigger hub. The 3.3 V input signal is amplified by the SN74128 line driver and outputed to four SubMiniature version A (SMA) connectors. 88

B.1. Focused camera with view on the balcony bars on the top of the university tower. 91
B.2. Focused camera with view on the weather cock on the top of the university tower. 92

List of Tables

2.1. Typical values for a Gaussian beam used to generate an optical lattice potential. . 16
2.2. Typical values for a Gaussian beam used to perturbate the optical lattice potential reported by [12]. 16

3.1. Parameters used for the lattice Hamiltonian matrix elements to calculate the energy bands. 22

5.1. Interval and duration times of the short- and long-term measurement as well as a typical AOD frequency sweep measurement. 37
5.2. Descriptive statistics of not-stabilized and actively stabilized short- and long-term intensity evolutions as well as a typical AOD frequency sweep measurement for comparison. 38

6.1. System parameters used for our simplified DDS model and used in the AD9910. . 43
6.2. Minimal and maximal playback parameters of the AD9910 according to eq. (6.18) with $f_{\mathrm{sys}} = 1\,\mathrm{GHz}$. 48
6.3. Digital ramp register that control the frequency and their respective presicion. . . 49
6.4. Digital ramp limit registers for a frequency sweep from 80 MHz to 120 MHz. . . . 49
6.5. Digital ramp step registers for a frequency sweep from 80 MHz to 120 MHz with duration $T_{\mathrm{ramp}} = 260\,\mathrm{ms}$. 49
6.6. Time scales of the AD9910 imposed by the technical limits of the playback duration time of the AD9910. 50

7.1. Experimental parameters used to inspect the output RF signal of the DDS. 52

List of Listings

4.1. Example usage of the Python module to control the setup. 34

A.1. BBB script that starts a HTTP server to listen for requests on which to trigger a rising edge signal. On execution it pulls the signal general purpose input output (GPIO) to high. The request callback then pulls the GPIO to low for one 1 ms. . 89

Bibliography

[1] Immanuel Bloch, Jean Dalibard, and Wilhelm Zwerger. "Many-body physics with ultracold gases". In: *Rev. Mod. Phys.* 80 (3 July 2008), pp. 885–964. DOI: 10.1103/RevModPhys.80.885. URL: https://link.aps.org/doi/10.1103/RevModPhys.80.885.

[2] Christian Gross and Immanuel Bloch. "Quantum simulations with ultracold atoms in optical lattices". In: *Science* 357.6355 (2017), pp. 995–1001. ISSN: 0036-8075. DOI: 10.1126/science.aal3837. eprint: http://science.sciencemag.org/content/357/6355/995.full.pdf. URL: http://science.sciencemag.org/content/357/6355/995.

[3] William D. Phillips. "Nobel Lecture: Laser cooling and trapping of neutral atoms". In: *Rev. Mod. Phys.* 70 (3 July 1998), pp. 721–741. DOI: 10.1103/RevModPhys.70.721. URL: https://link.aps.org/doi/10.1103/RevModPhys.70.721.

[4] Rudolf Grimm, Matthias Weidemüller, and Yurii B. Ovchinnikov. "Optical Dipole Traps for Neutral Atoms". In: ed. by Benjamin Bederson and Herbert Walther. Vol. 42. Advances In Atomic, Molecular, and Optical Physics. Academic Press, 2000, pp. 95–170. DOI: https://doi.org/10.1016/S1049-250X(08)60186-X. URL: http://www.sciencedirect.com/science/article/pii/S1049250X0860186X.

[5] Matthew P. A. Fisher et al. "Boson localization and the superfluid-insulator transition". In: *Phys. Rev. B* 40 (1 July 1989), pp. 546–570. DOI: 10.1103/PhysRevB.40.546. URL: https://link.aps.org/doi/10.1103/PhysRevB.40.546.

[6] D. Jaksch et al. "Cold Bosonic Atoms in Optical Lattices". In: *Phys. Rev. Lett.* 81 (15 Oct. 1998), pp. 3108–3111. DOI: 10.1103/PhysRevLett.81.3108. URL: https://link.aps.org/doi/10.1103/PhysRevLett.81.3108.

[7] Tin-Lun Ho and Qi Zhou. "Squeezing out the entropy of fermions in optical lattices". In: *Proceedings of the National Academy of Sciences* 106.17 (2009), pp. 6916–6920. ISSN: 0027-8424. DOI: 10.1073/pnas.0809862105. eprint: http://www.pnas.org/content/106/17/6916.full.pdf. URL: http://www.pnas.org/content/106/17/6916.

[8] Jean-Sébastien Bernier et al. "Cooling fermionic atoms in optical lattices by shaping the confinement". In: *Phys. Rev. A* 79 (6 June 2009), p. 061601. DOI: 10.1103/PhysRevA.79.061601. URL: https://link.aps.org/doi/10.1103/PhysRevA.79.061601.

[9] Anton Mazurenko et al. "A cold-atom Fermi–Hubbard antiferromagnet". In: *Nature* 545.7655 (2017), p. 462.

[10] Brian J. Roxworthy et al. "Application of Plasmonic Bowtie Nanoantenna Arrays for Optical Trapping, Stacking, and Sorting". In: *Nano Letters* 12.2 (2012). PMID: 22208881, pp. 796–801. DOI: 10.1021/nl203811q. eprint: https://doi.org/10.1021/nl203811q. URL: https://doi.org/10.1021/nl203811q.

[11] Richard Roy et al. "Rapid cooling to quantum degeneracy in dynamically shaped atom traps". In: *Phys. Rev. A* 93 (4 Apr. 2016), p. 043403. DOI: 10.1103/PhysRevA.93.043403. URL: https://link.aps.org/doi/10.1103/PhysRevA.93.043403.

[12] Simon Hertlein. "Test setup for single–site manipulation using a 2D acousto-optic deflector"". 2017.

[13] C. Gerry and P. Knight. *Introductory Quantum Optics*. Cambridge University Press, 2004. ISBN: 9781139453554. URL: https://books.google.de/books?id=MDwgAwAAQBAJ.

[14] J. Jackson and J.D. Jackson. *Wie Classical Electrodynamics, 3rd Edition, Intern Ational Edition*. John Wiley & Sons, Limited, 2005. ISBN: 9780471427643. URL: https://books.google.de/books?id=XFyDkgEACAAJ.

[15] M. Bartelmann et al. *Theoretische Physik 2*. Springer Berlin Heidelberg, 2018. ISBN: 9783662561164. URL: https://books.google.de/books?id=seqmswEACAAJ.

[16] Lea Boßmann. "On the Dipole Approximation". 2016. URL: http://www.mathematik.uni-muenchen.de/~bohmmech/theses/Bossmann_Lea_MA.pdf.

[17] H.A. Bethe and E.E. Salpeter. *Quantum mechanics of one- and two-electron atoms*. Springer, 1957. URL: https://books.google.de/books?id=1ZUuAAAAIAAJ.

[18] Rudolf Grimm, Matthias Weidemüller, and Yurii B. Ovchinnikov. "Optical Dipole Traps for Neutral Atoms". In: Advances In Atomic, Molecular, and Optical Physics 42 (2000). Ed. by Benjamin Bederson and Herbert Walther, pp. 95–170. ISSN: 1049-250X. DOI: https://doi.org/10.1016/S1049-250X(08)60186-X. URL: http://www.sciencedirect.com/science/article/pii/S1049250X0860186X.

[19] Wikimedia Commons. *File:Gaussian beam with german description.svg — Wikimedia Commons, the free media repository*. [Online; accessed 31-August-2018]. 2014. URL: https://commons.wikimedia.org/w/index.php?title=File:Gaussian_beam_with_german_description.svg&oldid=143765578.

[20] Tim Rom. "Bosonische und fermionische Quantengase in dreidimensionalen optischen Gittern". Dec. 2009.

[21] U. Rössler. *Solid State Theory: An Introduction*. Advanced Texts in Physics. Springer Berlin Heidelberg, 2004. ISBN: 9783540222446. URL: https://books.google.de/books?id=qgU50X9vtIoC.

[22] Frederik Görg. "Ultracold Fermionic Atoms in Optical Superlattices". Mar. 2014.

[23] Ulf Bissbort. "Dynamical effects and disorder in ultracold bosonic matter". 2013. URL: http://publikationen.ub.uni-frankfurt.de/frontdoor/index/index/docId/28591.

[24] J. N. L. Connor et al. "Eigenvalues of the Schrödinger equation for a periodic potential with nonperiodic boundary conditions: A uniform semiclassical analysis". In: *The Journal of Chemical Physics* 80.10 (1984), pp. 5095–5106. DOI: 10.1063/1.446581. eprint: https://doi.org/10.1063/1.446581. URL: https://doi.org/10.1063/1.446581.

[25] D. ROYER, S.N. Lyle, and E. Dieulesaint. *Elastic Waves in Solids II: Generation, Acousto-optic Interaction, Applications*. Advanced Texts in Physics. Springer Berlin Heidelberg, 1999. ISBN: 9783540659310. URL: https://books.google.de/books?id=q%5C_9rJYpgjZ0C.

[26] *A Technical Tutorial on Digital Signal Synthesis*. Analog Devices. URL: https://www.ieee.li/pdf/essay/dds.pdf.

[27] *1 GSPS, 14-Bit, 3.3 V CMOS Direct Digital Synthesizer*. AD9910. Rev. D. Analog Devices. May 2012. URL: http://www.analog.com/media/en/technical-documentation/data-sheets/AD9910.pdf.

[28] J. Vankka and K.A.I. Halonen. *Direct Digital Synthesizers: Theory, Design and Applications*. The Springer International Series in Engineering and Computer Science. Springer US, 2013. ISBN: 9781475733952. URL: https://books.google.de/books?id=-CsLCAAAQBAJ.

[29] L. Cordesses. "Direct digital synthesis: a tool for periodic wave generation (part 1)". In: *IEEE Signal Processing Magazine* 21.4 (July 2004), pp. 50–54. ISSN: 1053-5888. DOI: 10.1109/MSP.2004.1311140.

[30] B.G. Goldberg. *Digital techniques in frequency synthesis*. McGraw-Hill, 1996. ISBN: 9780070241664. URL: https://books.google.de/books?id=oCtTAAAAMAAJ.

[31] A.V. Oppenheim, A.S. Willsky, and S.H. Nawab. *Signals and Systems*. Prentice-Hall signal processing series. Prentice Hall, 1997. ISBN: 9780138147570. URL: https://books.google.de/books?id=LwQqAQAAMAAJ.

[32] David T. Ashley et al. "On Best Rational Approximations Using Large Integers". In: (2013). URL: http://esrg.sourceforge.net/docs/paper_brap_detailed.pdf.

[33] James Bergstra and Yoshua Bengio. "Random Search for Hyper-parameter Optimization". In: *J. Mach. Learn. Res.* 13 (Feb. 2012), pp. 281–305. ISSN: 1532-4435. URL: http://dl.acm.org/citation.cfm?id=2188385.2188395.

[34] *Design and Fabrication of Acousto-Optic Devices*. Optical Science and Engineering. Taylor & Francis, 1994. ISBN: 9780824789305. URL: https://books.google.de/books?id=iGQvMUy3C0AC.

[35] Mark Bendett et al. "Method and apparatus for precision working of material". US20180110655. 2018.

[36] Mark E. Arnoldussen et al. "Operator-controlled scanning laser procedure designed for large-area epithelium removal". US20180064579. 2008.

[37] Mark Bendett et al. "Apparatus and method for opthalmologic surgical procedures using a femtosecond fiber laser". US7131968. 2004.

[38] *SN54128, SN74128 Line Drivers*. Analog Devices. Mar. 1988. URL: http://www.ti.com/lit/ds/symlink/sn74128.pdf.

Appendix A.

Electronics

A.1. Trigger hub

The trigger hub is driven by a 3.3 V input signal and a 5 V voltage source. The input signal is amplified to drive four transistor-transistor logic (TTL) inputs through use of the SN74128 [38] line driver. Furthermore the hub is designed to be mounted on the BBB which itself provides the trigger network interface. The SN74128 exposes four independent outputs Y, each is driven by a

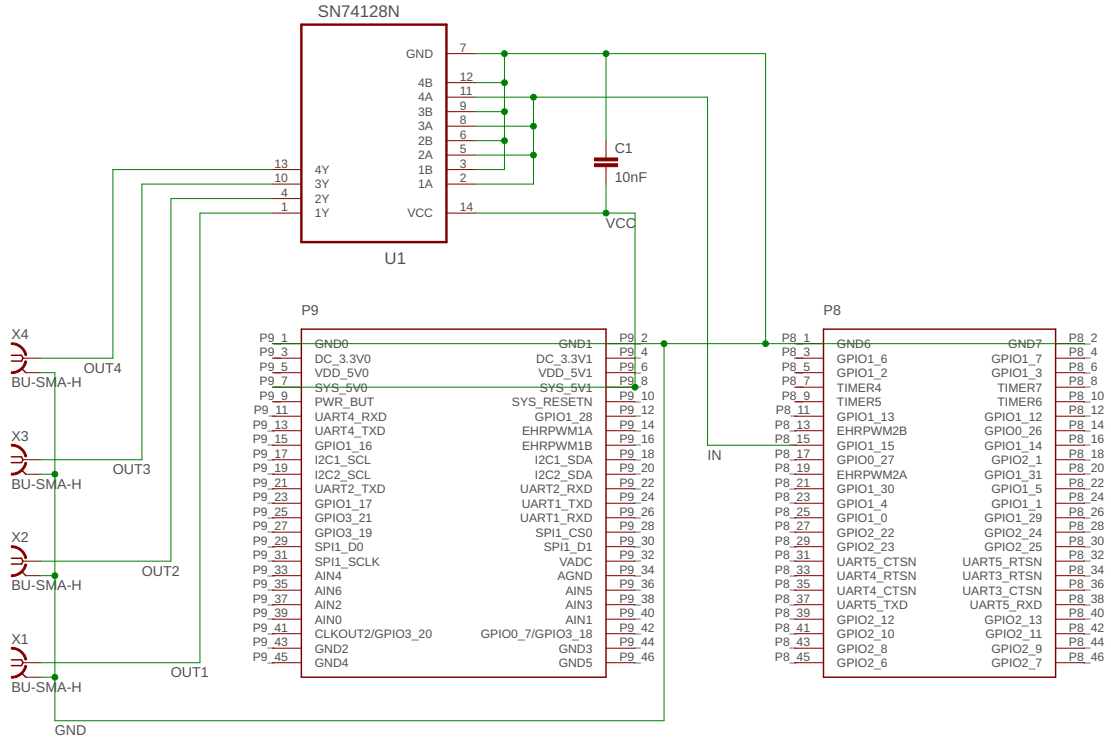

Figure A.1.: Elecronic circuit schematics of the trigger hub. The 3.3 V input signal is amplified by the SN74128 line driver and outputed to four SMA connectors.

two-input (A and B) with NOR ($\overline{A+B} = Y$) logic. As our objective is to forward rising edge trigger signals we pulled all four B to low by connecting them with ground (GND). The four A

where connected together with the input signal. The input signal has to transition from 1 to 0 in order to signal a rising edge trigger signal. Using the BBB makes it easy to write scripts that

```
var http = require('http')
var bone = require('bonescript')

const PIN = 'P8_15'

bone.pinMode(PIN, 'out')
bone.digitalWrite(PIN, 1)

http.createServer(function(req, res) {
  bone.digitalWrite(PIN, 0)

  setTimeout(function() {
    bone.digitalWrite(PIN, 1)

    res.end('OK')
  }, 1)
}).listen(6200)
```

Listing A.1.: BBB script that starts a HTTP server to listen for requests on which to trigger a rising edge signal. On execution it pulls the signal GPIO to high. The request callback then pulls the GPIO to low for one 1 ms.

communicate with other devices over the LAN. We used the bonescript library to access the GPIO interface as it is pre-installed on the BBB.

Appendix B.

Calibration

Alterations of the laboratory environment combined with the exchange of components from the original setup made it necessary to recalibrate the setup. In this chapter we want to document the calibration steps required to reproduce the claimed results.

B.1. Fiber coupling

The visually shielded section of the setup, used to reduce the output power of the laser source, is optically paired with the open section for beam deflection via a SMF that only permits two orthogonal polarization and a single gaussian mode. By tuning the polarisator inside the power reduction section we can try to match one of the orthogonal polarization modes supported by the SMF. Polarization discrepancies cause the polarization inside the SMF to oscillate with vibrations or changes in temperature, henceforth it is key to couple polarization modes in order to ensure a stable operation. A strategy proven to find an approximate polarization match between the laser beam and the SMF is presented. In addition to the setup described in Section 4.1.2 and Section 4.1.2 an oscilloscope and a hot air gun were used.

1. Connect the photodiode to the oscilloscope and use a coarse time scale (i.e. 2 s).

2. Apply appropriate laser safety glasses and inform present personal of the imminent danger.

3. Open the cover of the power reduction setup.

4. Apply heat to the SMF through the hot air gun, alternatively you can try to move the fiber.

5. The photodiode signal should start to oscillate. Tune the polarizor inside the power reduction subject to minimizing the oscillation.

The oscillations occur as the polarization circulates inside the fiber and will stop at some point when a new equilbrium has been established. In this case remove the heat or mechanical stress on the fiber and wait before you reapplying new impetus.

B.2. Beam alignment

Beams that pass off-centered through spherical lenses experience optical aberrations, additionally uncentered beams may cause further optical defects from reflections or clipping at boundaries. Since most changes to the optical setup outdate the previous beam alignment, hence making the realignment a rather frequent procedure, we want to showcase what worked well for us. As auxilliaries we used a pair of iris diaphragms that can be placed in front of the lens mounts as a screen (i.e. a white sheet of hard paper). By placing both iris diaphragms towards the incident beam on two successive lenses we we can visually find a center reference point by inspecting the symmetry of the iris illumination at different pinhole diameters.

B.3. Camera focus

Finally we had to reposition the camera to focus the incoming beam on the CCD sensor of the camera. Finding the precise focus position is not an easy undertaking. There is no sharp focal spot but rather a focal area, however outside the focal area no image can be seen. We followed the procedure described in [12] that consists of extracting the camera rail with its lens and focusing it on a far distant object. In our case we choose the university tower as distant object. The window

Figure B.1.: Focused camera with view on the balcony bars on the top of the university tower.

frame used by [12] was overgrown by trees at the time of writing. In Figure B.1 we can see the

university tower as seen by a common digital camera. If we look careful on the left-hand side of the tower top we discover a weathercock. In Figure B.2 we can see the weathercock on top of the

Figure B.2.: Focused camera with view on the weather cock on the top of the university tower.

university tower as seen by the CCD camera at aligned focal position.

Declearation of authorship

Statutory declearation

I hereby declare that this thesis has been composed solely by myself except where indicated otherwise by reference or acknowledgment.

The work presented has not been submitted, in whole or in part, in any previous application for a degree.

Munich, September 7, 2018